University of the Witwatersrand



Doctoral Thesis

Beam Shaping and Amplifiers

Author:
Mr. Arthur Justin Harrison

Supervisor:
Dr. Darryl Naidoo

Co-Supervisor:
Prof. Andrew Forbes

A thesis submitted in fulfillment of the requirements for the degree of Doctor of Philosophy

in the

Structured Light Laboratory
School of Physics

June 9, 2023

Declaration of Authorship

I, Mr. Arthur Justin Harrison, declare that this thesis titled, "Beam Shaping and Amplifiers" and the work presented in it are my own. I confirm that:

- This work was done wholly or mainly while in candidature for a research degree at this University.
- Where any part of this thesis has previously been submitted for a degree or any other qualification at this University or any other institution, this has been clearly stated.
- Where I have consulted the published work of others, this is always clearly attributed.
- Where I have quoted from the work of others, the source is always given. With the exception of such quotations, this thesis is entirely my own work.
- I have acknowledged all main sources of help.
- Where the thesis is based on work done by myself jointly with others, I have made clear exactly what was done by others and what I have contributed myself.

Signed:



Date: June 9, 2023

"*I... a universe of atoms, an atom in the universe*"

Richard P. Feynman

UNIVERSITY OF THE WITWATERSRAND

Abstract

Doctor of Philosophy

Beam Shaping and Amplifiers

by Mr. Arthur Justin Harrison

Tailored or structured laser light has received much attention from the photonics community globally. Structured forms of laser light have the potential to enhance many aspects of laser-enabled processes across a myriad of applications, such as industrial manufacturing processes, optical communication, quantum computing, medical sciences, and space sciences. While the laser itself is well over 60 years old, the range of obtainable "structured" laser outputs has been restricted for many decades since its inception. With recent advances in micro-mechanical electro-optics, liquid crystal display, and advanced lithographic processing technologies, it is possible for us to create highly complex forms of structured light with exotic spatial, phase, and polarization characteristics. As we make the inevitable transitions towards updating the existing laser technology with structured light systems, there are certain parameters that need to be met such as average laser power, which is crucial for performing micro and macro material processing, accounting for 15% of the global demand for lasers. Therefore, in addition to the selection of structured light, there is a clear need for obtaining high-power structured light which generally involves the need for optical power amplifiers.

This dissertation explores the generation, power scaling, and characterization of structured light for application areas that demand high-power laser outputs. To fully characterize the process of power scaling of structured laser light, an accurate 3D numerical model is required. Here we present a new 3D model for an end-pumped cylindrical rod Master Oscillator Power Amplifier (MOPA) system, using contemporary analytical expressions and novel approximations which demonstrate significant improvements over current comparative 3D modelling approaches. Then, we explore the amplification of structured light fields, in the form of higher-order Laguerre-Gaussian modes, using a novel polarization-based dual-pass MOPA. This system was specifically developed to maximize amplification efficiency while maintaining the purity and complex structures of high-order Laguerre-Gaussian modes and showed excellent agreement with the 3D simulated results. Finally, we investigate the thermally-induced aberrations resulting from end-pumping bulk solid-state gain media. We show that amplification of higher-order Laguerre-Gaussian modes in this aberrated system, specifically those possessing orbital angular momentum, results in the separation of the phase singularities, otherwise known as "vortex splitting". We fully study this effect and describe the cause and rectification of this phenomenon.

Acknowledgements

I extend my gratitude to the Council for Scientific and Industrial Research (CSIR) and the National Laser Center (NLC) for providing me with financial support and the opportunity to pursue my passion for science. I would like to thank my supervisor, Dr. Darryl Naidoo, for his patience, willingness to share knowledge, and friendship during this time. I am grateful for the freedom you gave me to explore science in my own way, thank you very much. I would like to acknowledge and thank my co-supervisor, Prof. Andrew Forbes, your dedication to science and your students is inspirational, it has been an honour to be part of your exceptional group. I want to express my appreciation to my colleagues at the NLC, Dr. Hencharl Strauss, Dr. Chemist Mabena, Dr. Attie Hendriks, Mr. Ameeth Sharma, and Dr. Nokwazi Mphuthi, for your valuable discussions, support, and motivation during this time. Thank you to my student peers at the University of the Witwatersrand for their support.

I would like to give a special acknowledgement to my wife, Melissa Harrison, for her love and support every day, I couldn't have done this without you. Throughout this journey, we have shared all the hardships, including a global pandemic, as well as beautiful and unforgettable memories of getting married. It has been a roller coaster of emotions, and I love you so much. Levi, our cat, I would like to thank you for waking us up every morning at 4 am for no reason. Your contributions have not gone unnoticed.

I'm thankful for the love and support of my parents, Henda and Arthur, and my in-laws, Michelle and Michele. I love you all. To my sister Nanine and her husband Renier, it is always a great time when we are together. My brother, Harley, you are such an inspiring young man, and I am incredibly proud of the gentleman you have become. Never change. Emma and Kyle, thank you for all of your support. I wish you both a lifetime of love and happiness.

And finally, to all my dearest friends - Craig, Simone, Preeban, Murali, Greg, Matt, Max, and all the boys at MSMK - thank you for all the memories, love and support.

Contents

Declaration of Authorship iii

Abstract vii

Acknowledgements ix

1 Introduction 1
1.1 Transverse Resonator Modes . . . 1
1.1.1 The Paraxial Helmholtz Equation . . . 1
1.1.2 Optical Resonators . . . 2
1.1.3 The Fundamental Gaussian Mode . . . 4
1.2 Higher-Order Transverse Modes . . . 5
1.2.1 Laguerre-Gaussian Modes . . . 6
OAM beams . . . 7
1.2.2 Hermite-Gaussian Modes . . . 7
Mode converters . . . 8
1.2.3 Vector Transverse Modes . . . 9
Vector Vortex Beams . . . 9
1.3 Beam Shaping . . . 10
1.3.1 Static Beam shaping . . . 10
1.3.2 Dynamic Beam shaping . . . 11
Spatial Light Modulators . . . 11
Digital Micromirror Devices . . . 11
1.4 High-Power Higher-Order Transverse Modes . . . 12
1.4.1 Intra-Cavity Generation . . . 13
Pump Beam Shaping . . . 13
Off-Axis pumping . . . 13
Mirror-Defects . . . 13
Interferometrically . . . 14
Spherical Aberration . . . 14
Birefingence and Thermal-effects . . . 14
Spatial-Light Modulator . . . 14
Geometric Phase Optics . . . 15
Integrated Mode Emitters . . . 15
1.4.2 Extra-Cavity Generation . . . 15
Spiral Phase Plates . . . 15
Spatial-Light Modulators . . . 16
Digital-Micromirrored-Devices . . . 16

Modal Phase Plate . . . 16
1.5 Solid-State Amplifiers . . . 16
1.5.1 Basic Theory . . . 16
1.5.2 MOPAs . . . 18
1.5.3 Amplification of Higher-Order Transverse modes . . . 19
1.6 Motivation . . . 19

2 3D modelling of End-Pumped MOPAs 21
2.1 Introduction . . . 21
2.2 Theory . . . 23
2.2.1 Pump Beam Modelling . . . 24
Contra-Propagation . . . 25
Co-Propagation . . . 26
2.2.2 Absorption Cross-Section . . . 26
2.2.3 Gain and Absorption coefficients . . . 27
2.2.4 Temperature-Gradient . . . 28
2.2.5 Change in refractive-index . . . 30
2.2.6 Beam Propagation Method . . . 31
Initialisation of Pump and Seed Fields . . . 31
Iterative procedure . . . 32
2.3 Experimental Setup . . . 33
2.4 Results and Discussion . . . 35
2.4.1 MMFC Diode Vs FT-Gaussian Spatial Transformation Comparison . . . 35
2.4.2 Absorption cross-section calibration . . . 36
2.4.3 SG of order n fitted to FT-Gaussian for $\Delta T(r, z)$ calculation . . . 37
2.4.4 FT-Gaussian vs SG thermal gradient . . . 39
2.4.5 Change in Refractive Index . . . 39
2.4.6 Amplification Performance . . . 40
2.5 Conclusion . . . 43

3 Amplification of higher-order Laguerre-Gaussian modes using a dual-pass MOPA system 45
3.1 Introduction . . . 45
3.2 Theory . . . 47
3.2.1 End-pumped MOPA designs . . . 47
3.2.2 Overlap Integral . . . 49
3.3 Experimental Setup . . . 49
3.3.1 LG_p^l mode selection using the SLM . . . 50
3.3.2 Dual-pass MOPA system . . . 51
3.4 Results and Discussion . . . 52
3.4.1 Amplified LG_p^l Mode Outputs . . . 52
3.4.2 Output Power Results . . . 52
3.4.3 Pump-Seed Intensity Overlap . . . 55
3.5 Conclusion . . . 56

4 Aberration-induced vortex splitting in amplified orbital angular momentum beams 57

4.1 Introduction . . . 57
4.2 Theory . . . 58
4.2.1 Wavefront Aberrations . . . 58
4.2.2 Modal Decomposition . . . 59
4.2.3 Gouy Phase in astigmatic systems . . . 60
4.3 Experimental Setup . . . 60
4.4 Results and Discussion . . . 61
4.4.1 Pump beam distortion . . . 61
4.4.2 Analysing the thermal aberrations . . . 63
4.4.3 How does this affect OAM beams ? . . . 63
4.4.4 Analyzing the Splitting . . . 64
4.4.5 Modal content . . . 65
4.4.6 Amplification Results . . . 69
4.5 Conclusion . . . 70

5 Conclusion **73**
5.1 Future Work . . . 74
5.1.1 Amplification of a propagation invariant vector flat-top beam . . . 74
5.1.2 Further Power-Scaling with Slab MOPAs . . . 77
5.1.3 Thermal Beam Shaping . . . 78
5.1.4 Conclusion . . . 78

Bibliography **81**

List of Figures

1.1 Schematic diagram showing the basic components and working principle of a laser. . . . 3
1.2 A schematic diagram of a Gaussian beam (left) confocal resonator design, consisting of two mirrors (magenta) with equal curvatures ρ separated by length L, with Figure insets (bottom) showing the transverse intensity profile at various positions inside the resonator. . . . 5
1.3 Grid plot showing the first nine Laguerre-Gaussian LG_p^l modes of equation 1.9, for the l, p=0, 1, 2 indices, with a) depicting the normalized transverse intensity and corresponding b) phase profiles. . . . 6
1.4 An illustration of the azimuthally varying phase profile of an LG mode containing topological charges of a) $l = 1$ and b) $l = 2$. The red arrow indicates the direction of the $0 \rightarrow 2\pi$ magnitude phase ramp. . . . 7
1.5 Grid plots showing the first nine Hermite-Gaussian $HG_{n,m}$ modes of equation 1.10, for the n, m=0, 1, 2 indices, with a) depicting the normalized transverse intensity and corresponding b) phase profiles. . . . 8
1.6 Schematic diagram showing the transformation from an $HG_{1,0}$ to LG_0^1 mode using a $\pi/2$ astigmatic mode converter configuration. . . . 8
1.7 The poles of the HOPS represent the RCP and LCP basis states and the opposing equatorial points are the radially and azimuthally polarization states, respectively. All intermediate points between the poles and equator are elliptically polarized states [50] . . . 9
1.8 3D SEM cross-section pictures of a) Higher-order LG phase plate, b) Fresnel lens and c), Bragg grating coupler. Images courtesy of Raith Nanofabrication. 10
1.9 a)A liquid-crystal spatial light modulator screen is shown with a zoomed-in view of individual pixels [76]. b)Individual micromirrors in "on" and "off" states. Reprinted with permission from SPIE [77] . . . 12
1.10 a) Schematic diagram showing an input beam with intensity I_0 passing through an externally pumped solid-state crystal (magenta) to emerge with an increased output intensity $I(z)$. While b) illustrates the two gain regions of an amplifier, above and below the saturation intensity I_{sat}, under steady-state pumping conditions. Where L_{sat} is the length of the crystal required to reach I_{sat}. . . . 17
1.11 Schematic diagram depicting the a) side- and b) end-pumping MOPA configurations. . . . 18

2.1 Illustration of the spatial evolution of a typical MMFC pump beam (red) propagating through a crystal material (magenta cylinder), with co- and contra-propagating seed beams (green arrows). . . . 24

2.2 Initial Gaussian beam modulated by the phase of DOE_1 that transforms into a FT beam $\Psi_{FT}(r)$ at the Fourier plane of lens f, used for a contra-propagation simulation. 25
2.3 FT beam $\Psi_{FT}(r)$ modulated by the phase transformation of DOE_2 that reverses the transformation process back to the original Gaussian beam $\Psi_G(r)$ at the Fourier plane of lens f, used for a co-propagation simulation. 26
2.4 Absorption cross-section of Nd:YAG crystal (black) and emission spectrum of the pump diode (red) with resulting weighted overlap integral (blue shaded area). 27
2.5 Schematic diagram of an end-pumped (blue arrows) laser rod (magenta) of radius R and length L mounted inside a copper heatsink (brown) with red arrows indicating the radial direction of heat flow. 29
2.6 The schematic diagram illustrates the split-step iterative procedure for the pump beam (red) and seed beam (green) in a contra-propagating configuration, where the pump beam travels from right to left and the seed beam travels from left to right. 32
2.7 Schematic diagram of the single-pass end-pumped experimental configuration. 34
2.8 The figure illustrates a comparison between the FT-Gaussian beam shaping profiles (represented by dash-dot lines) and the measured MMFC diode output (indicated by markers) at various points along the free-space propagation corresponding to the crystal length, specifically at $z = 0$, $L/4$, $L/2$, $3L/4$, and L. The inset of the figure displays the experimental 2D intensity profiles of the MMFC pump beam measured at $z = 0$, $L/4$, $3L/4$, and L, labeled as a, b, c, and d, respectively. 35
2.9 Plot a) shows the experimentally measured ($\pm$ 0.1 nm error bars) central wavelength λ_0 (left axis, black) and spectra bandwidth $\Delta\lambda$ (right axis, magenta), with the optimal values used in the simulation (asterisk). Plots b) and c) are experimentally measured (black asterisk) and simulated (magenta circles) values of the transmitted and input pump beam powers, respectively. 36
2.10 2D simulation, using the calibrated absorption cross-section calculation method, of the absorption into the crystal for the Gaussian-FT evolving pump beam at maximum pump power P_p= 38 W. 38
2.11 Gaussian-FT pump beam (solid) compared to the "best fit" super-Gaussian SG^n (dotted) used in the calculation of $\Delta T(r, z)$. 38
2.12 3D (top row), 2D (middle row) and 1D (bottom row) visualisation of the thermal gradient $\Delta T(r, z)$ inside the Nd:YAG crystal using the SG^n approximations of the FT-Gaussian transformation pump beam. 40
2.13 3D (top row), 2D (middle row) and 1D (bottom row) visualisation of the thermal gradient $\Delta T(r, z)$ inside the Nd:YAG crystal as a result of end-pumping by a non-diverging super-Gaussian beam (left column) versus the FT-Gaussian transformation pump beam (right column). 41
2.14 Comparative plot showing the change in refractive index $\Delta n(r, z)$ caused by the non-diverging super-Gaussian beam of order n=20 (dotted lines) and the FT-Gaussian transformation pump beam (solid lines), respectively, at $z = 0$, $L/4$, $L/2$, $3L/4$ & L positions of the crystals. 42
2.15 The red, magenta and black plot colors represent the 3D SG, 2D SG and FT-Gaussian pump beam models, respectively. 42

3.1 Schematic diagrams showing the various solid-state crystal (magenta) end-pumped MOPA configurations to achieve single-pass and/or dual-pass amplification. a) Single and b) dual-pass MOPA configurations for an unpolarized input beam using a dichroic mirror (yellow rectangles). Diagrams c) and d) are dual-pass configurations of linearly polarized input beams, requiring polarization-based optics such as half-wave plates, quarter-wave plates (thin red rectangle), and polarizing beam splitter cubes (light blue square). The Fibre-coupled diode laser pump beam (shaded red) is imaged using a single lens (light blue) into the MOPA system. The output coupler (grey rectangle) of the laser resonator is shown and the broken line indicates subsequent beam shaping and/or optical components. 48
3.2 Schematic diagram showing a) the master oscillator and beam shaping setup using the spatial light modulator with $4f$ spatial filtering, and b) a detailed optical layout of the novel dual-pass end-pumped MOPA setup used in the experiment. 49
3.3 Experimental data showing the spatial profiles of the various LG_p^l modes selected using complex-amplitude shaping on a spatial-light modulator before undergoing dual-pass amplification, with the radial cross-section shown as the green profile. The Laguerre polynomial orders are given in the insets. 50
3.4 Schematic diagram depicting a) the spatial evolution and beam size of the fibre-coupled diode laser pump beam at the entrance (ω_i) and exit (ω_f) faces of the Nd:YAG crystal rod, and b) the simulated "unfolded" layout of the dual-pass MOPA experiment. 51
3.5 Spatial profiles of the various LG_p^l modes after dual-pass amplification at 38 W of pump power, with the radial cross-section shown in green. 53
3.6 a) Numerically simulated amplification results and b) the experimentally measured output powers for single (solid lines) and dual-pass (dotted lines) amplification of the LG_p^l modes with incident powers $P_\mathrm{s} = 100$ mW at input pump powers ranging from $P_\mathrm{p} = 6$ W - 38 W. 54
3.7 Simulated results showing the trend of the normalized output powers versus the normalized overlap integrals of each LG_p^l mode. 56

4.1 Schematic diagram showing the experimental layout with figure insets (top) showing the pump intensity profile (not to scale) measured at various z-positions of the Nd:YAG crystal (pink) with (green) ellipticity values (ϵ). The circled figure inset (bottom right), schematically depicts the cross-section of the fixed pump ω_p (red circle) and varying seed ω_s (blue circles) beam sizes at the pumped face of the crystal ($z = 0$ mm). 59
4.2 Ray Optics Simulation depicting the difference in the incident angles (α_A & α_B) between the outer rays (points A & B) of the pump beam (yellow) normal to the dichroic mirror (grey), resulting in a distorted pump beam at the focal plane. 62
4.3 A bar plot showing the Zernike coefficients C_n^l of the thermally-induced wavefront aberrations for incident pump powers P_p of 25 W (black), 40 W (purple) and 60 W (blue), respectively. The figure inset shows the corresponding reconstructed phase profiles of the wavefront aberration for the pump powers ϕ_{P_p}. 62

4.4 Experimental results (top row) of the LG_0^2 OAM modes with $\beta = 0.5$ (left grid), 0.8 (middle grid) and 1 (right grid) after interaction with the thermally-induced pump $P_p = 60$ W aberration, measured at positions O_1 (left column), O_2 (middle column) and O_3 (right column) with corresponding simulated results of the beam intensities (middle row) and phases (bottom row). 64
4.5 Graph showing the simulated (solid lines) behaviour of Γ through the focus of lens L_2 for $\beta = 0.5$ (purple), 0.8 (yellow) and 1 (red), with experimentally measured Γ values plotted as error bars. An example (right) of the algorithm used to locate (red crosses) the intensity minima (top) with correlation to the phase singularities (bottom) used to calculate d_{sep}. 65
4.6 Computational modal decomposition results (top) in the $HG_{n,m}$ basis of LG_0^2 modes for $\beta = 0.5$, 0.6, 0.7, 0.8, 0.9, 1 aberrated by phase $\phi_{60\,W}$, with insets showing the corresponding split OAM spatial profiles. (bottom) Traces of the main constituent $HG_{n,m}$ modes in the bar plot increase (solid lines left axis) and decrease (dashed lines right axis) as a function of β. 66
4.7 Differences in Near-Field and Far-Field. In the top figure insets, we see the transverse intensity and phase profiles of the simulated and reconstructed aberrated beam, alongside their modal weightings. The middle and bottom plots show the evolution of the Gouy phase of the three different mode orders that possess relevant weightings. Blue(green) lines connecting blue(green) and orange lines show the difference between the phases, and the light blue(green) lines on the bottom are the length of each corresponding line showing the module of the difference between the phases. 67
4.8 The output powers of the LG_0^2 higher-order OAM modes (marked with black asterisks) and a comparison with the fundamental Gaussian LG_0^0 mode (marked with black crosses) were measured experimentally for β values of 0.5 (red), 0.8 (yellow), and 1 (purple). An exponential fit was applied to the experimental data points for both the LG_0^2 (represented by solid lines) and the LG_0^0 modes (represented by dashed lines). The right figure insets display the transverse beam intensity profiles at the maximum pump power $P_p = 60$ W for the LG_0^2 (left column) and LG_0^0 (right column) modes for different β values, including the ellipticity values (marked in green) for the LG_0^0 outputs. 69

5.1 Intensity plot of the VFT beam (magenta) produced by the superposition of a vortex LG_0^1 mode (red) and a Gaussian LG_0^0 mode (blue), with equal amplitude weighting $\alpha = 0.5$. 75
5.2 Mach-Zehnder interferometer comprising of two polarizing beam splitters (PBS) to used to create a VFT beam at the output. 76
5.3 Amplification outputs of the end-pumped solid-state amplifier system. The solid lines and shaded region represents the simulated power levels where the upper and lower bands account for ±5% fluctuations in power measurements. The experimental data, shown as asterisks, are for the input VFT power of a) 100 mW and b) 1 W, while the figure insets are the intensity profiles, with 1D trace in green, of beams at the maximum amplified power. 77
5.4 Figure illustrating multi-pass MOPA systems utilizing a) thin disk [266] and b) slab gain medium [267] geometries to achieve high gain amplification. . . . 78

List of Tables

2.1 Summary of Nd:YAG properties: The parameters marked with superscripts 'a' and 'b' were obtained from references [176] and [157], respectively, while parameter 'c' was calculated using the method outlined in reference [156]. . . 34

3.1 Summary of Nd:YAG crystal properties used in the simulation. 52
3.2 Experimentally measured beam quality M^2 factors of the LG_p^l modes Before and After dual-pass amplification at $P_p = 38$ W. Theoretically, the beam quality values scale according to $M^2 = 2p + |l| + 1$. 53
3.3 A summary of the simulated and experimentally measured single (SP) and dual-pass (DP) amplified output powers P_s of the various LG_p^l modes at maximum pump power $P_p = 38$ W with the relative % error between the simulation and experimental data in the last two columns. The data has been arranged in descending order of the simulated dual-pass output power P_s. The theoretical M^2 values are provided in the column adjacent to the corresponding LG_p^l modes. 55

List of Publications

1. Harrison, J., Forbes, A. & Naidoo, D. "Amplification of higher-order Laguerre-Gaussian modes using a dual-pass MOPA system." Optics Express. ISSN: 1094-4087. https://opg.optica.org/oe/abstract.cfm?doi=10.1364/OE.483373 (2023).
2. Harrison, J., Buono, W. T., Forbes, A. & Naidoo, D. "Aberration-induced vortex splitting in amplified orbital angular momentum beams." Optics Express. (In print).

For my loving wife, Melissa.

Chapter 1

Introduction

1.1 Transverse Resonator Modes

This section presents a concise mathematical derivation of the paraxial Helmholtz approximation from Maxwell's electromagnetic wave equation, with the Kirchoff integral equation that defines the eigenmode solutions of an optical resonator. These concepts lead to the fundamental transverse eigenmode solution in free space, also known as the Gaussian mode. The importance and properties of the Gaussian mode are emphasized, along with key concepts related to optical modes in general that will be significant throughout the dissertation.

1.1.1 The Paraxial Helmholtz Equation

In 1864, on the back of his famous collated equations for electromagnetism, Sir James Clerk Maxwell derived one of the most important and elegant equations in modern physics, the electromagnetic wave equation, the mathematical framework describing light propagation in space and time [1]:

$$\left(\nabla^2 - \frac{1}{c^2}\frac{\partial^2}{\partial t^2}\right)\tilde{\mathbf{E}}(\mathbf{r},t) = 0, \tag{1.1}$$

where, $\nabla^2 = \frac{\partial^2}{\partial x^2} + \frac{\partial^2}{\partial y^2} + \frac{\partial^2}{\partial z^2}$ is the Laplacian operator in cartesian coordinates, c is the speed of light in a vaccum and $\tilde{\mathbf{E}}(\mathbf{r},t)$ is the electromagnetic field vector. A popular textbook solution to the wave equation is a plane wave travelling in the z-direction with the electric-field vector oscillating in the $\hat{\mathbf{x}}$ and $\hat{\mathbf{y}}$ directions:

$$\tilde{\mathbf{E}}(z,t) = (\tilde{E}_x\hat{\mathbf{x}} + \tilde{E}_y\hat{\mathbf{y}})e^{-i(kz+wt)}, \tag{1.2}$$

where k, w, z and t are the wavenumber, angular frequency, position and time, respectively. $\tilde{E}_x = E_x^0 e^{i\phi}$ and $\tilde{E}_y = E_y^0 e^{i\phi}$ are the complex amplitudes with phase ϕ, which define the polarization state of the electromagnetic field. Although plane waves do not exist physically, they do share some resemblance with real laser beams, however, unlike plane waves, laser light cannot exist as an infinite uniform "sheet" of propagating light, but rather must be spatially confined.

To obtain solutions of the wave equation, which describes laser light that is spatially confined, we start by separating the spatial and time-dependent variables of the electromagnetic field so that $\tilde{\mathbf{E}}(\mathbf{r},t) \equiv \tilde{\mathbf{E}}(\mathbf{r})\tilde{E}(t) = \tilde{\mathbf{E}}(\mathbf{r})e^{-iwt}$. Substituting into equation 1.1, one can easily obtain

the time-independent Helmholtz equation:

$$\left(\nabla^2 + k^2\right)\tilde{\mathbf{E}}(\mathbf{r}) = 0, \tag{1.3}$$

where $k = w^2/c^2$ with the complex spatial variable $\tilde{\mathbf{E}}(\mathbf{r}) = \tilde{\mathbf{E}}^{\mathbf{0}}(\mathbf{r})e^{-ikz}$. Next, we assume that the amplitude and phase of $\tilde{\mathbf{E}}^{\mathbf{0}}(\mathbf{r})$ vary slowly over some distance z which is much larger than the wavelength, such that $\frac{\partial^2\tilde{\mathbf{E}}^{\mathbf{0}}(\mathbf{r})}{\partial z^2} \ll k\frac{\partial\tilde{\mathbf{E}}^{\mathbf{0}}(\mathbf{r})}{\partial z} \ll k^2\tilde{\mathbf{E}}^{\mathbf{0}}(\mathbf{r})$. Now, from the Helmholtz equation 1.3, applying the slowly varying z approximation and after some algebraic steps [2] one arrives at the paraxial Helmholtz equation [3]:

$$\left(\nabla_\perp^2 - 2ik\frac{\partial}{\partial z}\right)\tilde{\mathbf{E}}(\mathbf{r}) = 0, \tag{1.4}$$

where $\nabla_\perp^2 = \frac{\partial^2}{\partial x^2} + \frac{\partial^2}{\partial y^2}$ are the transverse partial derivatives perpendicular to the propagation direction. The paraxial wave equation is a partial differential equation that describes the propagation of laser beams in the direction of the optical axis. The solution of equation 1.4 provides a mathematical representation of a laser beam's electric field $\tilde{\mathbf{E}}(\mathbf{r})$ and intensity distribution $\mathrm{I(r)} = |\tilde{\mathbf{E}}(\mathbf{r})|^2$ as it propagates in free space. In the following section, we discuss the basic concept of the optical resonator and how it gives rise to natural solutions to the paraxial wave equation.

1.1.2 Optical Resonators

Radiative energy conservation in atoms is described by the three Einstein coefficients: stimulated emission, spontaneous emission, and absorption [4]. His seminal work revolutionised our understanding of light interactions with atoms and set the stage for over a century of scientific advancement. Perhaps the most important, was the LASER, the abbreviation for Light Amplification by Stimulated Emission Radiation, first demonstrated by Theodore Maiman and featured as a single-page in the Nature Journal on August 8, 1960, titled; "Stimulated Optical Radiation in Ruby" [5]. More than 60 years on, the laser has evolved into a tremendous variety of complex instruments that have advanced all aspects of the natural and medical sciences, industrial engineering, and global communication, each requiring lasers with unique spatial, temporal, spectral, and power characteristics.

Regardless of their complexity or output characteristics, all lasers share three fundamental components: a gain medium, an optical cavity, and an external energy source, schematically depicted in Figure 1.1.

A common example of a gain medium is a transparent solid-state material (magenta) doped with rare-earth ions that can be energized by an external energy source, typically the emission from a semiconductor diode laser (blue wavey arrows). To explain the fundamental concept of a laser we simplify the number of energy levels in the rare-earth ions to only two (i.e. E_l & E_u), as indicated on the crystal of Figure 1.1. Einstein stated that if an electron (blue dots) is promoted from a lower energy level E_l to a higher E_u energy level via absorption (blue arrow) of a photon, then it will return "spontaneously" in time to the lower state E_l (green arrow), and in doing so, emit a photon of energy $\Delta\mathrm{E} = \mathrm{E}_u$ - E_l (red wavey arrow) to obey the conservation of energy law. Furthermore, Einstein stated that if a spontaneously emitted photon encounters an excited electron residing in E_u, then it can instantaneously "stimulate"

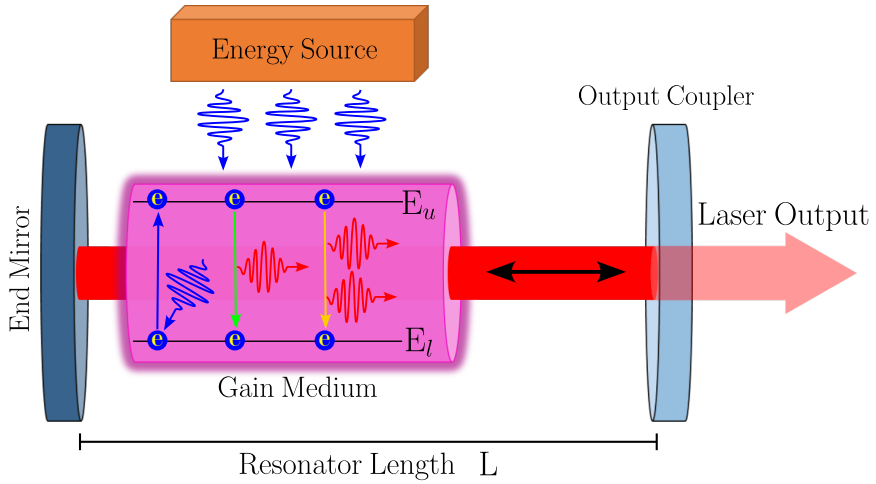


FIGURE 1.1: Schematic diagram showing the basic components and working principle of a laser.

that electron to transition to the lower energy state (yellow arrow) and produce an identical photon replica of itself, thus growing exponentially as it transits the crystal volume.

An example of an optical cavity is the Fabry-Perot resonator, which typically consists of two mirrors - one highly reflective and one partially reflective - separated by a distance L. For a ray of light that enters a Fabry-Perot resonator, it will remain confined between the mirrors after an infinite number of round-trip reflections. Such optical systems are generally referred to as stable resonators. In laser resonator design, the g-parameter is used to determine the conditions for a stable two-mirror resonator to exist [6]:

$$g_i = 1 - \frac{\mathrm{L}}{\rho_i} \quad \& \quad 0 < g_1 g_2 < 1, \tag{1.5}$$

where $i = 1, 2$ represents each mirror, ρ_i is the radius of mirror curvature ($\rho = \infty$ for flat mirrors), and L is the distance between the mirrors. All combinations of mirror geometries and cavity lengths, of which there are many, that satisfy the above constraint are considered to be stable resonators, detailed examples can be found in reference. Outside of the constraint values $0 < g_1 g_2 < 1$ are the unstable resonators, meaning that an on-axis launched ray of light will eventually be ejected from the system. Stability diagrams, where the x and y axes are hyperbolic functions of the g_1 and g_2 parameters, provide an excellent way to visualize resonator stability regions and assist in the cavity design process and selection of mirror curvature combinations and cavity length [7].

In a stable resonator with an excited gain medium, only one spontaneously emitted on-axis photon is required to seed the lasing action. Each round trip adds more photons to the electromagnetic field, thus increasing the total optical power contained inside the resonator cavity. Assuming that the external energy source supplies a constant source of photons, the optical power in the resonator will reach an asymptote when the rate at which electrons populate E_u is equal to the rate at which they are stimulated to E_l, at which point, the system is in "steady-state" and the optical power transmitted through the partially reflective mirror is constant.

1.1.3 The Fundamental Gaussian Mode

For any stable two-mirror resonator configuration ($0 < g_1 g_2 < 1$), one can solve for the steady-state transverse electric field distribution on each of the resonator mirrors $i = 1, 2$ using the Kirchhoff integral equation [6], which is a scalar solution to the paraxial Helmholtz equation 1.4. Rewriting the electromagnetic field in cartesian coordinates (x, y) and in scalar form, we can express the Kirchhoff integral equation as:

$$\begin{aligned}\gamma\tilde{\mathrm{E}}_i(x_2, y_2) = i\frac{e^{-ikL}}{2Lg_j\lambda}\int\int \tilde{\mathrm{E}}_i(x_1, y_1)\times \\ \exp\left[\frac{-i\pi}{2Lg_j\lambda}\left(G(x_1^2 + y_1^2 + x_2^2 + y_2^2) - 2(x_1x_2 + y_1y_2)\right)\right]\mathrm{d}x_1\mathrm{d}y_1,\end{aligned} \tag{1.6}$$

where $G = 2g_ig_j - 1$ is the "G-parameter" of the two mirror resonator ($i, j = 1, 2$ & $i \neq j$) and γ is a proportionality factor. If the transverse electric field distribution on each mirror remains unchanged during a round trip inside the cavity and is self-repeating, then $\tilde{\mathrm{E}}_i(x, y)$ is an eigensolution of the resonator. In steady-state, the transverse modes oscillating between mirrors $i \leftrightarrow j$ experience diffraction losses equal to $1 - |\gamma|^2$ per round trip [7]. Therefore, the electric fields on either end of the mirror are identical, except for the proportionality factor γ which affects only the amplitude. There are an infinite number of analytical solutions $\tilde{\mathrm{E}}_n(x, y)$ & γ_n to equation 1.6, each corresponding to a unique eigenmode of the resonator, however, the physical constraints of the resonator such as the gain medium shape, symmetry of the excited gain region, thermal-effects, cavity length, mirror geometry, and curvature, etc., all dictate the steady-state eigenmode solution.

The first steady-state eigensolution of equation 1.6 in a stable resonator cavity is the fundamental transverse mode, commonly referred to as the Gaussian beam [8]. The Gaussian laser beam is radially symmetric, with its intensity distributed in a bell-shaped curve that peaks on the optical axis, expressed mathematically as:

$$E(r, z) = E_0\frac{\omega_0}{\omega(z)}\exp\left(-\frac{r^2}{\omega^2(z)}\right)\exp\left(-i\frac{kr^2}{2R(z)}\right)\exp(i\xi(z)), \tag{1.7}$$

where E_0 is a constant defining the maximum electric field amplitude and ω_0 is the beam waist radius. The parameters that vary as a function of the longitudinal position z are the beam radius $\omega(z)$, the wavefront radius of curvature $R(z)$ and Gouy phase $\xi(z)$, mathematically written as:

$$\omega(z) = \omega_0\sqrt{1 + \left(\frac{z}{z_R}\right)^2}, \quad R(z) = z\left[1 + \left(\frac{z_R}{z}\right)^2\right], \quad \xi(z) = \arctan\left(\frac{z}{z_R}\right).$$

The parameter $z_R = \pi\omega_0^2/\lambda$ is the Rayleigh length or Rayleigh range, which is the distance from the beam waist where the beam radius increases by a factor of $\sqrt{2}$.

The schematic depicted in Figure 1.2 corresponds to a confocal stable Gaussian beam resonator, where both mirrors located at each end of the resonator have the same radius of curvature, denoted by ρ_i, and are separated by a distance of L. As illustrated, a Gaussian beam maintains its Gaussian shape while oscillating within the resonator mirrors, but its

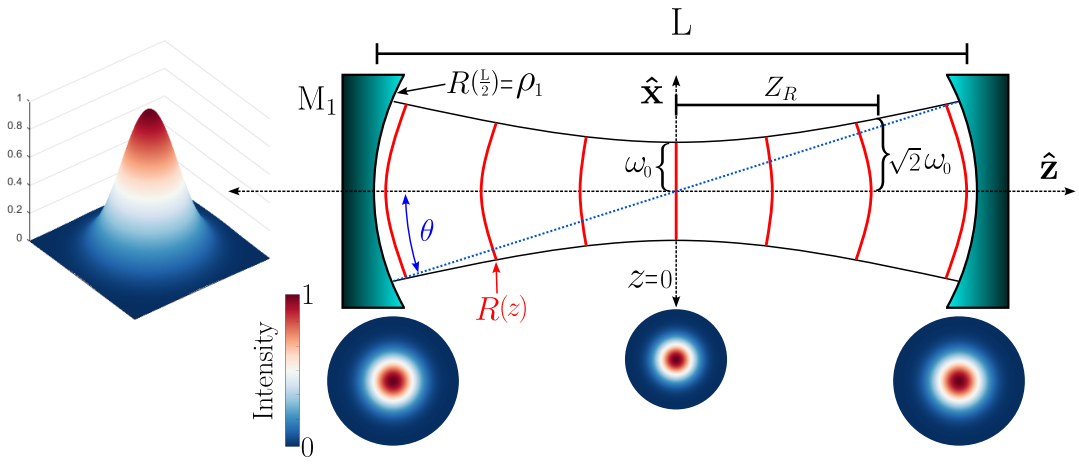


FIGURE 1.2: A schematic diagram of a Gaussian beam (left) confocal resonator design, consisting of two mirrors (magenta) with equal curvatures ρ separated by length L, with Figure insets (bottom) showing the transverse intensity profile at various positions inside the resonator.

characteristics, such as beam radius and wavefront curvature radius, differ at different longitudinal positions. Upon reflection from a curved mirror surface (M_1), the Gaussian beam possesses the same wavefront curvature as the mirror itself, denoted by $R(\mathrm{L}/2) = \rho_i$. This property holds for mirrors of all curvatures, including flat (plane) mirrors that have a radius of curvature extending to infinity, i.e., $\rho = \infty$. As z approaches zero in the confocal resonator illustrated in Figure 1.2, the wavefront curvature (depicted by the red lines) increases so that $R(0)$ tends to infinity. This indicates that the wavefront becomes entirely flat at the beam waist ω_0 position.

The beam propagation factor commonly referred to as the "beam quality" or "M-squared (M^2)" is intrinsically linked to the half angle divergence (θ), indicated by the blue line in Figure 1.2, of a laser beam so that

$$\theta = \mathrm{M}^2 \frac{\lambda}{\pi\omega_0} \tag{1.8}$$

The fundamental Gaussian mode has an M^2=1 and is often referred to as being "diffraction-limited". Since the M^2 and divergence angle θ of equation 1.8 are directly proportional, a unique characteristic of the Gaussian beam is that its radius $\omega(z)$ varies slowly resulting in an extended depth of focus.

1.2 Higher-Order Transverse Modes

There exists an infinite number of solutions to the paraxial Helmholtz equation in a stable resonator, which is determined by the geometry of the gain medium and cavity mirrors. These include circularly, rectangular and elliptical symmetries solutions, corresponding to Laguerre-Gaussian (LG), Hermite-Gaussian (HG) and Ince-Gaussian (IG) mode families, respectively, and expressed in cylindrical (ρ, ϕ, z), cartesian (x, y, z) and elliptical (ξ, η, z) coordinates [9], respectively. Here, the mathematical formulation of the higher-order circular LG and rectangular HG mode families is provided.

1.2.1 Laguerre-Gaussian Modes

The generalized Laguerre-Gaussian LG_p^l eigenmodes are a group of cylindrically symmetrical solutions to the paraxial Helmholtz equation 1.4. These modes have found wide-ranging applications in various fields, including optical tweezers [10–12], trapping [13–15], quantum communication [16–19], free-space [20–23], underwater [24] optical communication, super-resolution microscopy [25–27], and advanced material processing [28–30]. Mathematically, the generalized LG function in cylindrical coordinates (ρ, ϕ, z) is expressed as:

$$\begin{aligned} \mathrm{LG}_p^l(\rho,\phi,z) = \frac{1}{\omega_0}\sqrt{\frac{2p!}{\pi\,(|l|+p)!}}\left(\frac{\sqrt{2}\rho}{\omega(z)}\right)^{|l|} \times \mathrm{L}_p^l\left[2\left(\frac{\rho}{\omega(z)}\right)^2\right] \\ \exp\left[-\left(\frac{\rho}{\omega(z)}\right)^2\right] \times \exp\left[i(2p+|l|+1)\xi(z)\right] \\ \times \exp\left[-\frac{ik\rho^2}{2R(z)}\right]\exp\left[\pm il\phi\right], \end{aligned} \tag{1.9}$$

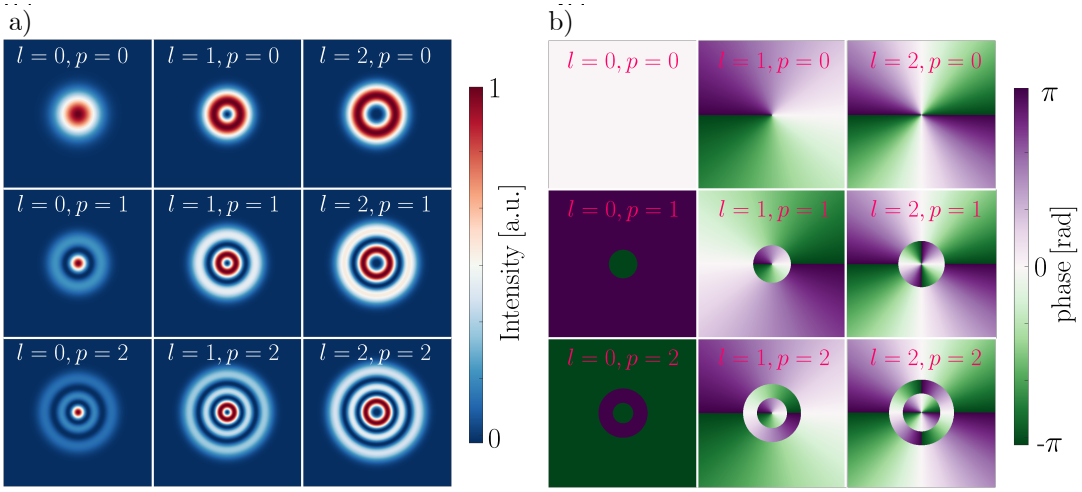


FIGURE 1.3: Grid plot showing the first nine Laguerre-Gaussian LG_p^l modes of equation 1.9, for the l, p=0, 1, 2 indices, with a) depicting the normalized transverse intensity and corresponding b) phase profiles.

where l and p are the azimuthal and radial integers of the L_p^l generalized Laguerre polynomial, which quantifies the topological charge and number of bright intensity rings, respectively. Figure 1.3, shows the a) transverse intensity and corresponding b) complex phase distributions of the first 9 LG_p^l permutations with azimuthal and radial integers $l, p = 0, 1$ and 2 at position $z = 0$. In the top left boxes insets of Figure 1.3 a) and b), when the Laguerre polynomial integers are set to zero (i.e. $l = 0$, $p = 0 \rightarrow \mathrm{LG}_0^0$) we recover the fundamental Gaussian mode with a uniform flat phase profile. The beam radius $\omega(z)$ and the M^2 of the higher-order LG_p^l modes scale according to their azimuthal l and radial p indices as follows:

$$\omega_{(l,p)}(z) = \omega_0\sqrt{2p+|l|+1}, \quad \mathrm{M}^2_{(l,p)} = 2p+|l|+1.$$

where ω_0 is the beam waist radius of the fundamental Gaussian mode.

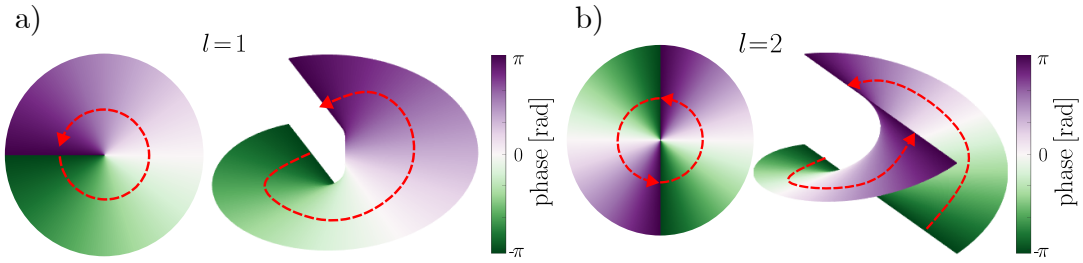


FIGURE 1.4: An illustration of the azimuthally varying phase profile of an LG mode containing topological charges of a) $l = 1$ and b) $l = 2$. The red arrow indicates the direction of the $0 \rightarrow 2\pi$ magnitude phase ramp.

OAM beams

The LG_p^l function of equation 1.9 includes a complex phase term that varies with the azimuthal angle $\exp[\pm il\phi]$. This complex phase imparts a quantized momentum of $\pm l\hbar$ per photon when the azimuthal index is not zero ($|l| > 0$), causing the wavefront to corkscrew as it propagates. The topological charge, given by the magnitude of $|l|$, determines the number of $0 \rightarrow 2\pi$ phase ramps contained in a full azimuthal rotation of the transverse beam profile, which is illustrated in Figure 1.4 for an $l = 1$ and $l = 2$ LG beam. These beams are known as orbital angular momentum (OAM) or vortex beams, and they have a distinct annular intensity profile with a zero-intensity centre where phase singularities exist. The sign of the topological charge, $\pm l$, determines the rotational direction of the corkscrew, which can be either clockwise or anti-clockwise, referred to as left ($l > 0$) and right-handedness ($l < 0$), respectively. The detailed properties of OAM beams are extensively covered in good reviews [31, 32].

1.2.2 Hermite-Gaussian Modes

The paraxial Helmholtz equation 1.4 has rectangular symmetric solutions known as the Hermite-Gaussian $\mathrm{HG}_{n,m}$ modes. These modes have found widespread use in various applications, including free-space optical communication [33–38], optical trapping [39–41], nonlinear optics [42], and electron acceleration [43–45]. Mathematically, HG modes in cartesian coordinates (x, y, z) are expressed as follows:

$$\begin{aligned}\mathrm{HG}_{n,m}(x,y,z) = \frac{1}{\omega_0}\sqrt{\frac{2}{2^{n+m}\pi\, n!\, m!}}\mathrm{H}_n\left(\frac{\sqrt{2}}{\omega(z)}\,x\right)\mathrm{H}_m\left(\frac{\sqrt{2}}{\omega(z)}\,y\right) \\ \exp\left[-\frac{x^2+y^2}{\omega(z)^2}\right]\exp\left[i\xi_{n,m}(z)\right]\exp\left[-\frac{ik(x^2+y^2)}{2R(z)}\right].\end{aligned} \tag{1.10}$$

Here, H_j is the Hermite polynomial of order j for the n, m indicies. As before, $\omega(z)$ and $R(z)$ are the beam radius and wavefront radius of curvature at position z, while the Gouy phase term $\xi_{n,m}(z) = (n + m + 1)\arctan(z/z_R)$. Figure 1.5, shows the a) transverse spatial intensity and b) complex phase distributions of the first 9 $\mathrm{HG}_{n,m}$ permutations of the n, m indices at position $z = 0$. As was the case of the LG modes, we recover the fundamental Gaussian mode when the indices n, m are set to zero (i.e. $\mathrm{HG}_{0,0}$). The rectangular symmetry of $\mathrm{HG}_{n,m}$ modes results in an independent scaling of M^2 and beam size along the x- and y-directions based on the n and m indices, respectively. We can generalize the variations of the

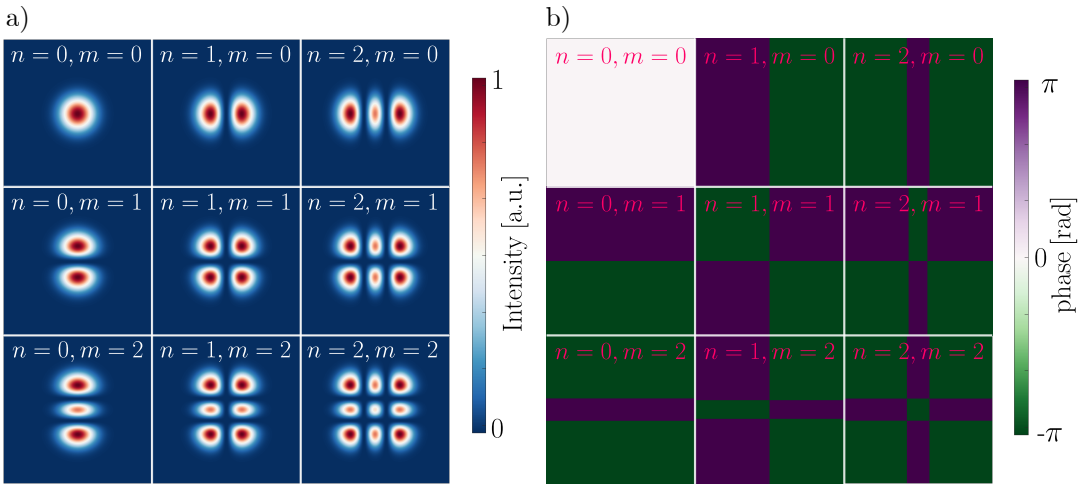


FIGURE 1.5: Grid plots showing the first nine Hermite-Gaussian $\mathrm{HG}_{n,m}$ modes of equation 1.10, for the n, m=0, 1, 2 indices, with a) depicting the normalized transverse intensity and corresponding b) phase profiles.

$\mathrm{HG}_{n,m}$ beam size and M^2, with respect to the Gaussian as follows:

$$\omega_j(z) = \omega_0\sqrt{2j+1}, \quad \mathrm{M}_j^2 = 2j+1, \quad \text{for} \quad j = n, m,$$

where ω_0 is the beam waist radius of the fundamental Gaussian mode. Here, $\omega_j(z)$ is the axis specific ($j = x, y$) beam radius as a function of distance z with corresponding M_j^2 value.

Mode converters

The HG field of equation 1.10 does not have an azimuthal term $\exp[\pm il\phi]$ and therefore does

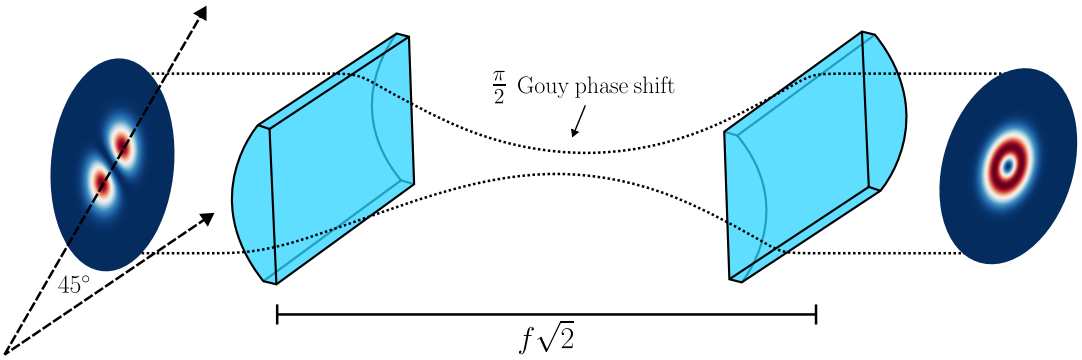


FIGURE 1.6: Schematic diagram showing the transformation from an $\mathrm{HG}_{1,0}$ to LG_0^1 mode using a $\pi/2$ astigmatic mode converter configuration.

not possess OAM. However, it is possible to convert, for example, an $\mathrm{HG}_{1,0}$ mode with a spherical wavefront into an LG_0^1 mode with a helical wavefront possessing OAM. This can be accomplished using an astigmatic mode converter (AMC), which consists of a pair of cylindrical lenses with focal length f, as shown in Figure 1.6. The input $\mathrm{HG}_{1,0}$ mode is angled at 45° with respect to the cylindrical lens to induce a relative Gouy phase shift of $\pi/2$ between the two intensity lobes, resulting in an LG_0^1 beam after the second cylindrical lens placed exactly $f\sqrt{2}$ from the first lens [46]. Passing an $\mathrm{HG}_{n,m}$ mode with indices m and n through a $\pi/2$ mode converter results in an LG_p^l mode with azimuthal index $l = n - m$ and radial index $p = \min(n, m)$. Additionally, the induced Gouy phase shift can vary from $\pi/2$

to π by varying the separation between the cylindrical lenses from $f\sqrt{2}$ to $2f$, which reverses the sign of the topological charge l in the output LG mode. The AMC is a vital tool for generating and characterizing LG modes [47] and will be discussed more in the generation section of the dissertation.

1.2.3 Vector Transverse Modes

The state of polarization of light is determined by the oscillation direction (linear, circular, or elliptical) of the electric field vector as it propagates [48]. Laser beams can be classified as scalar polarized beams, or "scalar beams", when all electric field vectors have the same polarization state. On the other hand, if the polarization state of the laser varies across the beam, it is known as a vector polarized beam, or "vector beam". Vector beams, or VBs, can occur naturally within a laser resonator, as they are solutions to the vectorial paraxial Helmholtz equation, but they can also be generated outside of a resonator by combining two orthogonally polarized scalar transverse modes. To mathematically represent the polarization distribution of a vector field, it is necessary to first establish an orthogonal basis that forms a complete set of linearly independent vectors. When mathematically describing such a vector field $|\Psi\rangle$, it is beneficial to use Bra-Ket notation:

$$|\Psi\rangle = \sqrt{\alpha}\,\psi_{\mathrm{R}}\,|\mathrm{R}\rangle + \sqrt{1-\alpha}\,\psi_{\mathrm{L}}\,|\mathrm{L}\rangle\,, \tag{1.11}$$

where ψ_{R} and ψ_{L} are two complex scalar transverse modes, with normalized amplitude coefficient α. Here, we used the right and left circular polarization states (RCP and LCP), represented as $|\mathrm{R}\rangle$ and $|\mathrm{L}\rangle$, respectively, as the basis vectors, analogous to how $\hat{\mathbf{x}}$ and $\hat{\mathbf{y}}$ are used in cartesian coordinates. However, one could alternatively opt for horizontal and vertical $\{|\mathrm{V}\rangle, |\mathrm{H}\rangle\}$ or diagonal and anti-diagonal $\{|\mathrm{D}\rangle, |\mathrm{A}\rangle\}$ basis states [48, 49].

Vector Vortex Beams

As a special case of vector beams, we substitute the transverse modes ψ_{R}, ψ_{L} of equation 1.11 with LG_p^l modes, specifically with $\psi_{\mathrm{R}} = \mathrm{LG}_0^{\mp l}$ & $\psi_{\mathrm{L}} = \mathrm{LG}_0^{\pm l}$. This unique superposition state produces cylindrical vector vortex beams (CVVB) [51]. The resulting polarization distribution can be visually represented on a modified higher-order Poincaré sphere (HOPS) [50], as shown in Figure 1.7. Varying the weighting coefficient α from 0 to 1 moves the location on the HOPS longitudinally to the $|\mathrm{L}\rangle$ and $|\mathrm{R}\rangle$ scalar polarization states, respectively, and the equator when $\alpha = 0.5$. The latitudinal variation is achieved by adjusting the relative phase shift ϕ between the two beams, allowing for full motion around the HOPS.

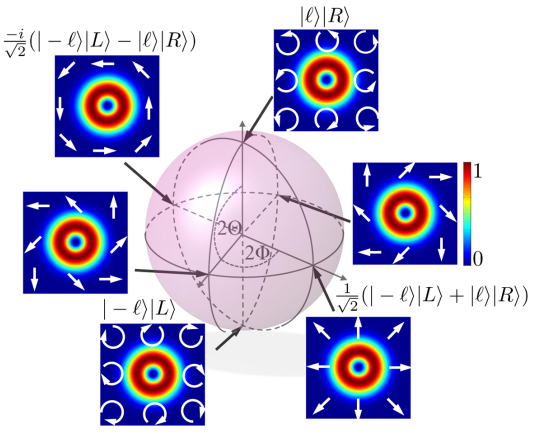


FIGURE 1.7: The poles of the HOPS represent the RCP and LCP basis states and the opposing equatorial points are the radially and azimuthally polarization states, respectively. All intermediate points between the poles and equator are elliptically polarized states [50]

1.3 Beam Shaping

Selecting the modes described in section 1.2 requires manipulation of the amplitude, phase, and/or polarization properties of optical light, known as beam shaping. This can be performed either inside or outside of a laser resonator, known as intra- and extra-cavity generation, respectively [52, 53]. In general, beam shaping requires additional optical elements to modulate the amplitude, phase and/or polarization of the electric field, which can be closely grouped as being either static or dynamic in their beam shaping flexibility. There are other methods for obtaining a desired beam shape, specifically for intra-cavity generation, that can not be categorized as singular optical elements but rather a result of manipulation of the fundamental mode of the resonator. Examples of these include, resonator design, tailoring the pump-beam shape, exploiting thermally-induced aberrations and birefringent properties of materials - examples will be provided in the generation section. Nevertheless, here, we only report on the stand-alone singular static and dynamic beam-shaping devices.

1.3.1 Static Beam shaping

The term "static optical elements" refers to optical components that are designed to carry out a distinct task. These components fall into three primary categories: beam integrators [54], diffractive optical elements (DOEs) [55], and refractors [56], each of which has several subcategories. DOEs are the contemporary approach to beam shaping in modern times and

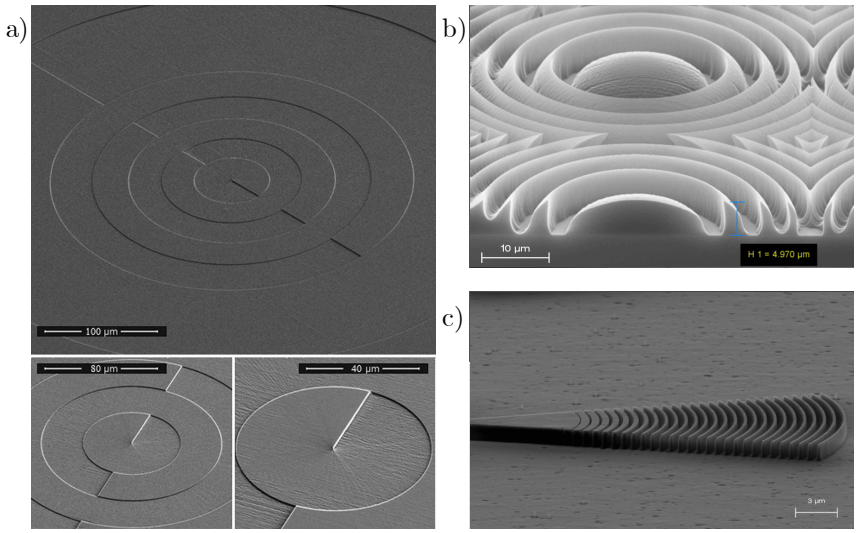


FIGURE 1.8: 3D SEM cross-section pictures of a) Higher-order LG phase plate, b) Fresnel lens and c), Bragg grating coupler. Images courtesy of Raith Nanofabrication.

can be fabricated into complex structures with high precision, as highlighted in Figure 1.8, some of which are used to tailor all properties of the electromagnetic field to achieve any desired transverse mode. Well-known examples of DOEs include: diffractive gratings [57], binary phase gratings [58], fresnel zone plates [59], as well as geometric phase elements such as; spiral phase plates [60, 61], modal phase plates [62], Q-plates [63], S-plates [64], and metasurfaces [65]. The fabrication of DOEs often involves lithographic techniques, which typically entails designing the DOE using computer software, transferring the desired pattern onto a mask, exposing the substrate to light through the mask, developing the exposed photoresist and etching the substrate to transfer the pattern into the material [66]. Over the past two

decades, lithography has undergone significant technological progress, largely propelled by the need for silicon-integrated chips that are more compact, and efficient. The fabrication of DOEs has benefited greatly from these advances, with feature resolutions well below 300 nm readily achievable, resulting in the high-purity selection of higher-order transverse modes.

1.3.2 Dynamic Beam shaping

In contrast to static optical elements, dynamic beam-shaping devices are not limited to a fixed beam transformation and can be digitally reprogrammed in real-time, thus allowing for on-the-fly selection of arbitrary complex phase elements. Liquid-crystal spatial-light modulators (SLMs) [67], digital micromirror devices (DMDs) [68] and deformable mirrors (DMs) [69], are exemplary examples of dynamic optical field manipulating devices.

Spatial Light Modulators

A SLM is a liquid crystal display (LCD) with millions of liquid crystal (LC) cells that can be independently controlled using an externally applied voltage, shown in Figure 1.9 a). Each cell consists of small rice-shaped molecules that are aligned parallel to one another under zero bias and collectively rotate when an external voltage is applied across the cell. The rotation of the molecules corresponds to a specific phase retardance that modifies the phase of the incident light. This allows for precise and controllable phase changes of up to 8π across the beam's spatial profile. Computer-generated holographic images (8-bit) are addressed onto the SLM display as 256-level grey-scale images, ranging from black to white (i.e. $0 \rightarrow 256$) corresponding to a $0 \rightarrow 2\pi$ phase shift. Although SLM displays only modulate the phase of the incident light, they can be used to perform amplitude and phase modulation [70] to select pure transverse modes, such as the LG and HG modes in section 1.2. The diffraction efficiency (DE) of an SLM display defines the percentage of input light transformed into the desired output mode. The level of DE depends on the physical hardware (i.e. fill factor, flickering and fringing effects), type of beam shaping (i.e. phase-only, or complex-amplitude and phase modulation), phase modulation depth, and grating period and structure (i.e sinusoidal or blazed) [71]. Newer SLM devices have ultra-high resolutions, smaller pixel pitch, and higher refresh rates compared to traditional devices. They can achieve resolutions of 4160 x 2464, pixel pitch of 3.1 μm, and refresh rates of 60 Hz [72], with some lower resolution devices capable of refresh rates of 500 Hz [73]. The LC pixels are susceptible to thermal damage, therefore, are limited to input optical powers of around 2 W/cm^2 with newer water-cooled versions capable of 200 W/cm^2 [74]. Therefore, especially for high-power beam shaping, careful selection of the SLM system to manage DE losses and mitigate thermal limitations is required for correct and successful implementation of SLMs.

Digital Micromirror Devices

A DMD is a micromechanical system that comprises highly reflective mirrors, which are comparable in resolution to the SLM displays. Each mirror or "pixel" can independently tilt between $+12°$ and $-12°$, corresponding to "on" and "off" states, respectively, as depicted in Figure 1.9 b). When the mirror is in an "on" state the light falling on the micromirror is reflected along the optical axis and contributes to the "shaped beam", whereas an "off" state is diverted away and discarded from the "shaped beam". Therefore, DMDs are referred to as binary holographic amplitude shaping devices [75]. Although the DMD is an amplitude

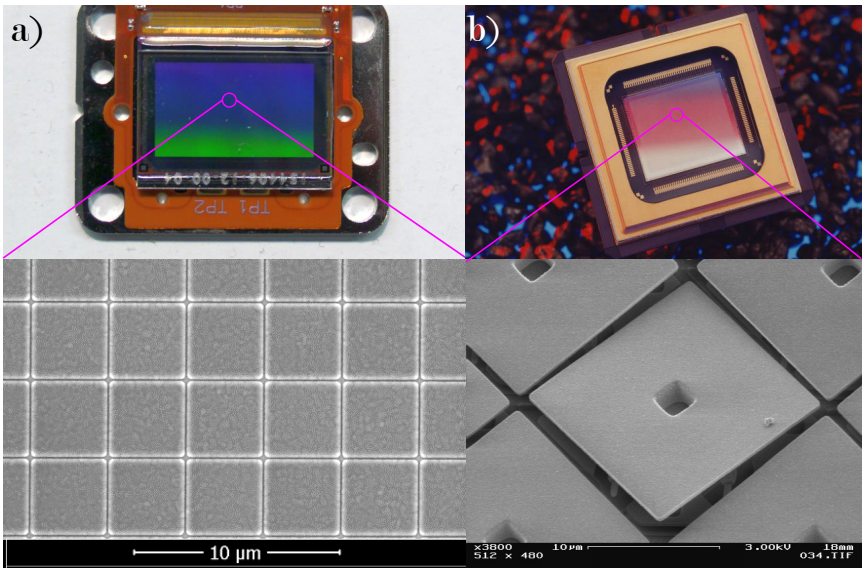


FIGURE 1.9: a)A liquid-crystal spatial light modulator screen is shown with a zoomed-in view of individual pixels [76]. b)Individual micromirrors in "on" and "off" states. Reprinted with permission from SPIE [77]

guiding device, it is possible to achieve complex field modulation of the phase and amplitude through a binary Lee hologram, whereby the continuous greyscale holograms utilized in the SLM are modified to binary values [68]. Modern DMD devices have comparable pixel pitch and resolution to SLM devices, however, the mechanical nature of DMDs grant them a far superior refresh rate, which can exceed 20 kHz, making them well suited for applications requiring rapid wavefront corrections. On the contrary, the simple binary nature of the DMDs systems produces very poor diffraction efficiencies compared to SLMs.

1.4 High-Power Higher-Order Transverse Modes

High-powered laser systems are highly utilized and adept at carrying out complicated operations across multiple industries, including medical procedures, material processing (e.g. cutting, welding, and drilling), additive manufacturing and military defence systems. Typically, commercially sold laser systems have a transverse profile that is restricted to either a Gaussian (single-mode) output or a superposition of multiple modes (multi-mode) to generate a uniform or flat-top profile at the working surface. The shapes produced by commercially available laser systems represent only a tiny fraction of the possible spatial profiles achievable through beam shaping, not to mention the additional polarization and phase degrees of freedom that are generally overlooked. Various studies have demonstrated unique light-matter interactions resulting from vortex modes annular spatial profile, polarization structures, and orbital angular momentum components. For instance, the polarization structure of a vector vortex beam can be transferred directly to a material to generate a textured micro-structured surface that is suitable for advanced material processing and creation of self-disinfecting surfaces [78]. Radially polarized vector vortex beams are highly effective in drilling micro-sized holes and producing near-perfect tapered edges at the output [79]. Additionally, the orbital angular momentum component of vortex beams can be transferred to a material, resulting in the creation of chiral micro-needle structures [30]. These are just a few examples from a small subset of higher-order transverse modes which demonstrate the benefits and vast

potential applications of high-power structured light, over traditional laser beam outputs. Therefore, it is crucial to conduct research on the production of high-power structured light using contemporary beam shaping methods. In the literature, one finds that the high-power generation of higher-order transverse modes is focused primarily on the circular-symmetric Laguerre-Gaussian modes, particularly scalar and vector OAM beams. Additionally, it is customary to generate Hermite-Gaussian modes with the purpose of converting them into Laguerre-Gaussian modes, therefore there is still a lot to explore regarding the benefits of the other higher-order modes. This section summarizes some of the current developments towards achieving high-power structured light, either directly generated from the cavity or created outside the laser cavity using direct beam shaping as well as indirect approaches (i.e. thermal lensing, cavity design, etc.)

1.4.1 Intra-Cavity Generation

Pump Beam Shaping

Creating an annular pump shape is a straightforward and convenient method for selecting circularly symmetric LG modes inside a cavity. This has been demonstrated successfully using capillary fibers [80, 81], Dammann grating binary phase elements [82], and centre-punched pump mirrors [83], to achieve scaler vortex beams with topological charges of $l = 1$ with a few watts of average power output. Annular pumped optical parametric oscillators (OPOs) can provide more dynamic and tunable scalar vortex emission, with topological charges ranging from $l = 1$ to 6, tunable wavelengths over the mid-IR range of 2260-3576 nm, and average power up to 8 W [84]. Digital micromirror devices (DMDs) have also been used to produce pump beam shapes resembling the $\mathrm{HG}_{n,m}$ modes of Figure 1.5, which result in direct lasing of scalar $\mathrm{HG}_{90,0}$ modes that could then be transformed into LG_0^{90} modes using an astigmatic mode converter (AMC) [85, 86].

Off-Axis pumping

Pumping the gain-medium off-axis is another simple method for inducing scalar HG emission from a laser cavity [87]. This simple approach combined with the AMC, is an effective way of generating scalar vortex beams with high topological charges and moderate powers. Recently, a vertical external cavity surface emitting laser (VECSEL) demonstrated direct emission of higher-order scalar HG modes with average powers exceeding 2 W [88]. This setup was later modified to include an AMC inside the laser cavity, enabling the simultaneous emission of both HG and LG scalar modes at low average power (20 mW) [89]. Another interesting effect of off-axis pumping, under certain cavity length constraints, is degenerate laser cavities that can emit multi-axis higher-order scalar HG modes that can be transformed into multi-axis OAM beams using an external AMC [90].

Mirror-Defects

Circular defects on cavity mirrors can also be used to obtain a desired mode in a cavity. In fact, the highest topological charge l scalar vortex emission from an intra-cavity resonator was achieved using an output coupler mirror inscribed with circular markings generated by ablating the coating layer, which produced $l = 288$ vortex emission [91]. The author of a related study claims that this technique can support intra-cavity vortex emission with topological charges of $l > 1000$.

Interferometrically

Recently, a Sagnac interferometric mode transforming vortex output coupler (VOC) was demonstrated. The resonator emitted a 95% pure LG_0^1 mode which is the highest continuous-wave average power (31.1 W) scalar vortex emission achieved from an intra-cavity laser at the time of writing [92].

Spherical Aberration

A novel bounce laser was developed using a simple cavity design with no additional optics, and only exploited the usually unfavourable effects of spherical aberration to achieve an impressive 16 W average power of pure scalar LG_0^1 emission [93]. Other approaches, which also exploited spherical aberration, but used lenses, have demonstrated scalar LG_0^l mode emission up to $l = \pm 33$ with 1.87 W of output power [94]. An improved version of this design allowed for scalar LG_0^l emission up to $l = \pm 95$, but the power was limited to < 140 mW [95].

Birefingence and Thermal-effects

The LG_0^l mode exhibits both radial and azimuthal polarization states inside the cavity simultaneously. However, in the presence of a birefringent material, the S and P-polarization states become decoupled. As a result, one state may suffer a significant loss, while the other can continue to oscillate. This straightforward method of producing either radial or azimuthally polarized vector vortex beams has been well-documented and demonstrated using a c-cut Nd:YVO_4 [96, 97]. In non-birefringent materials, thermal-lens effect-induced bifocusing may occur at output powers in the few watts range. By adjusting the incident pump beam power and the relative position of the crystal to the pump beam focus position, the fundamental cavity oscillation can switch between radial and azimuthal polarization vector vortex modes [98, 99]. When high-power pumping conditions are applied, a strong bifocusing effect can produce vector polarization states with high topological charges, ranging from $l = 1$ to 14 [100]. Recently, a stable, highly pure (95%), and high-power (20 W) radially polarized LG_0^l mode emission at a wavelength of 2090 nm was achieved by utilizing annular pumping, thermally-induced birefringence, and bifocusing effects. This was accomplished by using an end-pumped Ho:YAG crystal with an intra-cavity lens on a translation stage, which was controlled by a machine learning feedback loop [101].

Spatial-Light Modulator

Adding complex diffractive optical devices inside the laser cavity is a more direct approach to selecting higher-order modes. One example of this is the digital laser, which utilized an SLM as an end-mirror and applied a phase mask to control the resonator eigenmode, resulting in arbitrary scalar LG mode outputs [102]. However, due to the low damage threshold of liquid crystal cells and high diffraction losses, the digital laser is limited to producing only a few mW's of power. A few years later, this concept was improved to include the generation of vector vortex beams by inserting a birefringent material into the cavity to separate the s- and p-polarization states. A single phase-only SLM was then used to address each polarization state independently and to select orthogonal HG modes that superimpose on the return pass and produce vector vortex modes with l values of 1 and 2 [103].

Geometric Phase Optics

Recently, an intra-cavity metasurface was used to achieve the highest intra-cavity topological charge output for vector vortex beam. By rotating the metasurface inside the cavity, the laser cavity produced variable topological charge emissions ranging from $l = 10$ to $l = 100$ and demonstrated the first "metasurface assisted laser" [104]. The spatially varying half-wave phase retarders or S-waveplates have been demonstrated to function inside the laser cavity and delivered high-purity vector vortex beams (over 90%) with a moderate slope efficiency (11%) with average output powers < 150 mWs [105]. For the high-power (> 30 W) generation of scalar vortex beams, the concept of fabricating spiral phase structures directly onto the mirrors is promising [106].

Integrated Mode Emitters

To enable the integration of next-generation telecommunications and quantum computing, it is essential to reduce the size of OAM mode-emitting lasers with high topological charges and tunable wavelength outputs. Various techniques can be employed for achieving this objective, including microchip lasers [107, 108], VECSELS [89, 109], and complete micron-sized laser systems [110–112].

1.4.2 Extra-Cavity Generation

Extra-cavity beam shaping devices can easily be added to existing laser systems as a separate modular system to produce the desired optical modes, however, intra-cavity generated modes are intrinsically of high-purity and with better output power. In this section, we highlight the recent advances in the extra-cavity generation of scalar and vector LG and HG modes.

Spiral Phase Plates

A common method for generating scalar vortex beams is to impart the azimuthally varying phase of the LG_p^l function in equation 1.9, onto a Gaussian beam using a spiral phase plate (SPP). SPPs are fabricated to achieve a fixed topological charge, and the higher the desired topological charge the more challenging and expensive the fabrication becomes. However, it is possible to stack or cascade multiple SPPs in series to generate a vortex beam with a high topological charge. This was demonstrated by stacking 6 SPPs (3 times $l = 2$ and 3 times $l = 4$) to create a vortex beam with a total topological charge of $l = 18$. However, the purity of the final OAM beam is compromised due to unoptimized spatial overlap as the beam diverges. A liquid crystal cell-based reprogrammable SPP has been demonstrated as a cost-effective alternative to expensive devices like SLMs for generating high OAM beams. The SPP utilizes 24 pie-sliced segments of liquid crystal cells that allow for selective topological charges of $l = 1, 2, 3, 4, 6, 8$, and 12, while still maintaining a high fill factor since there are no individual pixels. This technology has the potential to be useful in preparing high OAM beams [113]. The spiral phase mirror (SPM) is similar to the SPP but is reflective rather than transmissive, and imparts the same azimuthally varying phase. With the use of an aluminium mirror constructed with 125 segments, each imprinting a phase ramp of 160π, the SPM has achieved the highest topological charge for an OAM beam, with $l = 10000$. This is calculated by multiplying the number of segments by the phase ramp value, resulting in $125 \times \frac{160\pi}{2\pi} = 10010$ [114].

Spatial-Light Modulators

Traditional SLMs with a display resolution of 1920x1080 pixels have been used to generate high-purity scalar vortex beams with a topological charge of up to $l = 600$ [115]. Newer SLMs with a display resolution of 3840x2160 pixels, four times greater than previous models, hav achieved topological charges of $l = 1400$ by following the same optimization process as previous models [116]. SLMs have also been incorporated into Sagnac interferometer design, to produce a highly controllable superposition vector vortex beam with dynamic control over the polaization state. The system demonstrated "perfect" vector vortex beams with topological charges ranging from $l = 1$ to 3 [117].

Digital-Micromirrored-Devices

OAM beams with topological charges as high as $l = 90$ can be generated through binary amplitude modulation and super-pixel resolution optimization [118]. The deformable mirror has the potential to handle much higher power beams (up to a few kW) than DMDs or SLMs. Recently, a continuous surface deformable mirror demonstrated proof-of-concept dynamic generation of OAM with topological charges ranging from $l = 1$ to 5 at low powers. [119].

Modal Phase Plate

To improve the sensitivity of detecting gravitational waves at LIGO, an LG_p^l mode with $l = 3$ and radial modes ($p = 3$) generated at an average power of 130 W, with 97% purity, using a single phase element made of fused silica and etched with its phase pattern of an LG_3^3 mode with a blazed grating. This is the highest average power extra cavity generation of a pure higher-order LG mode.

1.5 Solid-State Amplifiers

As we have seen in the previous section, the generation of structured light both inside and outside the laser cavity is a complex process that involves sensitive optical alignment and highly-specialized optical components. Optical cavities with structured light outputs are generally limited to a narrow window of output power before thermally-induced aberrations cause the cavity to become unstable and cease to lase. In the case of the extra-cavity beam shaping systems, the static elements, specifically the DOEs, are made from transparent fused silica which can sustain high average powers. However, they have very stringent input beam requirements to operate efficiently and are fabricated for only one beam shape. The dynamic systems, specifically the SLM, have arbitrary beam-shaping capabilities but are severely limited to low-power beam selection, especially for producing pure modes where complex-amplitude modulation is performed. To circumvent the low-power limitations of SLMs, while benefiting from their unrivalled beam shaping abilities, is to power scale the low-power output using an optical amplifier.

1.5.1 Basic Theory

Section 1.1.2 explains the concept of a laser resonator, which forms the basis of an optical amplifier. However, in an optical amplifier, the resonator cavity mirrors are omitted, leaving only the gain medium and an external energy source. For instance, consider a solid-state gain medium with a length of L and two energy levels $\Delta E = E_u - E_l$, each having an

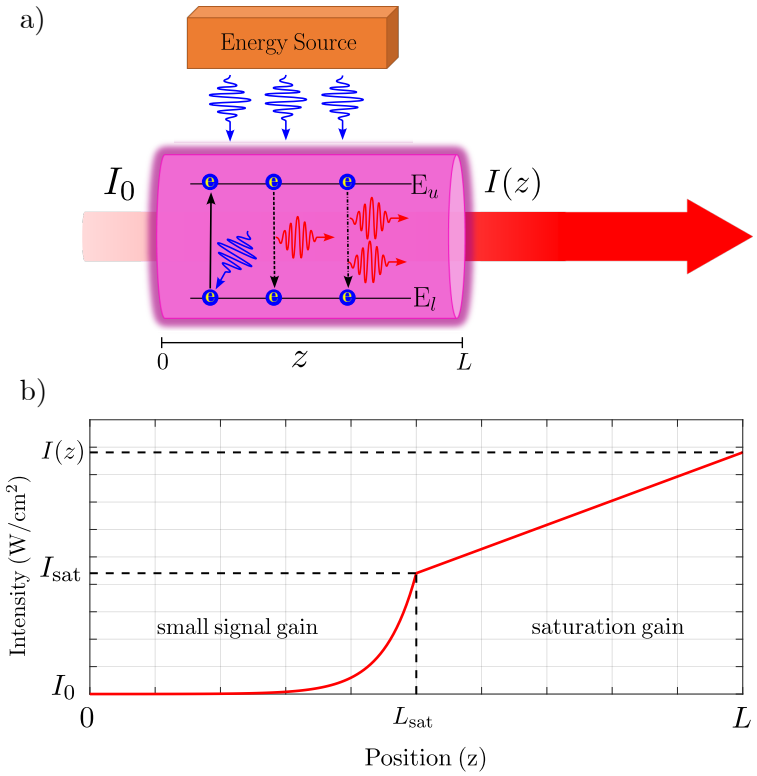


FIGURE 1.10: a) Schematic diagram showing an input beam with intensity I_0 passing through an externally pumped solid-state crystal (magenta) to emerge with an increased output intensity $I(z)$. While b) illustrates the two gain regions of an amplifier, above and below the saturation intensity I_{sat}, under steady-state pumping conditions. Where L_{sat} is the length of the crystal required to reach I_{sat}.

electron population density of N_u and N_l, respectively. By subjecting the gain medium to a steady supply of external optical energy, population inversion is achieved, with most electrons residing in the upper energy level ($N_u \gg N_l$). When an input optical field of intensity I_0 and wavelength $\lambda = hc/\Delta E$ enters the excited gain medium at $z = 0$ (as illustrated in Figure 1.10 a)), it induces stimulated emission, leading to the exponential growth of the optical field intensity $I(z)$ as a function of z within the gain medium:

$$I(z) = I_0\, e^{\sigma_{\text{em}}[N_u - N_l]z}. \tag{1.12}$$

The exponential growth of the optical field intensity $I(z)$, as given by equation 1.12, depends on the emission cross-section σ_{em} and the difference in electron densities $\Delta N = N_u - N_l$. As $I(z)$ increases, it eventually reaches the saturation intensity limit $I_{\text{sat}} = h\nu/\sigma_{\text{abs}}\tau_u$, where h, ν, and τ_u represent Planck's constant, the optical frequency, and the decay lifetime of the upper energy level E_u. At this point, the population inversion state is depleted, and the electron densities balance out ($N_u = N_l$). The rate of electrons being excited to N_u through absorption of the external energy source equals the rate of stimulated emission. Once $I(z)$ exceeds the saturation limit, the growth of the optical field is linear as a function of z:

$$I(z) = I_0 + g_0 I_{\text{sat}} z, \tag{1.13}$$

where g_0 is the small gain signal ($g_0 = \sigma\Delta N$). Figure 1.10 b) demonstrates the two operational regions of an amplifier, the small signal gain region when $I(z) < I_{\text{sat}}$ and the saturation gain region when $I(z) > I_{\text{sat}}$. Amplifiers are typically designed to operate above the I_{sat} region where efficient energy extraction occurs to minimise beam distortions caused by thermal effect due to excessive build-up of heat.

1.5.2 MOPAs

Master oscillator power amplification (MOPA) is a system to power scale beams from an oscillator through a power amplifier (PA). The technique of power scaling is modular in nature, meaning that multiple MOPAs can be stacked in series to obtain a high laser power [120]. When considering bulk-solid state crystals, an efficient way to excite or "pump" the gain medium is using narrow-wavelength diode-lasers in either side- or end-pumping geometries, as shown in Figure 1.11.

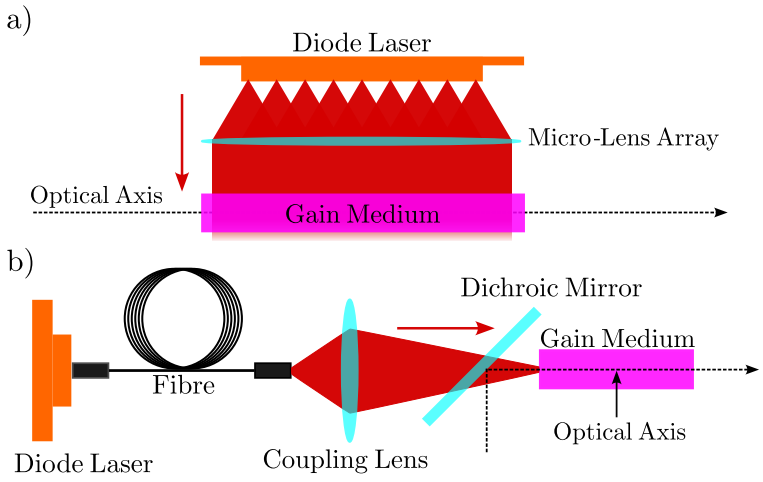


FIGURE 1.11: Schematic diagram depicting the a) side- and b) end-pumping MOPA configurations.

Side-pumped PAs can be generalized as systems where the pump photons enter the gain medium perpendicular with respect to the direction of the optical axis so that the crystal is homogenously excited. Side-pumped configurations offer high amplification potential but require a minimum threshold input seed power to amplify efficiently and are subjected to high-intensity pump radiation, which increases the risk of thermally-induced phase aberrations [121, 122]. In end-pumped systems, the pump photons are injected parallel to the optical axis, resulting in spatial confinement to a small region to achieve optimal spatial overlap with the optical field. End-pumped PAs are ideal for scaling power in the low to intermediate range (less than 100 W) and function effectively as pre-amplifier PA stages before being injected into side-pumped MOPAs to achieve high-power output [123]. The solid-state gain media used in MOPAs are manufactured into various geometries [124], such as; cylindrical rods [125] and single-crystal fibres (SCFs) [126], which support single or double-pass amplification, and the rectangular slabs [127], thin-disks [128] which can support multi-pass amplification for maximal energy extraction.

1.5.3 Amplification of Higher-Order Transverse modes

MOPA systems have been implemented to amplify the output of both intra-and extra-cavity generated higher-order transverse modes, specifically scalar and vector-polarized Laguerre-Gaussian modes. However, most of the attention has been directed towards the amplification of vortex beams. Here, we report a few of these examples from the literature that have achieved high-average power outputs using a MOPA.

End-pumped cylindrical rod MOPAs have been used to demonstrate power scaling of LG_0^1 vortex modes with scalar polarization [120], as well as radially [101] and azimuthally [69] polarized vector vortex modes, achieving average output powers of 40 W, 10.7 W, and 100 W, respectively. Amplification of vortex modes with 3 and 5-lobe petal intensity structures to 2.4 W and 1.8 W, respectively, demonstrated that complex spatial and phase structures can be preserved in end-pumped cylindrical rod MOPAs [129]. For side-pumped cylindrical rod MOPAs, examples range from low-power vector vortex outputs (< 1 W) with controllable polarization and high-purity [130, 131] to very high-power radially and azimuthally polarized vector vortex beams with 2.1 kW [132] and 4 kW [133] of average power outputs, using multiple MOPA systems stacked in series. Recently, an end-pumped rectangular slab MOPA was used to perform multi-pass amplification of a radially-polarized vector vortex beam to achieve an average output power of 33.7 W [134]. Power scaling of vortex beams using thin-disk multipass MOPAs has seen major improvements since it was first demonstrated, where it achieved an impressive average power of 635 W [135]. Since then, improvements were made to the MOPA design to increase the number of amplification passes from 20 to 30 [136] and then 44 passes, to achieve an impressive 1.7 kW average power output for a radially polarized vortex beam [137]. To our knowledge, there is only one instance in the literature where an arbitrary high-order scalar Laguerre-Gaussian mode generated with an SLM has been amplified using a single end-pumped Rubidium MOPA stage [138], but at low output powers < 30 mW. Therefore, based on the literature, the selection and amplification of higher-order modes using the MOPA strategy have yielded high-average powers sufficient for industrial applications. However, systems with dynamic selectivity, such as the SLM, are still far behind in terms of high-power generation.

1.6 Motivation

As we have seen in the previous sections, the complexity of laser beams, accelerated by advancements in beam-shaping technologies, has transcended from the simple fundamental Gaussian mode to exotic forms of structured light with complex spatial, phase and polarization properties. Potential growth for new and emerging application areas that may benefit from structured light is coupled firstly with our ability to select them at will, and most importantly, to obtain them at the average power levels that the application necessitates. In fact, there are currently no commercially available laser systems that deliver on-demand pure higher-order transverse modes. Nevertheless, there is extensive research to show that many if not all laser-enables processes can benefit greatly from the ability to tailor light using an ad hoc approach for each task at hand, where the spatial, phase and polarization degrees of freedom should be added to the toolbox [30, 139, 140]. The digital spatial-light modulator (SLM) is a highly versatile and flexible beam-shaping technology that has been shown to produce structured light with high purity and efficiency, surpassing that of its digital micromirror device counterpart. SLMs are presently constrained by their thermal limitations, which render

them inadequate for direct beam shaping in high-power experiments and applications. As a result, they are predominantly employed for low-power fundamental research.

In this dissertation, SLM beam-shaping technology is utilized for the on-demand selection of high-order Laguerre-Gaussian beams used in conjunction with power-scaling systems to provide a route towards the realization of a system capable of delivering high-power structured light with no moving parts, reconfiguration or adjustments of any kind. As evident in the literature, there is limited research regarding amplifying higher-order Laguerre-Gaussian modes or higher-order modes in general. Presented in the format as separate research articles, the upcoming chapters 2 to 4 cover various important topics which will be briefly summarized here. In chapter 2, a three-dimensional model for an end-pumped rod MOPA system is provided, utilizing a step-wise beam propagation method and contemporary analytical expressions for the gain saturation, thermal-gradient and thermal effects. We expand on current modelling approaches, which treat the pump beam as a static shape, by using a Gaussian to flat-top transformation allowing the step-wise model to include pump beam propagation dynamics. Furthermore, using experimental spectral data, a calibration procedure is demonstrated to establish the correct physical inputs of the model. In chapter 3, a novel dual-pass end-pumped rod MOPA design is demonstrated and compared to conventional approaches. The novel MOPA design is used to perform power scaling of the first nine LG_p^l modes, having identical beam sizes and input powers, generated via complex amplitude shaping using an SLM. The developed three-dimensional model was used to analyse the single and double pass amplification of each LG_p^l mode in terms of beam quality, and correlation between the output power and spatial overlap with the pump beam. In chapter 4, amplification of higher-order LG_0^2 modes is performed and the thermally-induced aberrations manifesting in the end-pumped crystal rod are investigated using a Shack-Hartmann wavefront sensor and analysed using the Zernike polynomials. The phase aberration induced the phenomena of "vortex splitting" beam distortion. A computational modal decomposition was performed on the aberrated LG_0^2 beams for various input beam sizes. Interestingly, a case is presented demonstrating the amalgamation of the distortion in the far field through a carefully induced Gouy phase shift. The dissertation is concluded in chapter 5 with brief summary of each chapter followed by a discussion on future work.

Chapter 2

3D modelling of End-Pumped MOPAs

2.1 Introduction

Bulk solid-state Master Oscillator Power Amplifier (MOPA) systems have, for several decades, been of considerable interest in industry to power scale low-power laser beams from a master oscillator to higher powers [141]. In such a MOPA configuration, the amplifier laser gain medium is excited using a pump source that is typically a narrow-wavelength diode-laser (single or multi-mode) in either a side- or end-pumping configuration. In a side-pumped configuration, pump light from stacked diode-laser bars is directed perpendicular to the optical axis while the seed beam (output from the oscillator), which is to be amplified, is propagated along the optical axis [142, 143]. Conversely, in end-pumped systems, the input pump source, which is typically a multi-mode fibre-coupled (MMFC) diode-laser, impinges a laser gain medium along the optical axis where the seed beam is co-axially propagated with the pump beam for optimal spatial overlap. While the design complexity of master oscillators prove to be considerably lower than MOPA systems in achieving high output powers, they possess high optical intra-cavity intensities which may lead to a degradation in the output beam parameters such as purity, power and polarization, especially if specialized intra-cavity optical components such as wavelength tuning devices and electro-optical q-switches are required. MOPA systems that contain a low-power oscillator and several sequential amplifiers enable the decoupling of sensitive intra-cavity optical components in the oscillator to achieve the desired output beam performance characteristics [120]. Such systems offer flexibility in pulse duration control, wavelength tuning, output power control, and maintaining the beam quality of the output from the oscillator. In addition, gradual power scaling reduces the thermal load on the laser gain medium thereby reducing thermal distortions and preserving the spatial, temporal and spectral properties of the amplified beam [144]. Such control is pertinent in applications such as marking and laser shock peening [145].

The two MOPA design configurations above both have advantages and disadvantages. Side-pumped systems offer higher amplification potential, however, since the entire gain medium is pumped, the thermal load in the gain medium increases dramatically thereby potentially distorting the seed beam due to thermally-induced phase aberrations [146–148]. End-pumped systems offer full control of the thermally induced aberrations to maintain the seed beam quality, however, at the cost of a lower amplification potential leading to a considerable

decrease in the output power of the amplified seed beam. In applications that employ high-brightness laser beams, which require both the output laser beam power and its beam quality to be maximised, both design configurations may be implemented, however, a prominent advantage of end-pumped systems is that it may be applied to a variety of laser gain media geometries such as thin-disks [128], cylindrical rods [149], fibre [150], and slab architectures [151]. To ensure that both the output power and beam quality are maximised, a stringent modelling approach is required to optimise the design strategy. For this purpose, we consider cylindrical rod geometries as they prove to be cost-effective, controllable, robust and still widely used as pre-amplifier stages for the low to intermediate power scaling of low-power seed beams.

There have been several seminal papers that advanced the modelling of MOPA systems, particularly end-pumped systems. These include the simulation of Laguerre-Gaussian beam propagation in Raman, dye, and free-electron lasers [152], consideration of the transverse intensity distribution of the pump and seed beam during amplification [153], and derivation of an analytical expression for the temperature distribution of the pump beam [154]. The temperature distribution inside the gain medium induces physical thermal expansion and thermo-optical changes, which influence the propagation of the seed beam through the gain medium. Over the last two decades, end-pumped isotropic materials, specifically YAG, have been modelled using only analytical expressions for the steady state rate-equations [155], temperature distributions of various pump beam profiles [156] and stress-strain effects leading to seed beam distortions [157] using the beam propagation method [158, 159]. More complex numerical models using finite element methods have also been investigated [160–162].

End-pumped systems typically employ a fiber-coupled diode laser as the pump source that is focused to the crystal face or at some position along the length of the crystal. For multi-mode sources (with core diameters >200 μm), the output rapidly evolves from a top-hat-shaped beam at the exit face of the fiber to a Gaussian or bell-like transverse profile along the propagation axis. As the pump beam is a fundamental component in end-pumped systems as it dictates the overall performance of the amplifier and the gain achievable in the system, it is necessary that not only the pump spatial profile at its highest fluence be characterized but so too its dynamic propagation behaviour over the gain medium volume. Current 2D or 3D end-pumped models consider a pump beam output that is static in its spatial intensity profile and is approximated as being either a uniform beam or top-hat [148, 159, 163, 164], Gaussian beam [154, 160, 165, 166], super-Gaussian beam [158, 167–170] or an arbitrary polynomial distribution [171]. With this, the static pump beam at the crystal face either holds its transverse distribution in propagation over the crystal length (3D models) or is reduced to two dimensions (2D models).

A second key characteristic of the pump source is its spectral behaviour. This describes the amplification potential of the amplifier as the gain saturation is based on the output wavelength of the pump source. The output wavelength of the pump laser is known to vary based on the driving current applied to the diodes in the pump laser due to changes in the temperature of the diodes. The vast majority of existing amplifier models consider a single value for the pump absorption cross-section which is typically related to the maximum absorption wavelength of the gain material. This critical factor is not static across the current levels and if incorrectly selected, will lead to significant errors in the determination of the temperature distribution, amplification potential and overall accuracy of the performance of

the amplifier.

In this chapter, we provide a new approach to modelling end-pumped Nd:YAG rod amplifiers in three dimensions with a multi-mode fibre-coupled diode laser as the pump. Here we describe the pump beam as a complex field that mimics the spatial evolution of a multi-mode fibre-coupled diode laser using a lossless phase-only Gaussian to Flat-top (FT) beam shaping technique. Additionally, we describe an approach, with calibration steps, to accurately determine the pump absorption cross-section for arbitrary driving currents. In our model, the gain medium is treated as a 3D mesh ($N_{x,y,z}$) so that the pump transformation occurs as it propagates longitudinally inside the crystal using a beam propagation method (BPM). This approach enables the gain saturation, thermal gradient and change in refractive index to be calculated at each N_z-interval using only analytical expressions in an iterative procedure. To demonstrate the accuracy of the model, we simulate the amplification of a Gaussian beam and verify the results experimentally.

2.2 Theory

An attractive approach to modelling end-pumped amplifiers in three dimensions is to make use of a beam propagation method (BPM) [158]. Such an approach harnesses Fast Fourier Transforms (FFTs) that are used to simulate accurate propagation of the pump and seed beams along the gain medium which includes diffraction effects provided that the pump and seed are complex fields that are solutions to Maxwell's wave equation. For seed beams that are eigenmodes, the electric fields are well-defined solutions to Maxwell's equations, however, this is not the case for MMFC diode-laser pump beams. Borrowing from the concepts of lossless beam-shaping, the MMFC pump beam may be described as a metamorphosis of a Gaussian mode to a FT beam using a phase-only diffractive element. The creation of the Gaussian to FT phase-element is highly flexible and allows for full control over the desired beam sizes, divergences and associated propagation distance between the two [172].

The energy-transfer between pump photons and the active ions or dopants in the laser crystal determines the gain distribution, which results in amplification, and the temperature gradient which leads to thermal-expansion (stress-strain) and optical (change in refractive index) variations in the crystal medium. Spatially, the gain and thermal distributions are proportional to the spatial profile and intensity of the pump beam which necessitates the accurate description of the pump beam evolution over the crystal length. An equally important factor is the rate of energy-transfer from the pump photons to the crystal material, which is defined as the absorption-cross section that dictates the magnitude of the gain and temperature distributions. Therefore, a comprehensive model must consider the spatial evolution and rate of energy-transfer of the pump beam collectively.

In this section, we discuss the theory for a cubic Nd:YAG ([1 1 1] cut) laser medium. Here, the amplifier characteristics, especially the thermal effects, may be understood through the treatment of analytical equations which provides a holistic and quantitative insight into the working parameters of the amplifier. In the subsections to follow, we will discuss the Gaussian to FT pump beam shaping process, the treatment of the pump beam absorption cross-section, and provide analytical expressions for the temperature distribution and the resulting change in refractive index. This section will be concluded by outlining the BPM to which all analytical expressions will be combined.

2.2.1 Pump Beam Modelling

The output of multi-mode fibre-coupled (MMFC) diode pump lasers do not possess a well-defined phase structure which results in an output that is incoherent and highly divergent. As such, simulation of its free-space propagation or propagation in complex media is a non-trivial task. The spatial profile of the output of a MMFC pump beam is flat-top (FT) shaped at the face of the fiber and rapidly diverges and transforms to a Gaussian-like intensity profile along the propagation axis, as illustrated in Figure 2.1. It is well known that such a pump beam may be focused to a Gaussian-like profile, however, beyond the focus, the spatial intensity profile rapidly evolves to a beam with a central dip with a triangular-shaped profile in between. To achieve a more stable behaviour, the exit face of the fiber may be imaged to the desired size using an afocal telescope. Here the beam will evolve from a FT-shaped beam to a Gaussian-like profile in a smooth and predictable manner. Through the stationary phase approximation, this behaviour can be modelled by utilising a lossless phase-only beam shaping technique which transforms a Gaussian beam to a FT beam, at the Fourier plane of a lens [52, 172, 173]. This approach enables the MMFC pump beam to be modelled as a complex field that mimics the divergence and spatial intensity transformation in free-space propagation.

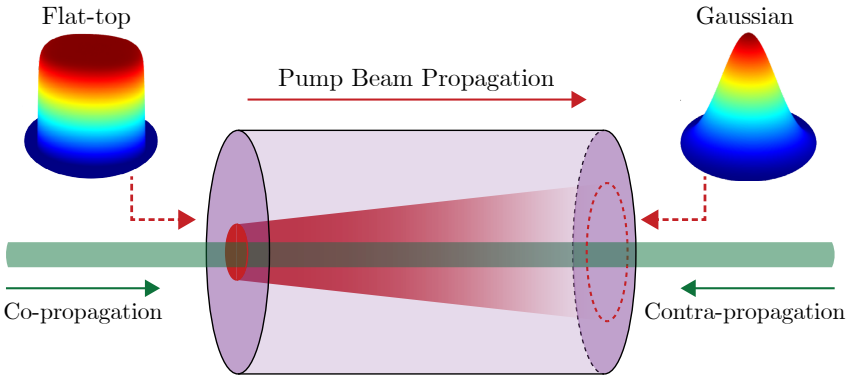


FIGURE 2.1: Illustration of the spatial evolution of a typical MMFC pump beam (red) propagating through a crystal material (magenta cylinder), with co- and contra-propagating seed beams (green arrows).

The phase-only transmission function $\Phi_{\mathrm{FT}}(r)$ and Fourier lens function $\mathrm{T}_{\mathrm{lens}}(r)$ to perform a Gaussian to FT beam transformation is expressed as:

$$\Phi_{\mathrm{FT}}(r) = \frac{\pi\omega_i\omega_f}{\sqrt{2}f\lambda}\int_0^{\rho}\sqrt{1-\exp\left(-\rho^2\right)}d\rho\,, \quad \text{with} \quad \rho = \frac{\sqrt{2}r}{\omega_i} \text{ and,} \tag{2.1}$$

$$\mathrm{T}_{\mathrm{lens}}(r) = \exp\left[\frac{-ikr^2}{2f}\right]. \tag{2.2}$$

where λ is the wavelength, k is the wavenumber, r is the radial coordinate, ω_i is the initial Gaussian beam radius, ω_f is the radius of the desired FT beam and f is the focal length of the Fourier lens $\mathrm{T}_{\mathrm{lens}}$, defined by equation 2.2.

For inline end-pumped amplifiers, the seed beam can be made to either co- or contra-propagate

with respect to the propagation direction of the pump beam. In the co-propagating configuration the seed and pump beams enter the crystal at the same end and propagate in the same direction, whereas for the contra-propagating configuration, the seed beam and pump beam propagate in opposite directions and enter the crystal at adjacent ends, as shown in Figure 2.1.

In the following section, we outline the mathematical steps for simulating the Gaussian to FT pump shaping transformations in both co- and contra-propagation configurations.

Contra-Propagation

The contra-propagation configuration consists of a convergent seed beam that is directed at a crystal on the opposite end of the highest pump fluence. At this end, the pump beam has a large Gaussian-like profile and as the seed decreases in size as it traverses the length of the crystal, it will arrive to its desired width on the opposite end of the crystal where the pump beam is a tightly focused FT profile. To simulate this case, we create the phase transformation $\Phi_{\mathrm{FT}}(r)$, by specifying the desired FT beam radius ω_f, Gaussian beam radius ω_i, and the Fourier lens focal length f to produce the transmittance of a single phase-element DOE_1

$$\mathrm{DOE}_1 = \mathrm{T}_{\mathrm{lens}}(r) \times \exp\left[-i\Phi_{\mathrm{FT}}(r)\right] . \tag{2.3}$$

For a Gaussian beam of radius w_i and power P_{p}, the corresponding beam will be modulated with the phase-transformation of DOE[1]

$$\Psi_{\mathrm{G}}(r) = \sqrt{\frac{2P_{\mathrm{p}}}{\pi\omega_i^2}}\exp\left[\frac{-r^2}{\omega_i^2}\right] \times \mathrm{DOE}_1 , \tag{2.4}$$

The modulated Gaussian beam $\Psi_{\mathrm{G}}(r)$ will transform gradually to a FT beam Ψ_{FT} of radius w_f during free-space propagation over the distance of the Fourier lens f, as depicted by Figure 2.2. It is important to note that when simulating the contra-propagating case, the pump beam propagation direction must be flipped so that it appears to travel backwards over the length of the crystal. Therefore, P_{p} of the Gaussian beam $\Psi_{\mathrm{G}}(r)$ is equal to the absorbed pump power measured after propagating through the crystal and not the total power that was injected into the crystal. Therefore, the sign of the absorption coefficient in the simulation must also change from an exponentially decreasing to an exponentially increasing function as will be discussed later.

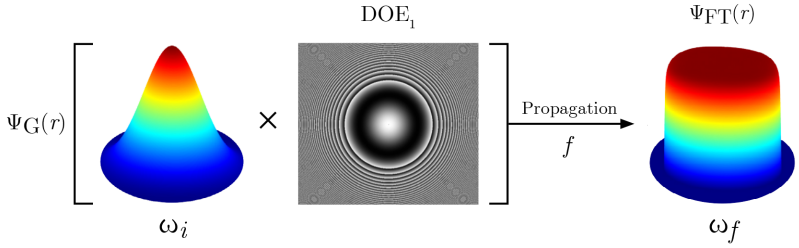


FIGURE 2.2: Initial Gaussian beam modulated by the phase of DOE_1 that transforms into a FT beam $\Psi_{\mathrm{FT}}(r)$ at the Fourier plane of lens f, used for a contra-propagation simulation.

Co-Propagation

In the co-propagating configuration, the seed and pump beams propagate in the same direction. The divergent seed beam, at its desired beam width, is injected at the crystal end where the pump beam is a tightly focused FT profile and exits the crystal where the pump beam has a large Gaussian-like shape. To simulate this configuration, the pump shaping process must be reversed from a Gaussian-FT to a FT-Gaussian transformation. To achieve this, the complex-conjugate phase of the FT beam $\Psi_{\mathrm{FT}}(r)$ at the plane of the Fourier lens f, shown on the right of Figure 2.2, is extracted and labelled as $\varphi_{\mathrm{FT}}(r)$. This is then used to create the reverse phase-modulation transformation, which is defined as DOE_2.

$$\mathrm{DOE}_2 = \exp\left[i\varphi_{\mathrm{FT}}(r)\right] . \tag{2.5}$$

The phase profile DOE_2 is then applied to the FT beam $\Psi_{\mathrm{FT}}(r)$ twice, once to cancel out the existing phase and a second time to modulate the beam with the reverse phase transformation

$$\Psi_{\mathrm{FT}^*}(r) = \Psi_{\mathrm{FT}}(r) \times \mathrm{DOE}_2 \times \mathrm{DOE}_2 . \tag{2.6}$$

Now, $\Psi_{\mathrm{FT}^*}(r)$ will transform from a FT beam back to the initial Gaussian beam $T_{\mathrm{G}}(r)$ during propagation over the length of the Fourier lens f, as depicted in Figure 2.3.

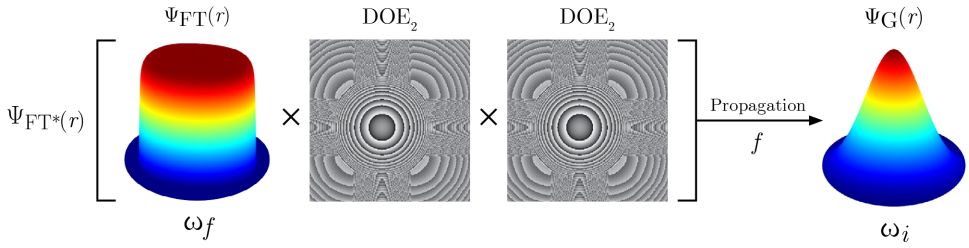


FIGURE 2.3: FT beam $\Psi_{\mathrm{FT}}(r)$ modulated by the phase transformation of DOE_2 that reverses the transformation process back to the original Gaussian beam $\Psi_{\mathrm{G}}(r)$ at the Fourier plane of lens f, used for a co-propagation simulation.

In the co-propagating scenario, since the beams enter the crystal at the same end, the pump power P_{p} of equation 2.4 should be the total input pump beam power before it enters the crystal and the sign of the absorption coefficient should be exponentially decaying. This simulation process is required to be calibrated by physical measurements of the parameters ω_i, ω_f and P_{p} to obtain the most accurate pump behaviour.

2.2.2 Absorption Cross-Section

The rate at which pump photons are absorbed by the neodymium (Nd^{3+}) ions inside the yttrium aluminium garnet (YAG) host lattice is determined by the absorption cross-section σ_{abs} (i.e. the probability of an absorption event to take place). The σ_{abs} spectrum for 0.5% atm. doped Nd:YAG is depicted by the solid black curve in Figure 2.4. The original data for σ_{abs} spectra in the Figure was measured for a 1% atm. doped Nd:YAG sample and had a peak value of $10 \times 10^{-20}\mathrm{cm}^2$ at wavelength 808 nm [174]. At low doping concentrations, σ_{abs} varies linearly with the dopant % and therefore, the original data can be scaled to represent a 0.5% doped Nd:YAG crystal [175]. The spectral line shape of a typical MMFC diode laser emission can be approximated as a standard Lorentzian distribution function, indicated by

the red curve in Figure 2.4, having a well-defined central wavelength λ_0 (vertical red dotted line) and bandwidth $\Delta\lambda$.

Experimentally, the central wavelength λ_0 and spectra bandwidth $\Delta\lambda$ of the MMFC emission spectrum varies with the driving current due to a temperature change in the diodes. This is the typical behaviour of diode lasers and manufacturers generally provide a value for the expected nm/C° or nm/A central wavelength shift as a function of temperature or current. The spectral emission characteristics of most 808 nm wavelength MMFC diodes vary between central wavelengths of 802 nm at threshold current to 808 nm at the maximum driving current with a spectral bandwidth of < 2 nm. Nevertheless, most amplification models use the peak absorption cross-section $\sigma_{\text{abs}}^{\text{p}^*} = 5 \times 10^{-20}$ cm^2 (vertical magenta line in Figure 2.4) across all driving currents and do not consider the spectral overlap of the emission and absorption curves. This is a significant oversight that leads to an overestimation of the pump absorption and seed amplification behaviour. Ideally, λ_0 and $\Delta\lambda$ of the diode emission spectrum should be measured experimentally, as a function of the pump power (i.e. driving current). With this information, an accurate $\sigma_{\text{abs}}^{\text{p}}$ value can be calculated by performing an overlap integral between a Lorentzian function $f(\lambda)$, using the experimentally determined λ_0 and $\Delta\lambda$ values, and the absorption cross-section data $g(\lambda)$ of the Nd:YAG crystal

$$\sigma_{\text{abs}}^{\text{p}} = \frac{\int g(\lambda) f(\lambda)\, \mathrm{d}\lambda}{\int g(\lambda) g(\lambda)\, \mathrm{d}\lambda} \tag{2.7}$$

The Lorentzian function $f(\lambda)$ is normalised to the peak absorption value. As an example, the overlap between the two curves, depicted as the magenta shaded region in Figure 2.4, is the weighted value of $\sigma_{\text{abs}}^{\text{p}} = 9.1 \times 10^{-21}$ cm^2 which is 5.5× smaller than the peak value of $\sigma_{\text{abs}}^{\text{p}*}$.

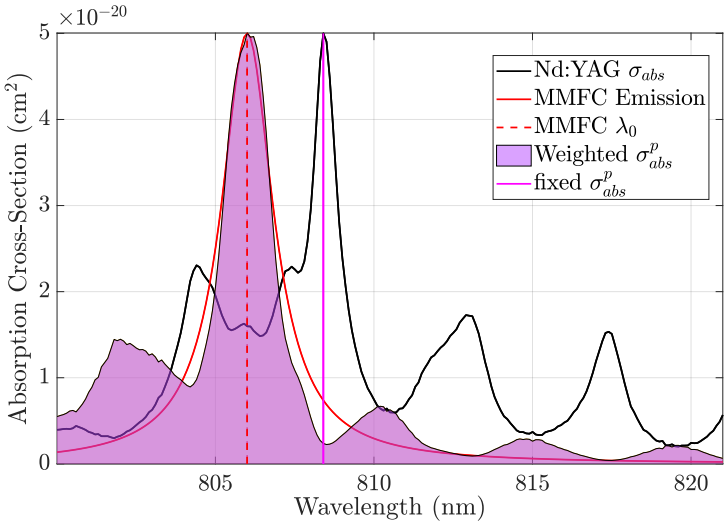


FIGURE 2.4: Absorption cross-section of Nd:YAG crystal (black) and emission spectrum of the pump diode (red) with resulting weighted overlap integral (blue shaded area).

2.2.3 Gain and Absorption coefficients

In a lossless 4-level Nd:YAG gain medium under steady-state continuous pumping conditions, the gain coefficient $G(r, z)$ that describes the exponential growth rate of a seed beam can be

written in cylindrical coordinates as [155, 170]

$$G(r,z) = \frac{I_{\mathrm{p}}(r,z) N_{\mathrm{tot}} \tau_{\mathrm{em}} \sigma^{\mathrm{p}}_{\mathrm{abs}} \sigma^{\mathrm{s}}_{\mathrm{em}}}{1 + \frac{I_{\mathrm{p}}(r,z)}{I^{\mathrm{p}}_{\mathrm{sat}}} + \frac{I_{\mathrm{s}}(r,z)}{I^{\mathrm{s}}_{\mathrm{sat}}}}\,, \tag{2.8}$$

where $\sigma^{\mathrm{p}}_{\mathrm{abs}}$ and $\sigma^{\mathrm{s}}_{\mathrm{em}}$ are the absorption and emission cross-sections of the pump $I_{\mathrm{p}}(r,z)$ and seed $I_{\mathrm{s}}(r,z)$ beams, respectively, while N_{tot} and τ_{em} are the number of active Nd^{3+} ions and decay-lifetime of the upper laser level, respectively. The saturation intensities of the seed $I^{\mathrm{s}}_{\mathrm{sat}}$ and pump $I^{\mathrm{p}}_{\mathrm{sat}}$ beams are calculated as

$$I^{\mathrm{s}}_{\mathrm{sat}} = h\nu_{\mathrm{s}}/\tau_{\mathrm{em}}\sigma^{\mathrm{s}}_{\mathrm{em}} \quad \text{and} \quad I^{\mathrm{p}}_{\mathrm{sat}} = h\nu_{\mathrm{p}}/\tau_{\mathrm{em}}\sigma^{\mathrm{p}}_{\mathrm{abs}}, \tag{2.9}$$

where h, ν_{s} and ν_{p} are Planck's constant and the frequency of the seed and pump beams, respectively.

Analogous to the gain coefficient, which defines the increase of the seed intensity I_{s}, the absorption coefficient $\alpha(r,z)$ describes the rate of the longitudinal exponential absorption of the pump intensity I_{p} by the crystal. Similarly, for a lossless 4-level Nd:YAG gain medium under steady-state continuous pumping conditions, the absorption coefficient may be written as

$$\alpha(r,z) = \frac{[I_{\mathrm{s}}(r,z)\tau_{\mathrm{em}}\sigma^{\mathrm{s}}_{\mathrm{em}} + 1] \times N_{\mathrm{tot}}\sigma^{p}_{\mathrm{abs}}}{1 + \frac{I_{\mathrm{p}}(r,z)}{I^{\mathrm{p}}_{\mathrm{sat}}} + \frac{I_{\mathrm{s}}(r,z)}{I^{\mathrm{s}}_{\mathrm{sat}}}}\,. \tag{2.10}$$

When the input seed intensity is below the saturation intensity ($I_{\mathrm{s}} << I^{\mathrm{s}}_{\mathrm{sat}}$), the gain distribution is proportional to the small signal gain $g_0 = I_{\mathrm{p}} N_{\mathrm{tot}} \sigma^{\mathrm{p}}_{\mathrm{abs}}$ and the seed beam experiences exponential amplification (i.e. $I_{\mathrm{s}} \propto I^0_{\mathrm{s}} e^{g_0 z}$), where I^0_{s} is the input seed intensity. When the seed intensity exceeds the saturation intensity ($I_{\mathrm{s}} >> I^{\mathrm{s}}_{\mathrm{sat}}$), the growth factor is reduced to a linear increase in the intensity of the beam. The saturation effects of the gain and absorption, are accounted for in the denominator of equations 2.8 & 2.10 and govern the growth rate of I_{s} and similarly the decay of I_{p}.

2.2.4 Temperature-Gradient

The difference in energy between the pump absorption and laser emission energy levels contributes to the heat generated inside the gain medium. This is caused by an effect known as quantum defect heating η_{h}, as only a fraction of pump photons that are absorbed reach the laser emission band and the rest are converted to heat through non-radiative relaxation processes ($\eta_{\mathrm{h}} = 0.24$ for 0.5% Nd:YAG). The analytical expressions of gain $G(r,z)$ and absorption $\alpha(r,z)$ coefficients, in steady-state, are calculable at any point during the Gaussian-FT transformation since they require only the intensity profile of the pump and seed beams. However, an analytical expression for the temperature distribution induced by the Gaussian to FT pump inside the gain medium is non-trivial.

In recent work by I. Cini et. al. (2017) [156], an analytical solution was obtained for the temperature $T(r,z)$ produced when end-pumping a cubic crystal (such as Nd:YAG) with a generalized $\mathrm{n_{th}}$ order super-Gaussian pump beam $\mathrm{SG^n}(r,z)$.

The boundary conditions in the derivation accounted for active cooling by a surrounding heat sink, schematically depicted in Figure 2.5, and solved using the steady-state heat conductance

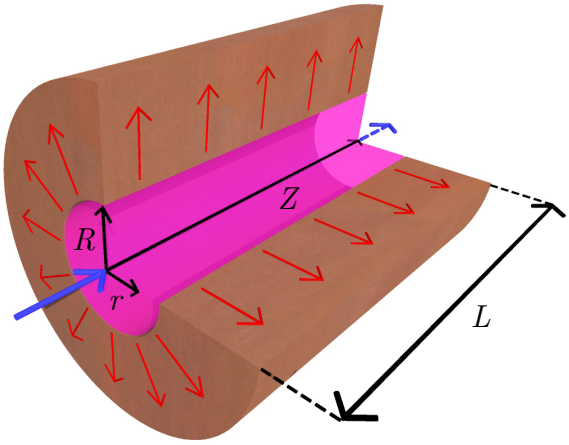


FIGURE 2.5: Schematic diagram of an end-pumped (blue arrows) laser rod (magenta) of radius R and length L mounted inside a copper heatsink (brown) with red arrows indicating the radial direction of heat flow.

equation in cylindrical coordinates with temperature-dependant thermal conductivity $k(T)$

$$k(T) = k_0 \left(\frac{T}{T_0}\right)^{\xi}, \tag{2.11}$$

where k_0 & T_0 are the thermal conductivity and reference temperature, respectively, and ξ is determined by a best fit to experimental data for the appropriate crystal dopant percentage and temperature range. A comprehensive list of these values for different crystals and temperatures can be found in reference [156]. For end-pumped crystal rods where the crystal radius is smaller than its length ($R << L$) and the pump beam is axially symmetric with isotropic cooling in the z-axis, then we can assume that the heat flow will be purely radial (red arrows in Figure 2.5) and the heat conductance differential equation simplifies to

$$\frac{1}{r}\frac{\mathrm{d}}{\mathrm{d}r}\left[rk(T)\frac{\mathrm{d}T(r,z)}{\mathrm{d}r}\right] + \mathrm{SG}^{\mathrm{n}}(r,z) = 0\,. \tag{2.12}$$

Equation 2.12 can then be solved to obtain the analytical expression for the temperature distribution $T(r,z)$ induced by the generalized super-Gaussian pump beam $\mathrm{SG}^{\mathrm{n}}(r,z)$ of order n, using the temperature dependant thermal conductivity $k(T)$ of equation 2.11. Rather than use the absolute temperature $T(r,z)$, it is convenient to define the temperature gradient relative to the boundary interface of the crystal rod and heat-sink material $T(R,z)$

$$\begin{aligned}\Delta T(r,z) = T(r,z) - T(R,z)\Bigg\{ & G_0\, e^{-\alpha(r,z)z} \times \Bigg[R^2{}_2F_2\left(\frac{2}{\mathrm{n}},\frac{2}{\mathrm{n}};1+\frac{2}{\mathrm{n}},1+\frac{2}{\mathrm{n}};-\frac{2R^{\mathrm{n}}}{\omega_{\mathrm{p}}^{\mathrm{n}}}\right) \\ & - r^2{}_2F_2\left(\frac{2}{\mathrm{n}},\frac{2}{\mathrm{n}};1+\frac{2}{\mathrm{n}},1+\frac{2}{\mathrm{n}};-\frac{2r^{\mathrm{n}}}{\omega_{\mathrm{p}}^{\mathrm{n}}}\right)\Bigg] + \left(T_{\mathrm{sink}} + \frac{\eta_{\mathrm{h}}P_{\mathrm{p}}\alpha(r,z)e^{-\alpha(r,z)z}}{2\pi R h_{\mathrm{c}}}\right)^{\xi+1}\Bigg\}^{\frac{1}{\xi+1}} \\ & - \left(T_{\mathrm{sink}} + \frac{\eta_{\mathrm{h}}P_{\mathrm{p}}\alpha(r,z)e^{-\alpha(r,z)z}}{2\pi R h_{\mathrm{c}}}\right),\end{aligned} \tag{2.13}$$

where

$$F_0 = \frac{\eta_{\mathrm{h}} P_{\mathrm{p}} \alpha(r,z)(\xi+1)T_0^{\xi}}{4\pi k_0} \quad \& \quad G_0 = \frac{2^{\left(\frac{2}{\mathrm{n}}-1\right)}\mathrm{n}F_0}{\Gamma(\frac{2}{\mathrm{n}})\omega_{\mathrm{p}}^2}.$$

${}_pF_q(a_1,\cdots,a_p;b_1,\cdots,b_q;z)$ and Γ are a Generalized Hypergeometric and Gamma Functions, respectively. R, ω_{p}, r, z, P_{p} and $\alpha(r,z)$ are the crystal radius, pump beam radius, the radial coordinate, longitudinal position, pump power and absorption coefficient, respectively. The variables T_{sink} and h_{c} are the heat-sink coolant temperature and heat transfer coefficient between the crystal rod and copper cooling block interface. The resulting thermal gradient $\Delta T(r,z)$ produces the well-know quadratic radial dependence of the temperature profile inside the pumped region of the crystal and logarithmic outside, so that $\Delta T(r,z) \to 0$ as $r \to R$ at the crystal boundary interface.

Analytically solving equation 2.12 at each N_z interval to obtain a unique $\Delta T(r,z)$ for the Gaussian to the FT pump transformation is not possible. Therefore, we use the generalised solution of equation 2.13 as is, and select a $\mathrm{SG}^{\mathrm{n}}(r,z)$ approximation that best fits the spatial profile and radius of Gaussian to FT transformation at each N_z position. This approximation is acceptable since the parabolic shape of $\Delta T(r,z)$ is quite similar for super-Gaussian beams of order $n = 2, 4, 6$ & 8, what is more important is the change in the pump beam size due to divergence which is accounted for at each N_z interval.

2.2.5 Change in refractive-index

The thermal gradient $\Delta T(r,z)$ that develops inside the gain medium causes the material to experience stress-strain effects leading to mechanical bulging of the crystal end-faces defined by the thermal expansion coefficient C. Additionally, thermo-optical changes occur in the material which cause variations to the refractive index n defined by the coefficient β(i.e. $\frac{\mathrm{d}n}{\mathrm{d}T}$).

In most amplifier models, the change in refractive index is simply defined as $\Delta n(r) = \frac{\mathrm{d}n}{\mathrm{d}T}\Delta T(r)$, where $\frac{\mathrm{d}n}{\mathrm{d}T}$ is the thermal dispersion coefficient with values ranging between $7\text{–}10\times10^{-6}$ K^{-1} for Nd:YAG at room temperature ~ 300 K [176, 177]. The change in refractive index produced by the quadratic to logarithmic variation in the thermal gradient $\Delta T(r,z)$ of equation 2.13, will simulate both thermal lensing and spherical aberration effects [170]. This simple method for calculating $\Delta n(r)$ is a reasonable approximation, depending on how well $\Delta T(r)$ is defined but neglects thermal expansion caused by stress and strain of the material.

A holistic $\Delta n(r)$ calculation for end-pumped amplifiers, especially when high-pump powers are involved, must include the effects of stress and strain and use temperature dependant coefficients so that $\mathrm{C} \equiv \mathrm{C}(T)$ and $\beta \equiv \beta(T)$. Extensive research has been conducted on the topic of thermally-induced stress-strain effects in cubic crystals, particularly Nd:YAG. Detailed explanations on the use of temperature-dependent coefficients $\mathrm{C}(T)$ and $\beta(T)$ have been provided in several publications [157, 176, 178]. The mechanical properties of cubic crystals, such as [1 1 1] cut Nd:YAG, can be estimated as an isotropic solid media where only two elastic coefficients (Poisson's ratio ν and Young's modulus E) are needed for a description of induced stress-strain and resulting change in refractive index $\Delta n(r)$

$$\Delta n(r) = n(r) - n_o = -a_1 \mathrm{C}_{\sum}^{R} + \beta_{\sum}(r) + a_1 \mathrm{C}_{\sum}(r) \quad \pm a_2 \left[\mathrm{C}_{\sum}^{r} - \mathrm{C}_{\sum}(r)\right], \tag{2.14}$$

with coefficients a_1 and a_2 defined as

$$a_1 = \frac{n_0^3\left[2(1-2\nu)(p_{11}+2p_{12})-(1+\nu)p_{44}\right]}{6(1-\nu)},$$
$$a_2 = \frac{n_0^3(1+\nu)(p_{11}-p_{12}+4p_{44})}{12(1-\nu)}.$$

The terms $\beta_{\sum}(r)$ and $\mathrm{C}_{\sum}(r)$ are the temperature-dependant thermo-optic and linear-expansion coefficients, respectively, which have been integrated with respect to temperature. The coefficients $\mathrm{C}_{\sum}^{R}$ & $\mathrm{C}_{\sum}^{r}$ are obtained from an additional integration over the crystal radius R and radial coordinate r, respectively. The above-mentioned integration steps to arrive at equation 2.14 are non-trivial, therefore, the reader is referred to the detailed discussion and derivation by D. Bričkus et. al. (2017) [157]. The coefficients a_1 and a_2 contain the Poisson's ratio ν, the initial reference refractive index n_0 and the p_{ij} coefficients of the elasto-optic matrix, which are provided in Table 2.1. The (+) and (-) signs infront of the last term in equation 2.14 describe the radial and tangential components of the change in refractive index. For low pumping fluence ($\mathrm{W/cm^2}$), the thermal dependencies of β and C can be neglected, however, for high-power pumped crystals the temperature-independent equations may underestimate the actual stresses by 1.5-1.8 times, which could result in crystal fracture if the thermal-fracture limit is exceeded (235 ± 16 MPa for YAG).

2.2.6 Beam Propagation Method

Using the scalar angle-spectrum theory of diffraction, based on the Fast Fourier Transform (FFT) method, the complex fields of the pump $\Psi_{\mathrm{p}}(r,z)$ and seed $\Psi_{\mathrm{s}}(r,z)$ beams are propagated using a split-step procedure, whereby the crystal volume of length L is divided into N_z intervals each of length $\delta z = L/N_z$.

Let $\Psi_i(r,z)$ be an arbitrary complex field that is an eigenmode of Maxwell's equation, the propagation of $\Psi_i(r,z)$ over a δz increment is as follows:

$$\Psi_i(r,z+\delta z) = F^{-1}\left\{F\left[\Psi_i(r,z)\right]\times\exp\left[ik\delta z\sqrt{1-\lambda^2(f_x^2-f_y^2)}\right]\right\}, \tag{2.15}$$

where $f_{x,y}$, F and F^{-1}, k and λ are the spatial frequencies in the Fourier domain, Fourier transform operator, inverse Fourier transform operator, wave number and wavelength, respectively.

Initialisation of Pump and Seed Fields

As discussed in section 2.1, the seed field $\Psi_{\mathrm{s}}(r,z)$ can be either co- or contra-propagating with respect to the pump field $\Psi_{\mathrm{p}}(r,z)$. For the sake of completeness, we describe the starting pump fields $\Psi_{\mathrm{p}}(r,z)$ for both cases, however, in our work, the experiment could only be performed in the contra-propagating configuration.

To simulate the co-propagating case, the starting pump field is set as the modified FT beam of equation 2.6

$$\Psi_{\mathrm{p}}(r,z) = \Psi_{\mathrm{FT}^*}(r), \tag{2.16}$$

and for the contra-propagating case, the starting pump beam is set to the Gaussian beam as defined by equation 2.4

$$\Psi_{\mathrm{p}}(r,z) = \Psi_{\mathrm{G}}(r). \tag{2.17}$$

Once $\Psi_{\mathrm{p}}(r,z)$ has been correctly defined, the spatial transformation of the pump (i.e Gaussian to FT or FT to Gaussian) will occur during the iterative propagation procedure.

In this work, the seed field $\Psi_{\mathrm{s}}(r,z)$ was a Gaussian beam of radius ω_{g} with an initial power P_{s} which is defined as

$$\Psi_{\mathrm{s}}(r,z) = \sqrt{\frac{2P_{\mathrm{s}}}{\pi\omega_{\mathrm{g}}^2}}\exp\left[\frac{-r^2}{\omega_{\mathrm{g}}^2}\right]. \tag{2.18}$$

While, $\Psi_{\mathrm{s}}(r,z)$ was chosen to be a Gaussian beam here, this modelling approach is in fact valid for any eigenmode from the Laguerre-Hermite-Gaussian mode family. Note that all variables with subscript (s) describe the seed beam, while all the subscript (p) is reserved for the pump beam.

Iterative procedure

The beam propagation method (BPM) of equation 2.15 is a tool that enables the seed and pump fields to interact in an iterative manner with the analytical expressions for the gain coefficient $G(r,z)$ of equation 2.8, absorption coefficient $\alpha(r,z)$ of equation 2.10, change in temperature gradient $\Delta T(r,z)$ of equation 2.13 and the change in refractive index $\Delta n(r)$ of equation 2.14, providing a complete solution for 3D modelling of Nd:YAG end-pumped amplifiers.

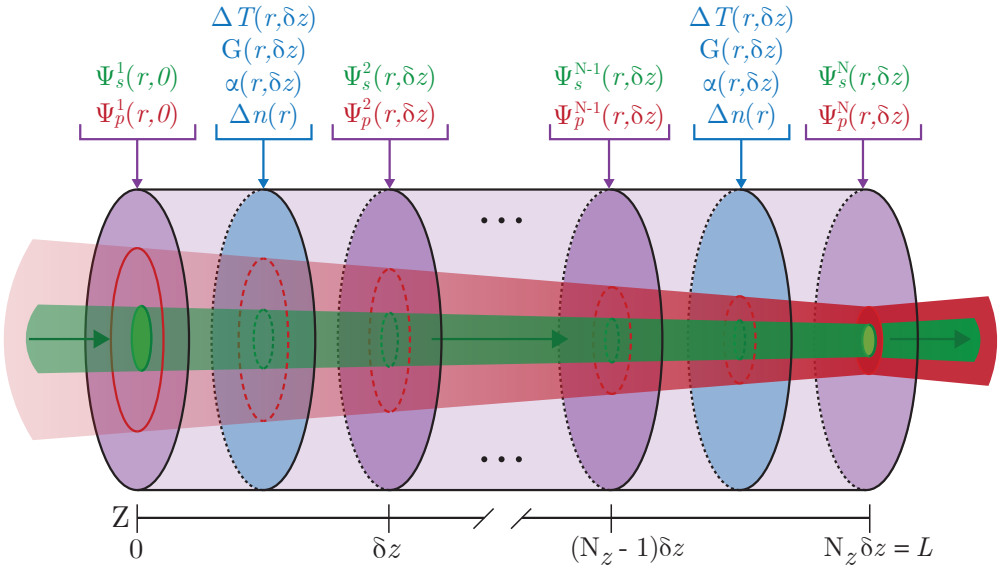


FIGURE 2.6: The schematic diagram illustrates the split-step iterative procedure for the pump beam (red) and seed beam (green) in a contra-propagating configuration, where the pump beam travels from right to left and the seed beam travels from left to right.

The BPM iterative procedure for the contra-propagation configuration can be explained with the aid of Figure 2.6. The simulation was performed in MATLAB using a mesh grid of dimensions $N_{x,y} = 3000$ and $N_z = 36$ so that each slice of the crystal was of width $\delta_z = 0.69$

mm. Increasing $N_z > 36$ did not improve on the model accuracy but only increased the computational time.

The position $z = 0$ marks the entrance face of the crystal, where the starting seed field $\Psi_s(r, 0)$ of equation 2.18 and pump field $\Psi_p(r, 0)$ of equation 2.17 are propagated midway into the first slice $N_{z=1}$ of the crystal (i.e. distance $\delta z/2$) using the propagation equation 2.15. At $z = \delta z/2$ (blue plane in Figure 2.6), the pump $I_p(r, \delta z/2) = |\Psi_p(r, \delta z/2)|^2$ and seed $I_s(r, \delta z/2) = |\Psi_s(r, \delta z/2)|^2$ intensities are calculated and used to determine the absorption coefficient $\alpha(r, \delta z)$. The pump field $\Psi_p(r, \delta z/2)$ is then modulated by the calculated absorption coefficient $\alpha(r, \delta z)$ as follows

$$\Psi_{p^*}(r, \delta z/2) = \Psi_p(r, \delta z/2) \times \exp\left[\pm\alpha(r, \delta z)\delta z\right]. \tag{2.19}$$

The sign in front of the absorption coefficient is $+$ for contra- and $-$ for co-propagating beams, respectively. The resulting pump intensity after absorption $I_p(r, \delta_z) = |\Psi_{p^*}(r, \delta z/2)|^2$ is used in the calculation of the gain $G(r, \delta z)$ coefficient and temperature gradient $\Delta T(r, \delta z)$. When calculating $\Delta T(r, \delta z)$, it is important to substitute the value of P_p corresponding to the absorbed pump $I_p(r, \delta z)$ and not the starting power P_p. The seed field $\Psi_s(r, \delta z/2)$ is then modulated in amplitude by the gain distribution $G(r, \delta z)$ and in phase by the change in refractive index $\Delta n(r)$ as follows

$$\Psi_{s^*}(r, \delta z/2) = \Psi_s(r, \delta z/2) \times \exp\left[(G(r, \delta z) - ik\Delta n(r, \delta z))\,\delta z\right], \tag{2.20}$$

so that the amplified seed intensity becomes $I_s(r, \delta z) = |\Psi_{s^*}(r, \delta z/2)|^2$. The modulated seed and pump fields of equations 2.20 & 2.19, respectively, are then propagated the remaining $\delta z/2$ distance to complete the first $N_{z=1}$ interval. These fields are then used as the input fields to the next $N_{z=2}$ interval and the calculation steps above are repeated. This iterative procedure continues until the pump and seed fields have propagated over all N_z slices spanning the length of the crystal.

2.3 Experimental Setup

To validate the theoretical 3D model, we performed a single-pass amplification of a Gaussian beam using a compact end-pumped Nd:YAG MOPA in a contra-propagating pump and seed configuration, schematically shown in Figure 2.7. The Nd:YAG crystal (properties summarised in Table 2.1) was end-pumped using an MMFC diode laser ($\phi_{\text{core}} = 400$ μm) with a central wavelength emission range of $\lambda_0 = 803 - 808$ nm, a spectral bandwidth of $\Delta\lambda = \pm 1.85$ nm and maximum output power of $P_p^{\max} = 38$ W. The output fiber face of the MMFC diode laser was 1:1 imaged to the face of the Nd:YAG crystal (plane-B) using a pair of $f_2 = 100$ mm lenses in a $4f$ configuration to achieve a uniform intensity FT profile with an FWHM radius of $\omega_f^p = 200$ μm. The pump beam radius (Gaussian-like intensity) that exited the crystal (plane-A) was measured to be $\omega_i^p = 1.7$ mm. The pump light was passed through a 45° dichroic mirror D_1 which was high-reflective coated at 1064 nm wavelength and anti-reflective coated at 808 nm wavelength to allow the Gaussian seed beam to be coupled out of the MOPA after amplification. The Gaussian seed beam was obtained from a master oscillator with wavelength, power and beam quality of $\lambda_s = 1064$ nm, $P_s = 100$ mW and $M^2 = 1.04$, respectively. The Gaussian beam output from the MO was first collimated and

Parameter	Symbol	Value	Unit
Seed Beam			
Seed input power	P_{s}	0.100	W
Seed wavelength	λ_{s}	1064	nm
Seed waist radius	ω_0^{s}	175	um
Pump Beam			
Pump input Power	P_{p}	0 - 38	W
Pump wavelength	λ_{p}	802 - 808	nm
Pump waist radius	ω_0	200	um
Pump waist radius	ω_f	1.7	mm
Crystal Properties			
Crystal length	L	25	mm
Crystal radius	R	2	mm
Atomic dopant	-	0.5	%
Number of active ions	N_{tot}	0.69×10^{20}	cm^{-3}
Index of refraction	n_0	1.82	-
Fluorescence lifetime	τ_{em}	240	μs
Absorption cross-section (dynamic)	$\sigma_{\mathrm{abs}}^{\mathrm{p}}$	$5.9-9.1\times10^{-21}$	cm^2
Absorption cross-section (peak)	$\sigma_{\mathrm{abs}}^{\mathrm{p*}}$	5×10^{-20}	cm^2
Emission cross-section	σ_{abs}^{s}	2.8×10^{-19}	cm^2
Young's modulus[a]	M	3×10^{10}	Pa
Poisson's ratio[a]	ν	0.25	-
Heat-sink temperature	T_{sink}	294	K
Thermal conductivity[b]	k_0	10.5	$\frac{\mathrm{W}}{\mathrm{m\cdot K}}$
Fitting temperature[b]	T_0	300	K
Fitting parameter[b]	ξ	-0.77	-
Thermal conductance[c]	h_{c}	1.6×10^{4}	$\frac{\mathrm{W}}{\mathrm{m^2.K}}$
Elasto-optic coef.[a]	p_{11}	-0.029	-
Elasto-optic coef.[a]	p_{12}	0.0091	-
Elasto-optic coef.[a]	p_{44}	-0.0615	-

TABLE 2.1: Summary of Nd:YAG properties: The parameters marked with superscripts 'a' and 'b' were obtained from references [176] and [157], respectively, while parameter 'c' was calculated using the method outlined in reference [156].

focused through a $f_1 = 200$ mm lens to obtain a beam radius of $\omega_{\mathrm{g}} = 181$ μm at the entrance face of the crystal (A) and a beam waist radius of $\omega_0 = 175$ μm at the pumped-face of the crystal (B). The power of the MMFC pump and Gaussian beams were analysed using a power meter (Gentec model: UP19K-30H-H5-D0) and spatially characterized using a CCD camera (BeamGage model: SP503U).

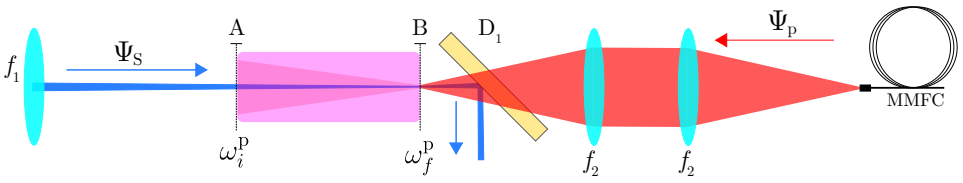


FIGURE 2.7: Schematic diagram of the single-pass end-pumped experimental configuration.

2.4 Results and Discussion

2.4.1 MMFC Diode Vs FT-Gaussian Spatial Transformation Comparison

The accuracy of modelling an in-line end-pumped amplifier hinges on some experimental verification steps as the behaviour of laser crystals and MMFC diode lasers vary based on manufacturer. To ensure that the FT to Gaussian beam shaping process is physically representative and accurate, the experimentally measured MMFC pump beam radius at the entrance ($z = 0$) and exit ($z = L$) faces of the crystal are used as the ω_i and ω_f inputs for the phase transformation in equation 2.4, respectively. The intensity profiles between the entrance and exit faces ($0 < z < L$) follow a smooth transition from a FT to Gaussian-like profiles.

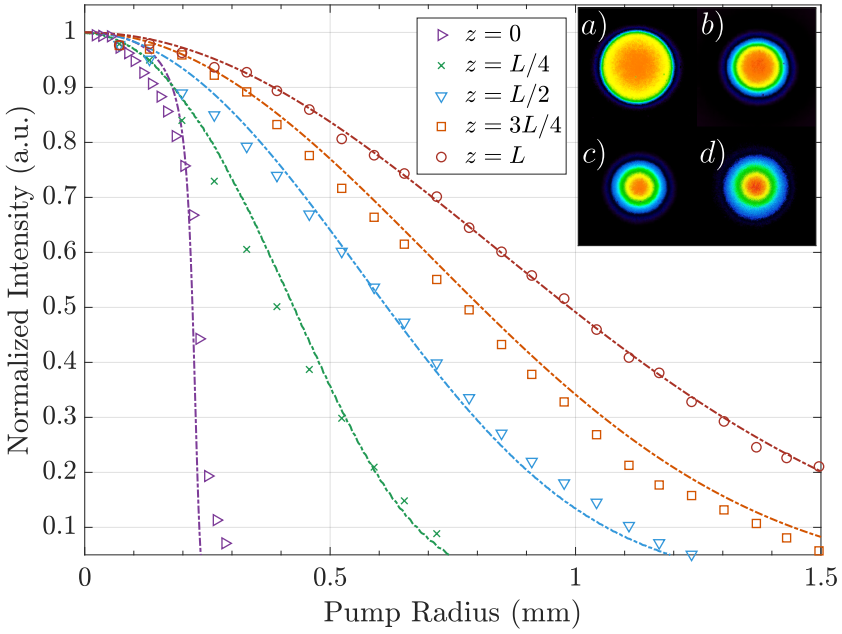


FIGURE 2.8: The figure illustrates a comparison between the FT-Gaussian beam shaping profiles (represented by dash-dot lines) and the measured MMFC diode output (indicated by markers) at various points along the free-space propagation corresponding to the crystal length, specifically at $z = 0$, $L/4$, $L/2$, $3L/4$, and L. The inset of the figure displays the experimental 2D intensity profiles of the MMFC pump beam measured at $z = 0$, $L/4$, $3L/4$, and L, labeled as a, b, c, and d, respectively.

The beam profiles at positions $z = 0$, $L/4$, $L/2$, $3L/4$ and L were experimentally measured as represented by data points in Figure 2.8 with 2D intensity profiles provided in the inset for $z = 0$, $L/4$, $3L/4$ and L corresponding to $a - d$, respectively. Based on the measured beam sizes at $z = 0$ and $z = L$, the corresponding FT to Gaussian transformation (dotted lines) compares exceedingly well with the experimental data with spatial overlap percentages of 98%, 95%, 99%, 94% and 96%, at positions $z = 0$, $L/4$, $L/2$, $3L/4$ and L, respectively. While the experimental data at $z = 0$ is slightly more rounded than the simulated FT, varying the position of the crystal relative to the length of the Fourier lens f in equation 2.1, the roundness of the FT at $z = 0$ can be controlled. We found that for a crystal of length 25 mm a Fourier lens of length $f = 25.5$ mm produces a FT beam that is slightly rounded and maintains the correct steepness.

2.4.2 Absorption cross-section calibration

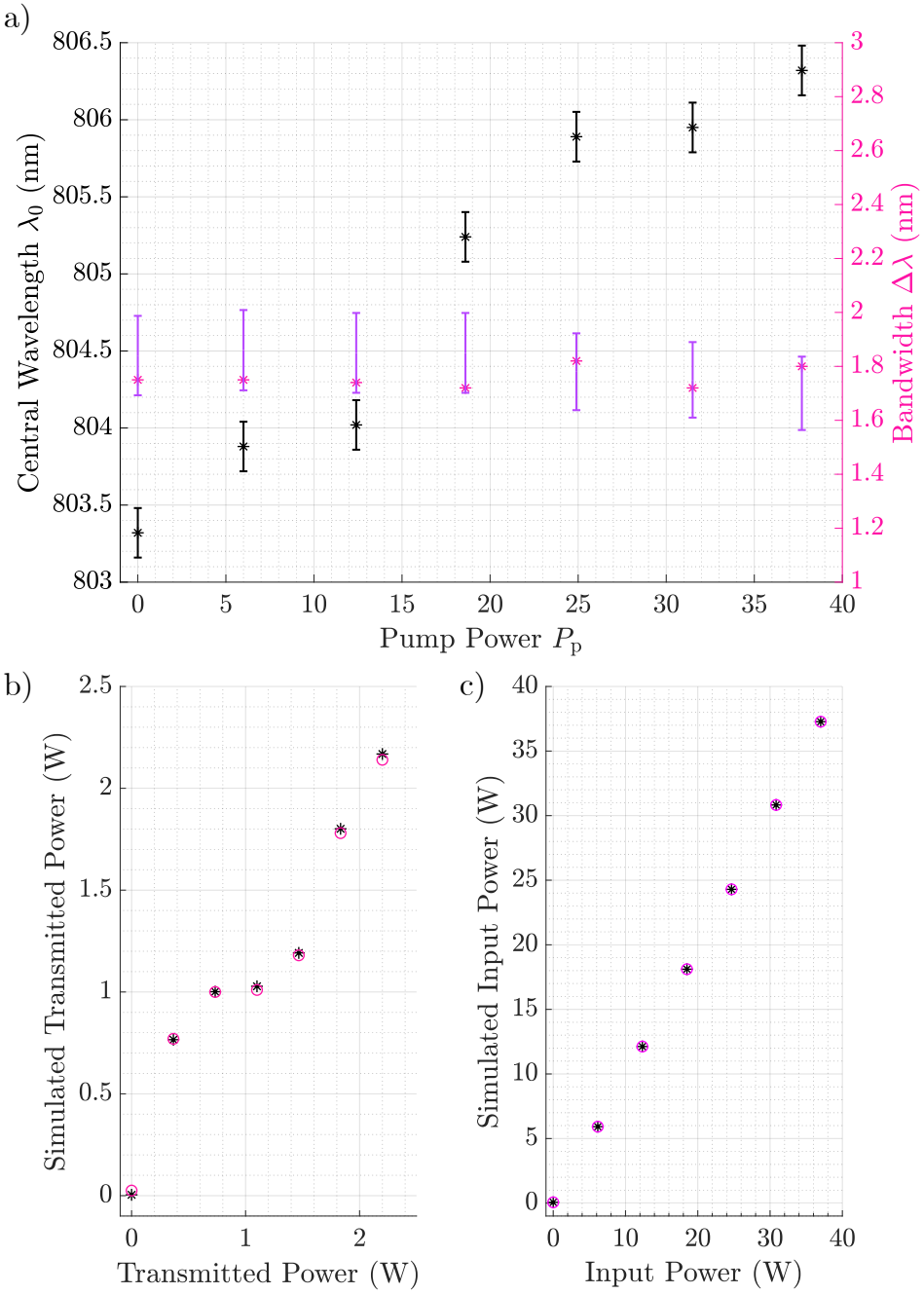


FIGURE 2.9: Plot a) shows the experimentally measured (± 0.1 nm error bars) central wavelength λ_0 (left axis, black) and spectra bandwidth $\Delta\lambda$ (right axis, magenta), with the optimal values used in the simulation (asterisk). Plots b) and c) are experimentally measured (black asterisk) and simulated (magenta circles) values of the transmitted and input pump beam powers, respectively.

The energy transfer between the pump and crystal is as important as the spatial evolution of the pump beam. As mentioned previously, each laser crystal and MMFC diode laser will vary based on manufacturer and to ensure that the 3D model was performing within the physical parameters of the crystal absorption properties, a simple experimental calibration procedure was performed by measuring the input and transmitted pump powers, central wavelength λ_0

and spectral bandwidth $\Delta\lambda$ values at 7 calibration points, evenly spaced between fluorescence emission ($\sim$ mW′s) to the maximum output pump power (38 W).

The calibration of the input power is equivalent to the measured output power of the MMFC diode laser as illustrated in Figure 2.9 c). Here, the measured power is represented by black asterisks and the magenta circles are the input power values as selected for the simulation for each of the 7 calibration points. The transmitted pump power after absorption through the crystal (black asterisk) as in Figure 2.9 b) illustrates non-linear behaviour as compared to the input powers in c). This is due to the shift in the pump emission central wavelength λ_0, shown in Figure 2.4, which causes $\sigma^{\mathrm{p}}_{\mathrm{abs}}$ and $\alpha(r,z)$ in equation 2.10 to vary as a function of the driving current.

To arrive at the correct transmitted powers from the simulation, an acute adjustment to the $f(\lambda)$ Lorentzian function used in equation 2.7, at each calibration point is required, to achieve the correct $\alpha(r,z)$ value. This is done by experimentally measuring the central wavelength λ_0 (left axis) and spectra bandwidth $\Delta\lambda$ (right axis) used to generate $f(\lambda)$ as shown Figure 2.9 a) at each of the 7 calibration points. Here, λ_0 (black asterisk) increases with the pump power in a non-uniform manner, however, $\Delta\lambda$, purple error bands, are relatively constant over the pump powers. The sensitivity of the spectrometer (Ocean Optics USB2000) is ± 0.1 nm on the the spectral bandwidth measurement and as such, the data is represented as error bands and not individual points.

The relative error in the measurement of $\Delta\lambda$ is much larger than λ_0. Therefore, $f(\lambda)$ is optimized by making small adjustments to the $\Delta\lambda$ value at each calibration point within the error band, until the transmitted powers in the model are in agreement with the experimental data points. The magenta points on a) represent the optimal values of $\Delta\lambda$ that produce the best fit (magenta circles) in b) for each of the calibration points. These steps calibrate the model with respect to the absorption cross-section. Here, 7 calibration points were selected, however, this process may be extended to include more calibration points as desired.

This calibration approach holds for both co- and contra-propagation configurations. In the co-propagation simulation, P_{p} is set to a calibrated value of the input power and will emerge from the crystal with the corresponding transmitted power. For contra-propagation, since the sign of the absorption coefficient is flipped, P_{p} is set to the transmitted power and exponentially grows to emerge from the crystal corresponding to the input power. Since the amplitude and phase of the seed beam are modulated at each slice N_z the absolute value of the net pump energy per interval δ_z is the same regardless of the pump propagation direction relative to the seed beam. With the calibrated absorption cross-section and associated FT to Gaussian pump transformation, the intensity of the pump beam absorption along the length of the crystal is shown in Figure 2.10. Here we see that while the majority of the absorption of the pump beam occurs within the first 2 mm, there is a large portion of the crystal that has potential gain necessitating a 3D model to completely understand the dynamics of an end-pumped amplifier.

2.4.3 SG of order n fitted to FT-Gaussian for $\Delta T(r,z)$ calculation

The analytical expression for the temperature gradient $\Delta T(r,z)$ is derived for a generalized super-Gaussian heat-load of order SG^{n} for a specified radius ω_{p}, absorption coefficient $\alpha(r,z)$ and pump power P_{p}. Since it is not feasible to solve the heat-conduction differential equation

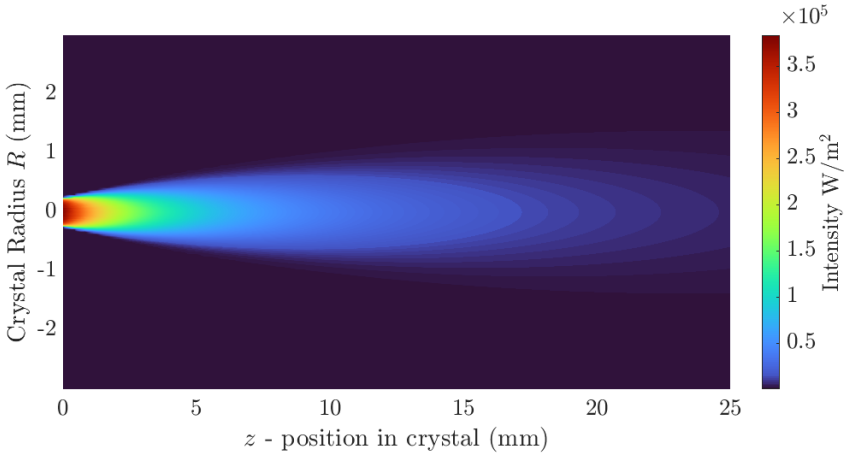


FIGURE 2.10: 2D simulation, using the calibrated absorption cross-section calculation method, of the absorption into the crystal for the Gaussian-FT evolving pump beam at maximum pump power P_{p}= 38 W.

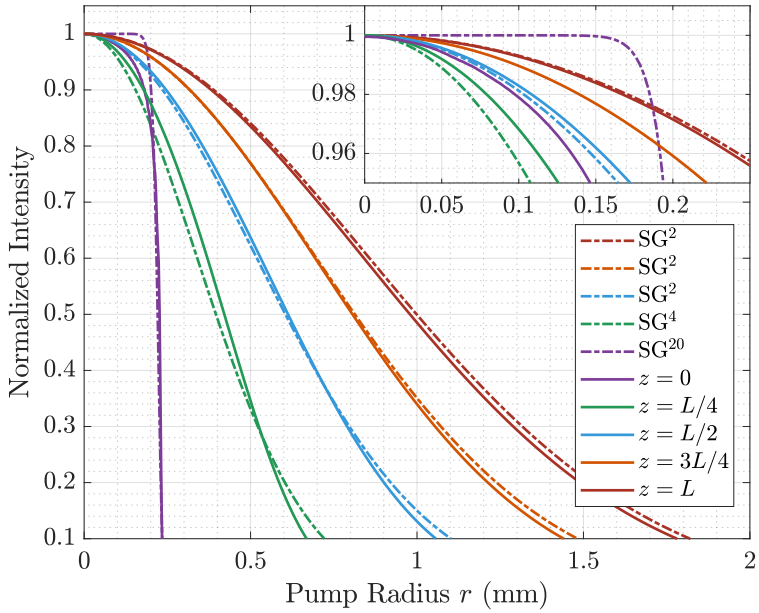


FIGURE 2.11: Gaussian-FT pump beam (solid) compared to the "best fit" super-Gaussian SG$^{\mathrm{n}}$ (dotted) used in the calculation of $\Delta T(r, z)$.

analytically at each N_z interval for the FT to Gaussian pump transformation, a "best fit" SG$^{\mathrm{n}}$ distribution was fitted to the FT to Gaussian transformation at each N_z interval. Only the order "n" of the SG$^{\mathrm{n}}$ was varied to establish a best fit, while the radius ω_{p}, absorption coefficient $\alpha(r, z)$ and pump power P_{p} were extracted at each N_z interval from the BPM procedure and substituted into equation 2.13 to obtain $\Delta T(r, z)$.

Figure 2.11 shows the normalized super-Gaussian functions of "best fit" orders of SG$^{\mathrm{n}}$ (dotted lines) for the corresponding FT to Gaussian spatial transformation (solid lines) at various points over the length of the crystal. At position $z = 0$, a super-Gaussian SG^{20} matches the steepness of the pump beam distribution accurately, but slightly overestimates the plateau flatness, as seen by the purple dotted line in the enlarged figure inset. Work by I. Cini et. al (2017), showed that variations to the peak values of $\Delta T(r, z)$ for equally sized SG$^{\mathrm{n}}$ beams

of various orders n= 2, 4, 8, 16 and 32 is marginal [156]. What is more important is the correlation of the steepness between the super-Gaussian estimation and the simulated pump beam, especially since this defines the area where the highest thermal gradient is experienced. Therefore, a slight overestimation of the pump beam flatness is traded to achieve an accurate estimation of the beam size at $z = 0$. For positions $z > 0$, the best fit values of n vary rapidly over the first few N_z intervals from SG^{20} at N_1, SG^6 at N_2, SG^4 from N_{3-6} and SG^2 for the remaining N_{7-36} slices.

2.4.4 FT-Gaussian vs SG thermal gradient

The thermal gradient over the intervals N_z is obtained by substitution of the corresponding best fit SG^n parameters: "n", ω_p, $\alpha(r, z)$ and P_p into equation 2.13. Figure 2.12, shows the dynamic temperature gradient evolution inside the crystal as a function of z under maximum input pump power of 38 W, using the calibrated absorption cross-section value. To illustrate the differences between the modelling approach presented here and that of a typical static and non-diverging SG^n approximation, we consider a SG^{20} pump beam at $z = 0$ as shown in Figure 2.13. The 3D plots in figures 2.12 a) & 2.13 a), have a similar form with the pumped end of the crystal at $z = 0$ having the highest peak temperature gradient that dissipates as the pump beam is absorbed into the crystal. As illustrated, the thermal gradients of the two decrease at different rates along the length of the crystal which is evident in the 2D and 1D plots of the respective images. This is primarily due to the non-diverging nature of the static SG^{20} pump beam approximation whereas in the Gaussian-FT dynamic pump beam approximation, the temperature gradient rather exhibits a more natural dispersion over the crystal length. We can further quantify these differences by analysing the 1D traces through the crystal, as shown in figures 2.12 c) & 2.13 c). At $z = 0$, the static and dynamic pump beams produced thermal profiles of the same shape and peak value of $\Delta T \sim 17.5$ K, as expected, since they are both the same SG^n approximations at $z = 0$. Additionally, we can clearly see the quadratic radial dependence of the temperature gradient in the region of the pump beam and the transition to a logarithmic dependence so that $\Delta T(R, z) = 0$ at the crystal boundary. For $z > 0$ the quadratic thermal gradient of the non-diverging super-Gaussian approximation is retained and remains centralised throughout the crystal compared to the dynamic approach which smooths out gradually. The peak ΔT values for the static pump beam exceeds the dynamic pump beam by 1.4×, 1.8×, 2.2× and 2.6× at $z = L/4$, $L/2$, $3L/4$ and L, respectively.

2.4.5 Change in Refractive Index

The thermal gradient gives rise to a change in the refractive index $\Delta n(r)$ as shown in Figure 2.14. Here, we compare the corresponding $\Delta n(r)$ produced by the static SG^{20} (dotted lines) and FT-Gaussian pump beams (solid lines), at various z-positions along the length of the crystal and it is clear that the Δn distributions follow the same spatial shape as that of the thermal gradient. $\Delta n(r)$ is calculated using equation 2.14 which includes the temperature-dependant linear expansion $C(T)$ and thermo-optic $\beta(T)$ coefficients. The inclusion of the higher order expansion terms introduces non-parabolic variations to $\Delta n(r)$, however, these effects only become apparent when $\Delta T(r, z)$ is significantly large. In this case, due to the relatively low maximum pump power $P_p = 38$ W, the peak $\Delta T(r, z) = 17.5$ K is too small to induce higher-order thermal variations and therefore $\Delta n(r)$ is reduced to the simplified

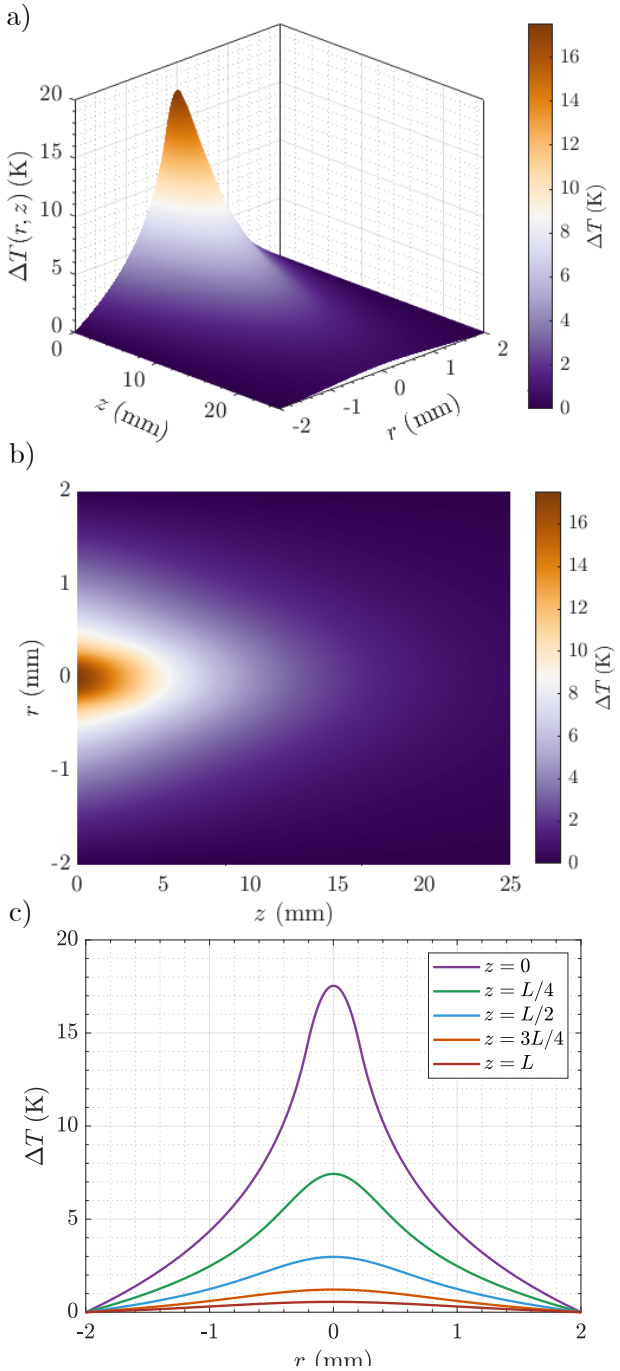


FIGURE 2.12: 3D (top row), 2D (middle row) and 1D (bottom row) visualisation of the thermal gradient $\Delta T(r, z)$ inside the Nd:YAG crystal using the SG^n approximations of the FT-Gaussian transformation pump beam.

$\Delta n = \frac{dn}{dT}\Delta T$ expression, where the thermal gradient and change in refractive index are proportional.

2.4.6 Amplification Performance

The individual components presented here are all combined in the determination of the power scaling performance of the end-pumped amplifier. As a fair point of comparison, we consider 6 cases to model where 3 are based on a fixed value for the absorption cross-section $\sigma_{\mathrm{abs}}^{\mathrm{p}}$ and

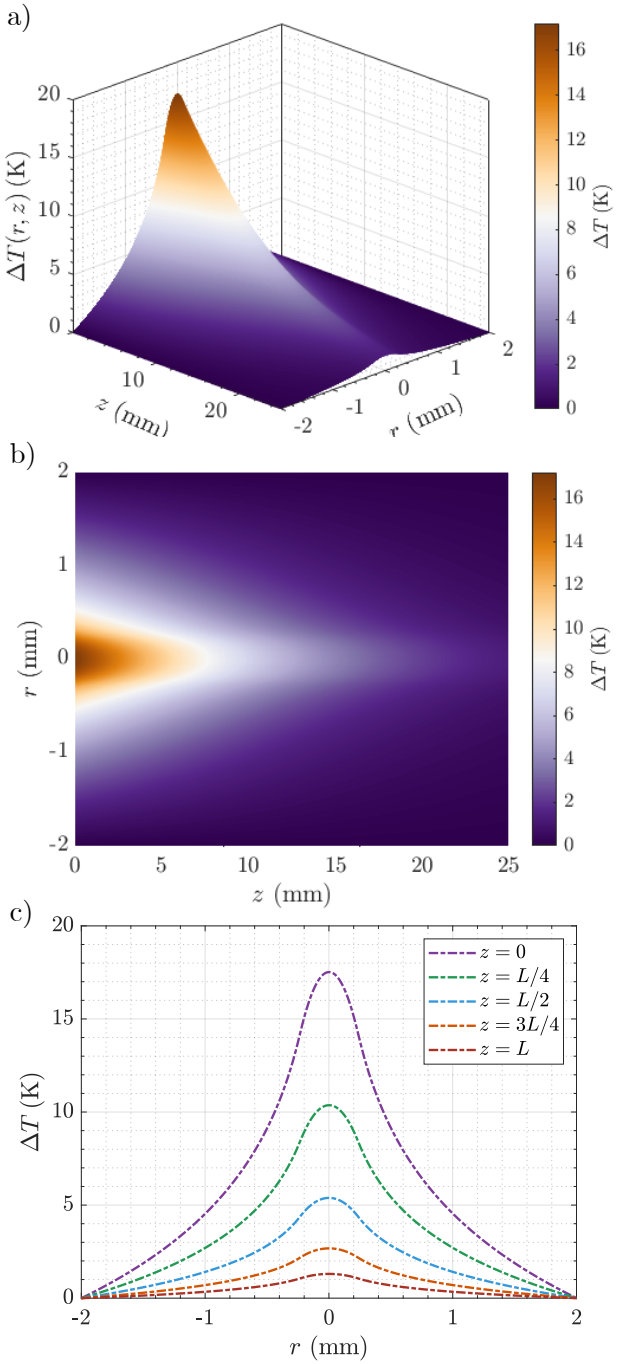


FIGURE 2.13: 3D (top row), 2D (middle row) and 1D (bottom row) visualisation of the thermal gradient $\Delta T(r, z)$ inside the Nd:YAG crystal as a result of end-pumping by a non-diverging super-Gaussian beam (left column) versus the FT-Gaussian transformation pump beam (right column).

3 consider the dynamic weighted absorption cross-section approach presented above to obtain $\sigma_{\text{abs}}^{\text{P}}$ across the pump power levels. For each subset, we consider a 2D modelling approach where only a single slice in the crystal, N_1, is evaluated. Here the pump beam is a super-Gaussian of order 20, SG^{20}, which holds for the FT-Gaussian transformation at the first slice. The remaining cases consider modelling in 3D for the static SG^{20} and dynamic FT-Gaussian pump beams, respectively as shown in Figure 2.15.

To supplement the modelling results, the experimentally obtained results (blue asterisks) for

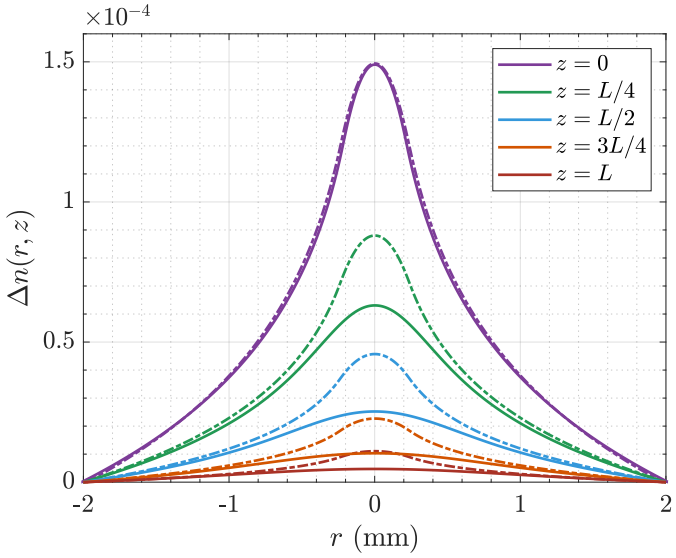


FIGURE 2.14: Comparative plot showing the change in refractive index $\Delta n(r, z)$ caused by the non-diverging super-Gaussian beam of order n=20 (dotted lines) and the FT-Gaussian transformation pump beam (solid lines), respectively, at $z = 0$, $L/4$, $L/2$, $3L/4$ & L positions of the crystals.

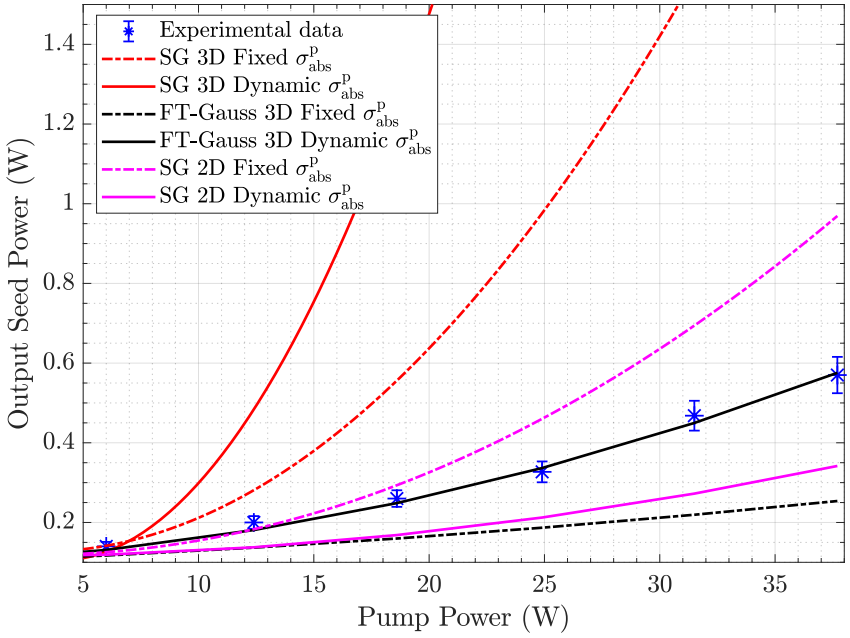


FIGURE 2.15: The red, magenta and black plot colors represent the 3D SG, 2D SG and FT-Gaussian pump beam models, respectively.

the amplification of a Gaussian beam are plotted on the same curve. Here the Gaussian beam had an input power of $P_s = 100$ mW and was amplified at pump powers $P_p = 5.8$ W, 12.4 W, 18.5 W, 25 W, 31.5 W & 38 W. The error bars correspond to a ±4% error deviation to account for the power meter and master oscillator fluctuations.

There are several interesting observations that can be made for the data presented in Figure 2.15. Firstly, the 3D models considering the static SG^{20} pump beam (red curves) drastically overestimates the power scaling potential of the amplifier as compared to the experimental data. For the case where the dynamic absorption cross-section was used, the slope of the

output power follows an almost asymptotic curve which deviates strongly from the anticipated exponential behaviour in the small signal gain region. While this behaviour was partly mitigated by considering a fixed absorption cross-section, it is clear that 3D modelling of an end-pumped amplifier using a static pump beam gives rise to significant errors. The 2D models (magenta curves) produce more reliable results which is to be anticipated as the majority of the pump absorption occurs within the first few mm in the crystal. However, as the pump power increases, the absorption of the pump beam in the crystal extends the region of gain along the crystal length due to pump saturation and the 2D models start to deviate from the experimental data more rapidly. By considering the dynamic FT-Gaussian pump beam and a fixed value of the absorption cross-section (black dashed curve) in 3D, the output power at the maximum pump power is underestimated by 2.4× in comparison to the experimental data. These results are circumvented by considering the full model specifications with a dynamic FT-Gaussian pump beam and a weighted absorption cross-section over the pump power levels (solid black curve). This gives rise to the most accurate determination of the power scaling potential as is evident with the high fidelity of the overlap with the experimental data. This model and associated calibration steps offers a holistic approach to determining the power scaling potential of in-line end-pumped Nd:YAG amplifiers.

2.5 Conclusion

In this chapter, we have demonstrated a new method of modelling in-line end-pumped Nd:YAG amplifiers in 3D. Here we considered a multi-mode fiber-coupled diode laser as the pump beam and described the transverse characteristics of the output intensity as a metamorphosis of flat-top to a Gaussian beam. This concept, borrowed from lossless laser beam shaping theory, can accurately be used to determine the beam shape transformation over a fixed distance. In creating a more robust model, the absorption cross-section was treated as a weighted variable based on the output spectrum of a physical diode laser across a variety of pump powers. Both the pump beam and the absorption cross-section require physical inputs and calibration to accurately represent their behaviour. These two components were combined with analytical expressions for the gain and absorption coefficients, thermal gradient and change in refractive index to produce a 3D model that harnessed a beam propagation method. The validity of the model was compared to the experimental amplification of a Gaussian beam at 1064 nm and demonstrated a high degree of overlap. The model presented here offers a new approach to accurately model in-line end-pumped amplifiers in 3D for cubic materials such as Nd:YAG.

Chapter 3

Amplification of higher-order Laguerre-Gaussian modes using a dual-pass MOPA system

3.1 Introduction

Many commercially available high-power lasers used in laser-enabled manufacturing processes such as welding [179], cutting [180], drilling [181], additive manufacturing [182] and surface hardening [183], employ either a Gaussian or multi-mode output. It is well-known that the spatial intensity profile of a laser beam directly influences the heat-affected zone (HAZ) during material processing which influences the overall performance of the process. To further improve on the efficiency of laser-enabled processes, laser outputs that are structured light fields have been investigated in comparison to a Gaussian or multi-mode beam. It has been shown that laser beams with a uniform intensity profile, commonly referred to as top-hat or flat-top beams, are better suited for micro-processes such as micro-hole drilling [184, 185], micro-channel scribing [186] and laser powder bed fusion (LPBF) [187]. Additionally, the use of non-diffracting Bessel beams [188] in additive manufacturing results in narrower, deeper and more controllable melt pools with a significant reduction in keyhole formation [189], while also maintaining a tight focus in the focal plane [190]. Annular or "doughnut" shaped beams have also been shown to drastically enhance the symmetry, stability and robustness of the direct metal deposition process [191, 192]. Higher-order Laguerre-Gaussian, LG_3^3 modes have been shown to offer a reduction of thermal noise in ultra-high precision interferometry for gravitational wave detection [193–195] and LG_p^l radial modes have the potential to achieve a smaller focal volume as compared to a Gaussian beam which is beneficial to micro-processing and super-resolution imaging [196, 197]. The structured light fields mentioned above represent only a fraction of an infinitely large state space of structured light fields that exist [198], either as pure eigenmodes or arbitrary fields. Given the marked impact structured light fields have demonstrated on laser-enabled processes amongst others, expanding this state space and incorporating structured light as a dynamic tool for enhancing the resolution, speed and efficiency of current laser-enabled processes pivots on beam shaping technologies which will enable the expansion of novel development areas. Structured light fields can be generated internal [199] or external [67] to a laser cavity using either linear or non-linear [200] techniques. Intra-cavity-generated light fields can be separated into static and dynamic approaches. Here,

static approaches consider an experimental system that is typically fixed to a single output field and will require a redesign of the optical cavity to select a different output field. There has been significant work in this area in achieving higher-order laser modes [201], particularly Laguerre-Gaussian modes which include birefringence effects [80], interferometric mode transformation [92], astigmatic mode converters [89, 202, 203], optical parametric oscillators (OPO) [84, 204, 205], annular pumping [82, 83, 206] and exploiting spherical aberration [93, 94, 207]. In contrast, dynamic approaches use a fixed optical system to select a variety of output beams through some external physical stimuli such as modifications to the distances between components [208] or physical movements of mirrors, crystals, components, or the pump beam along the x and y axis [91, 201, 209, 210]. Digital-based modifications may also be implemented to select a variety of modes, as was done in the digital laser [102] where a liquid crystal on silicon spatial light modulator was incorporated as the back mirror in the laser cavity to produce on-demand eigenmodes. These approaches have unlocked a much larger state space that is available to be implemented in applications. While much of the existing approaches span power levels up to kW outputs [135, 136, 211–216], these systems have limited flexibility over the spatial profile of the output beam. Furthermore, outputs from intra-cavity beam selection approaches are fixed to eigenmodes of the cavity and arbitrary selection of structured light fields and their superpositions at a desired power level are not yet achievable. Extra-cavity dynamic beam shaping approaches typically convert a Gaussian beam into a desired structured field using phase modulating devices, such as digital-micro-mirror devices (DMDs) [68, 118, 217, 218] and spatial light modulators (SLMs) [219]. These devices are re-programmable and can address arbitrary and complex-phase profiles [75, 220], providing a platform to achieve near real-time and flexible beam shaping on demand. While such approaches are efficient in selecting both eigenmodes and arbitrary fields, they are limited in their power handling capability and restrict their usage in applications > 4 W.

Several cases of lower-order Laguerre-Gaussian modes, such as Gaussian and vortex modes produced with static beam shaping elements have been power scaled with end-pumped crystal rod MOPAs [120, 129, 221], as well as amplification of vectorial vortex modes with side pumped crystals [130, 131] at low powers. To our knowledge, only one example of pure higher-order Laguerre-Gaussian modes, generated with an SLM, has been amplified using a single end-pumped Rubidium MOPA stage [138], but again at low output powers < 30 mW. To achieve desired power levels of > 10 W, inline MOPA systems may be stacked into a chain of multiple amplification stages [222, 223]. The modular implementation of multiple MOPA systems also allows for aberration correction to be performed between each stage to preserve the beam quality [224–227]. Laser beam power-scaling with an end-pumped MOPA, specifically those with cylindrical crystal rod geometries of high aspect ratio (i.e., $L > R$), typically only pass through the excited gain medium once for single-pass amplification. However, to maximise the output power, its desirable to implement a dual-pass system which has been shown using polarization optics [228, 229] or high-reflective dichroic mirrors [230] for improved efficiency. While these configurations result in higher extracted gain, they are susceptible to parasitic effects which cause the MOPA to lase independently due to optical feedback. Additionally, it is difficult to control the beam size of the return pass in these systems, which may result in sub-optimal spatial overlap between the seed and pump beams.

In this chapter, we present a novel controllable dual-pass pre-amplifier used to amplify higher-order Laguerre-Gaussian LG_p^l modes at a wavelength of $\lambda = 1064$ nm. We first discuss current end-pumped design configurations and limitations and demonstrate a new elegant design that

allows for efficient, controllable and parasitic free dual-pass amplification using polarization optics. The higher-order Laguerre-Gaussian modes are selected through complex amplitude modulation on an SLM and the resulting beams are characterised in the beam quality. We provide a full model for a 4-level Nd:YAG crystal to simulate the amplifier performance using a split-step iterative procedure, replicating the experimental observations. We show both single- and dual-pass operation, demonstrating a dual-pass gain of up to 17×, resulting in a 300% increase in output power over the single-pass configuration.

3.2 Theory

3.2.1 End-pumped MOPA designs

Inline end-pumped amplifiers consist of a pump diode that is directed at a laser crystal where the pump light propagates along the length of the crystal. The seed beam to be amplified is propagated co-linear to the pump ensuring maximum spatial overlap. Figure 3.1 a), shows the conventional single-pass end-pumped configuration for a seed beam of arbitrary polarization. Here, the seed and pump overlap spatially over the length of the crystal and are coupled out using a 45° dichroic mirror, which has a high-reflective coating at the laser wavelength and anti-reflection coated at the pump wavelength. The photons of the pump beam are exponentially absorbed as it propagates along the z-axis of the crystal volume, according to Beer-Lambert's law, resulting in a high-to-low gradient in the gain distribution. When the seed beam is contra-propagated (opposite direction), to the pump, it experiences a small degree of amplification in the tail of the lower gain region before reaching the high gain region, resulting in slightly higher extraction energy.

The efficiency of configuration a) can be further enhanced with the realisation of a dual-pass configuration. A trivial approach for dual-pass amplification, as shown in Figure 3.1 b), is to employ a slightly rotated 0° dichroic mirror so that the first pass output is back reflected through the gain region for a second pass [230]. This design, however, has three major drawbacks: firstly, it is difficult to precisely control the size of the reflected beam resulting in poor spatial overlap with the gain region; secondly, to couple the back-reflected beam out of the MOPA requires a slight rotation of the dichroic mirror which can result in off-axis alignment with the gain region resulting in asymmetric amplification and thermal aberration effects, and aperturing or clipping effects; thirdly, when the angle between the dichroic mirror is near parallel to the crystal face of the output coupler of the master oscillator (grey mirror on the right of Figure 3.1), there is sufficient optical feedback which can result in parasitic lasing. Such an effect is the independent lasing action of the MOPA system and will occur at a certain threshold pump power which clamps the potential gain of the system.

For improved control, an on-axis dual-pass MOPA design using a polarizing beam splitter (PBS) and quarter-wave plate (QWP) combination, as shown in Figure 3.1 c) is often used [228, 229]. This configuration requires that the input beam is linearly polarised so that it can be coupled into the MOPA through the PBS. After experiencing single-pass amplification, the light exiting the crystal is converted from linear to circularly polarized light as it passes through the rotated QWP ($\phi(\frac{\lambda}{4}) = \pi/2$ phase shift) and is reflected off a parallel dichroic mirror to pass through the QWP a second time, thus transforming from circularly to linearly polarized light. The polarization orientation of the light passing through the QWP twice is orthogonal to the input polarization orientation since the total phase shift is $2 \times \phi(\frac{\lambda}{4}) = \pi$.

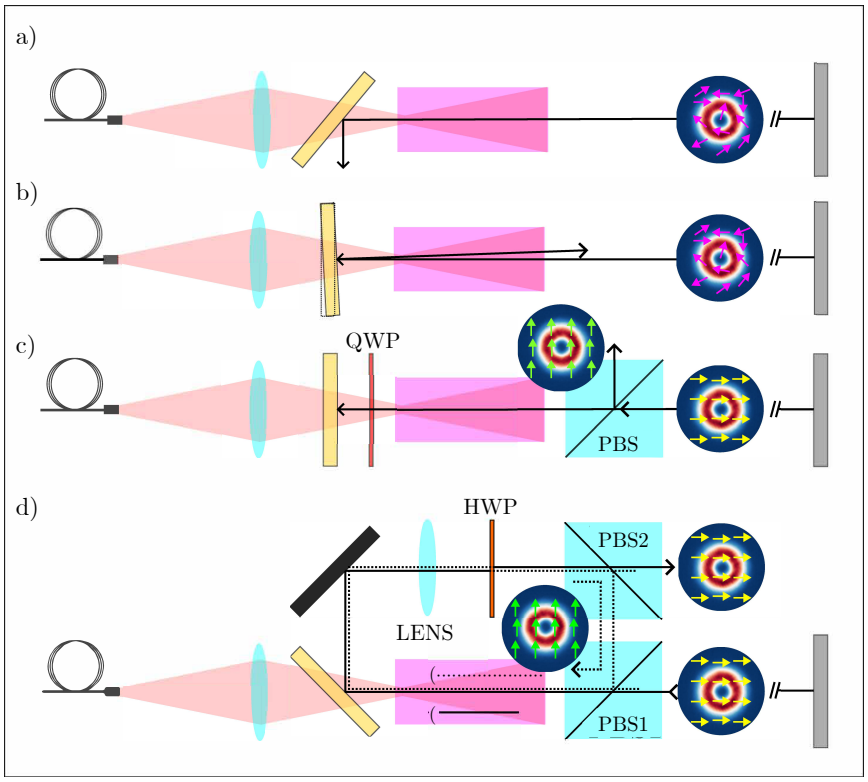


FIGURE 3.1: Schematic diagrams showing the various solid-state crystal (magenta) end-pumped MOPA configurations to achieve single-pass and/or dual-pass amplification. a) Single and b) dual-pass MOPA configurations for an unpolarized input beam using a dichroic mirror (yellow rectangles). Diagrams c) and d) are dual-pass configurations of linearly polarized input beams, requiring polarization-based optics such as half-wave plates, quarter-wave plates (thin red rectangle), and polarizing beam splitter cubes (light blue square). The Fibre-coupled diode laser pump beam (shaded red) is imaged using a single lens (light blue) into the MOPA system. The output coupler (grey rectangle) of the laser resonator is shown and the broken line indicates subsequent beam shaping and/or optical components.

The orthogonally polarized light is then reflected off the PBS and coupled out of the MOPA system after being amplified a second time. This design allows for an on-axis dual-pass alignment of the seed, however, it does not allow for acute control of the beam size on the return pass. Additionally, due to the extinction ratio of typical high-power PBSs (>2000:1), optical feedback to the output coupler is not eliminated and parasitic lasing will occur albeit at a higher pump power threshold.

In Figure 3.1 d), we present a dual-pass interferometric MOPA design, similar to a ring amplifier in pulsed laser systems. This design allows for improved control over the second pass beam size using a 1:1 imaging lens positioned inside the MOPA system while suppressing any optical feedback to the output coupler. In this design, a horizontally polarized input beam passes through PBS1 and undergoes single-pass amplification. The output from the crystal is then reflected off two rotated dichroic mirrors, each at 45°, and directed through a HWP ($\phi(\frac{\lambda}{2}) = \pi$) that induces a 90° rotation of the polarization direction to produce vertically polarized light. PBS1 and PBS2, which are highly reflective to vertical polarization states, are used to redirect the beam to pass through the crystal for a second pass (black dotted line). The dual-pass output then follows the same optical path as the first-pass output and is converted from vertical to horizontally polarized light after passing through the HWP and

is coupled out of the system at PBS2. The beam size in the amplifier is controlled using a positive lens f which is positioned carefully so that the pumped face of the crystal is imaged back to itself. This ensures that one round trip inside the amplifier is exactly $4f$ to this image plane and that the beam size at the pumped face of the crystal is kept identical on single- and dual-pass.

3.2.2 Overlap Integral

The overlap η of the spatially varying LG_p^l modes with the pump beam at each N_z-interval of the crystal can be calculated from [231]

$$\eta(N_z) = \frac{\int \mathrm{d}y \int I_\mathrm{p}\,(x,y,N_z)\, I_\mathrm{s}\,(x,y,N_z)\,\mathrm{d}x}{\int \mathrm{d}y \int I_\mathrm{p}\,(x,y,N_z)\, I_\mathrm{p}\,(x,y,N_z)\,\mathrm{d}x}\,, \tag{3.1}$$

where I_p and I_s are the intensities ($\mathrm{W/m^2}$) of the pump and seed fields, respectively, corresponding to the interval N_z. It is important to note that typically the intensities I_p and I_s are normalized to unity. This is relevant in laser resonator calculations where the spatial overlap between eigenmodes and the gain, based on the cavity design, determines which modes will lase. In amplifiers, however, the relative power densities and spatial overlap of the pump and mode will determine how a higher-order mode will power scale relative to a Gaussian beam and thus the normalization of the respective intensities is not required.

3.3 Experimental Setup

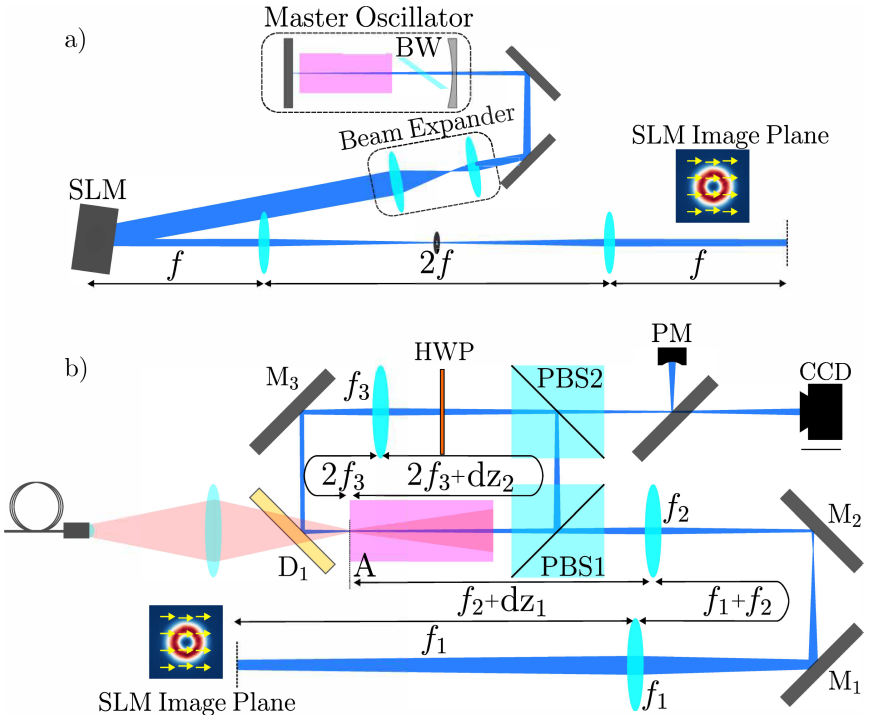


FIGURE 3.2: Schematic diagram showing a) the master oscillator and beam shaping setup using the spatial light modulator with $4f$ spatial filtering, and b) a detailed optical layout of the novel dual-pass end-pumped MOPA setup used in the experiment.

The experimental section comprises two parts: part a) is the LG_p^l mode generation setup using an SLM, and part b) is the dual-pass MOPA configuration, depicted schematically in Figure 3.2.

3.3.1 LG_p^l mode selection using the SLM

In part a) of Figure 3.2, an Nd:YAG master oscillator with an internal Brewster window (BW) was constructed to provide a 4 W cw horizontally polarized Gaussian beam operating at a wavelength of $\lambda = 1064$ nm. The Gaussian beam output was magnified and collimated using an afocal telescope to a D4σ beam diameter of 22 mm and the corresponding beam was directed to an SLM device (PLUTO-2.1-NIR-015). At the plane of the SLM screen, the effective power density was ~ 2 W/cm^2 which is the damage-threshold limit for this device. The respective higher-order LG_p^l modes were selected by addressing the SLM with complex-amplitude phase holograms using equation 1.9 at z = 0, with a beam waist radius of ω_0 =0.9 mm. To maintain a consistent beam size at the SLM image plane, the LG_p^l beams were scaled according to their respective M^2 to all have the same second moment radius as the fundamental Gaussian LG_0^0 beam using the factor of $\sqrt{2p + |l| + 1}$. The resultant beams were selected by imaging the SLM screen using a pair of $f = 500$ mm lenses placed in a $4f$ imaging configuration with a variable aperture placed between the two lenses, as depicted in Figure 3.2 a). The aperture was positioned to only select the first order of diffraction resulting in the outputs displayed in Figure 3.3. To keep the power at this plane fixed for all the modes, the output power from the master oscillator was carefully adjusted for each mode to $P_s = 100$ mW $\pm$ 5 mW.

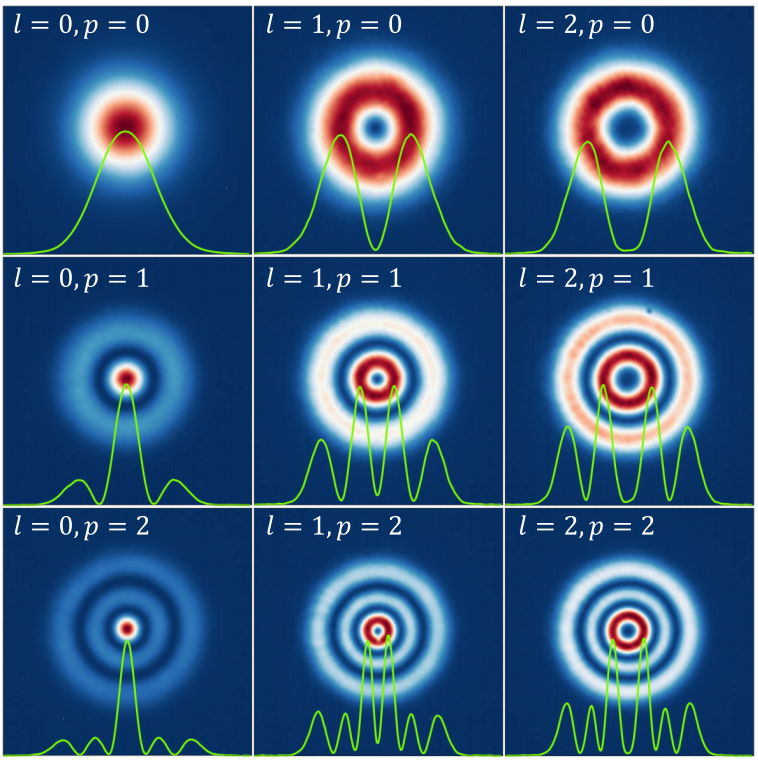


FIGURE 3.3: Experimental data showing the spatial profiles of the various LG_p^l modes selected using complex-amplitude shaping on a spatial-light modulator before undergoing dual-pass amplification, with the radial cross-section shown as the green profile. The Laguerre polynomial orders are given in the insets.

3.3.2 Dual-pass MOPA system

In part b) of Figure 3.2, the pump source in the amplifier was an 808 nm wavelength fibre-coupled diode laser with a 400 μm core diameter, providing a cw pump power of up to $P_{\mathrm{p}} = 38$ W maximum. The fibre tip was imaged onto the face of the amplifier Nd:YAG crystal to a FHWM spot size of $\omega_p = 200$ μm. The image plane of the SLM was demagnified and relay imaged through a PBS to the pumped face of the Nd:YAG crystal using a $f_1 = 500$ mm and $f_2 = 100$ mm which resulted in a beam width of $\omega_0 = 180$ μm at the crystal face, marked as position A. Due to refraction effects caused by propagating through the PBS (UV Fused silica, $L_{\mathrm{PBS}} = 25.4$ mm and $n_{\mathrm{PBS}} = 1.45$) and Nd:YAG crystal (properties summarized in Table 3.1), the distance from lens f_2 to the image plane A is shifted longitudinally by a distance $\mathrm{dz_i} = L_{\mathrm{i}}\frac{n_{\mathrm{i}}-1}{n_{\mathrm{i}}}$, where L_{i} is the length of a transparent media of refractive index n_{i}. The adjusted focal position was at distance $f_2 + \mathrm{dz_1}$ after lens f_2, where $\mathrm{dz_1}$ includes a shift caused by the PBS and Nd:YAG media (i.e. $\mathrm{dz_1} = \mathrm{dz_{PBS}} + \mathrm{dz_{YAG}} = 19.14$ mm).

The corresponding beam was reflected off a 45° dichroic mirror ($\mathrm{D_1}$) and subsequently a 45° high reflecting mirror ($\mathrm{M_3}$) at 1064 nm wavelength. The beam was directed to a lens, $f_3 = 100$ mm, which was positioned at a distance $2f_3 = 200$ mm from A to perform single-lens imaging for the second-pass amplification step. The position of PBS1 and PBS2 (both Thorlabs PBS25-1064-HP) were selected such that the distance after f_3 was $2f_3 + \mathrm{dz_2} = 227.02$ mm to compensate for refraction of PBS1, PBS2 and the Nd:YAG crystal (i.e. $\mathrm{dz_2} = 2\times\mathrm{dz_{PBS}} + \mathrm{dz_{YAG}} = 27.02$ mm). A zero-order HWP (Thorlabs WPH10M-1064) was positioned between lens f_3 and PBS2 and angularly rotated for optimal horizontal to vertical polarization conversion so that the first-pass output was reflected by PBS1 and PBS2 back to the crystal. The output at PBS2 of the system corresponds to dual-pass amplification, however, to perform single-pass amplification only, without altering the general alignment of the system, the HWP was removed and a beam blocker was placed between PBS1 and PBS2 to prevent optical feedback. The output power of the system was sampled using a power meter (Gentec UP25N-100H-H9-D0) while the beams were characterized using a CCD camera (Spiricon SP620U).

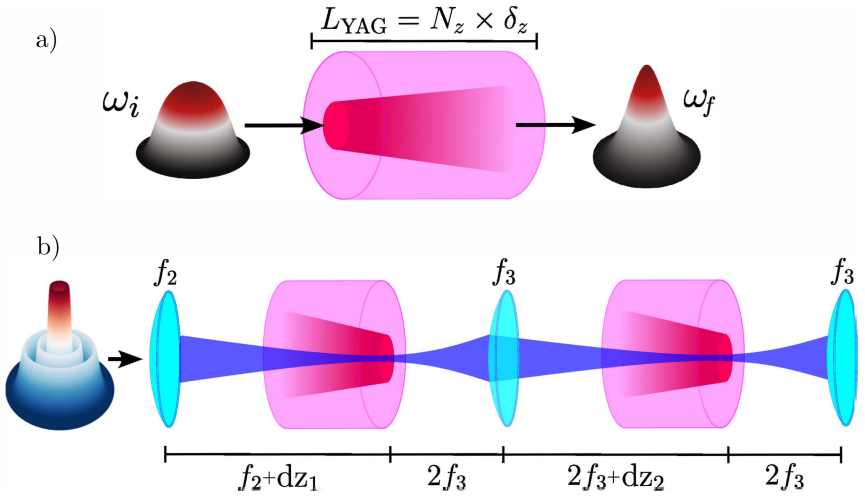


FIGURE 3.4: Schematic diagram depicting a) the spatial evolution and beam size of the fibre-coupled diode laser pump beam at the entrance (ω_i) and exit (ω_f) faces of the Nd:YAG crystal rod, and b) the simulated "unfolded" layout of the dual-pass MOPA experiment.

A 3D simulation of the dual-pass MOPA system was performed using an iterative split-step

procedure, as described in chapter 3, based on the Fourier propagation method using a flat-top to Gaussian pump beam transformation. Utilising the flat-top to Gaussian pump beam shaping method, depicted schematically in Figure 3.4 a), the model accounts for the spatial evolution and divergence behaviour of the fibre-coupled diode laser output as it propagates through the Nd:YAG crystal. Figure 3.4 b), is a schematic diagram showing the "unfolded" dual-pass experimental setup of Figure 3.2 b) that was used in the simulation. The simulation was performed in MATLAB with a mesh-grid size of $N_{x,y} = 3000$ and the length of the Nd:YAG crystal was discretized into N_z =36 intervals, so that the length of each interval was $\delta_z = L_{\mathrm{YAG}}/N_z = 0.69$ mm .

Crystal Properties	
Parameter	Value
Length (L_{YAG})	25 mm
Radius (R)	2 mm
Atomic dopant	0.5 %
Number of active ions (N_{tot})	6.90×10^{25} m^{-3}
Index of refraction n_{YAG}	1.82
Fluorescence lifetime τ_{em}	240 μs
Pump absorption cross-section $\sigma^{p}_{\mathrm{abs}}$	$5.9{-}8.8\times10^{-25}$ m^2
Seed emission cross-section σ^{s}_{em}	2.8×10^{-23} m^2

TABLE 3.1: Summary of Nd:YAG crystal properties used in the simulation.

3.4 Results and Discussion

3.4.1 Amplified LG^{l}_{p} Mode Outputs

The MOPA system was designed to be static so that only the phase profile on the SLM screen is modified when selecting different modes. The initial optimization of the position of the imaging lens f_3 was performed for the Gaussian mode and aligned for best output beam quality and highest dual-pass output power, thereafter, no alterations were made to the optical system. The 2D intensity profiles of the dual-pass amplified LG^{l}_{p} modes for an input pump power of $P_{\mathrm{p}} = 38$ W are shown in Figure 3.5. Here, the input modes are generated by the SLM at the input of PBS1 while the output was measured after transmission through PBS2. The modes maintained their transverse profiles with a high degree of spatial overlap which was confirmed by a measure of their respective beam qualities, M^2, as shown in Table 3.2. The dual-pass amplified output of the fundamental LG^{0}_{0} mode remained diffraction-limited with an $\mathrm{M}^2 = 1.01$ and as shown in Table 3.2, the beam quality of the higher-order modes was well preserved ($\sim$ 10% variation). Such minimal variations in output beam quality are to be expected since end-pumped MOPA systems are known to experience some degree of thermally-induced aberrations which may cause beam distortions, especially beams with a vortex phase component. Additionally, since the system was static and aligned for optimum Gaussian performance, misalignment sensitivity for the higher-order modes was not examined.

3.4.2 Output Power Results

The output power of the system was numerically simulated for both single- and dual-pass, as shown in Figure 3.6 a) for pump powers ranging from P_{p},= 6 W - 38 W. Here, the single-pass is represented by solid lines while the dual-pass is shown as dashed lines with the maximum corresponding power values for each mode captured in Table 3.3. The input

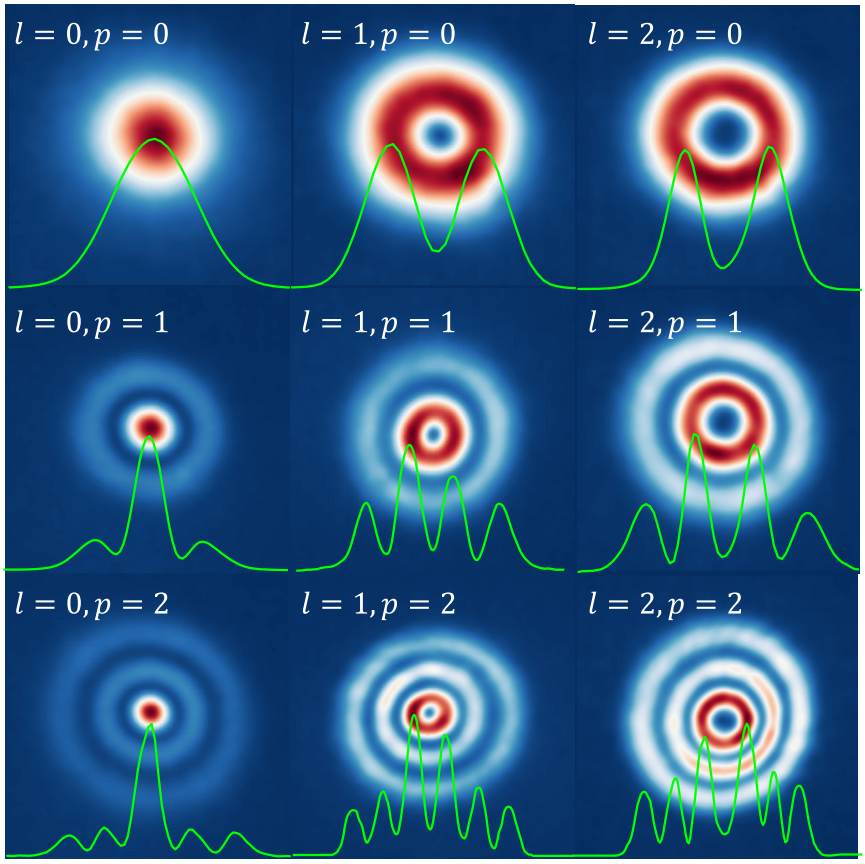


FIGURE 3.5: Spatial profiles of the various LG_p^l modes after dual-pass amplification at 38 W of pump power, with the radial cross-section shown in green.

LG_p^l	M^2 Before	M^2 After
$l = 0,\ p = 0$	1.04	1.01
$l = 1,\ p = 0$	2.07	2.52
$l = 2,\ p = 0$	3.01	3.25
$l = 0,\ p = 1$	3.02	3.29
$l = 1,\ p = 1$	4.01	4.46
$l = 2,\ p = 1$	5.03	5.47
$l = 0,\ p = 2$	5.04	5.26
$l = 1,\ p = 2$	6.03	6.36
$l = 2,\ p = 2$	7.02	7.85

TABLE 3.2: Experimentally measured beam quality M^2 factors of the LG_p^l modes Before and After dual-pass amplification at $P_p = 38$ W. Theoretically, the beam quality values scale according to $M^2 = 2p + |l| + 1$.

power for all the modes in the simulation was set to $P_s = 100$ mW and the data in Table 3.3 has been arranged in descending order of maximum dual-pass output power. There is a clear trend for the higher-order modes (excluding the Gaussian) in both the single- and dual-pass output power in that as the M^2 increases, the power decreases. This, however, is only true for modes with an azimuthal order $l > 0$. Interestingly, the descending order follows an increase in the Laguerre-Gaussian radial order where modes of the same radial order (p) are grouped together and further arranged according to an increase in the azimuthal order

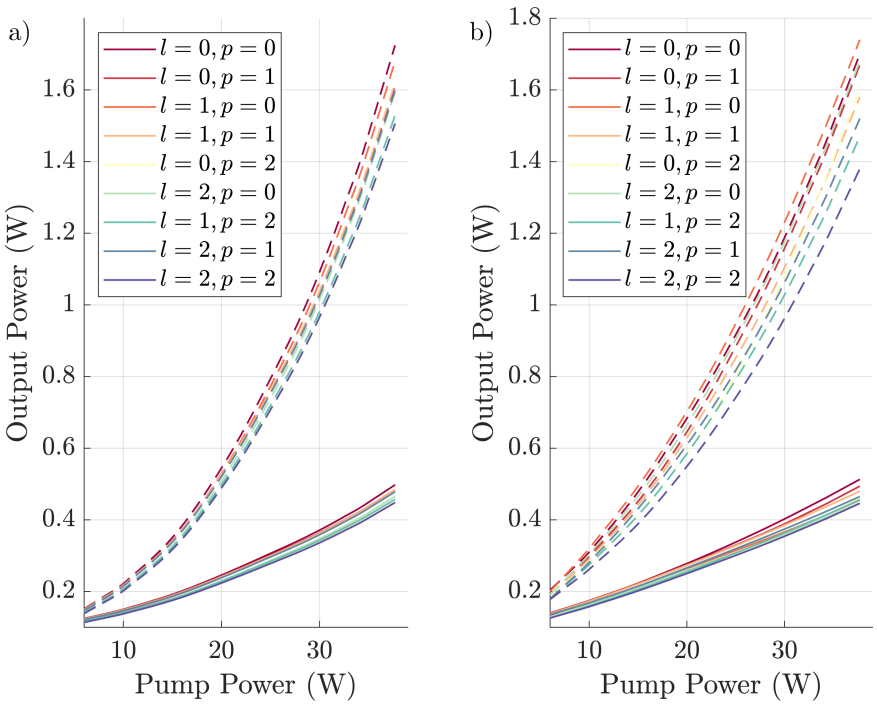


FIGURE 3.6: a) Numerically simulated amplification results and b) the experimentally measured output powers for single (solid lines) and dual-pass (dotted lines) amplification of the LG_p^l modes with incident powers $P_s = 100$ mW at input pump powers ranging from $P_p = 6$ W - 38 W.

(l). Additionally, if $p > 0$, then the lowest power for a particular group of the same radial order, p, is when the azimuthal order $l = 0$.

Experimentally, the output powers for both single-and dual-pass are in excellent agreement with the numerical simulations as shown in Figure 3.6 b) and Table 3.3. Here we see a significant enhancement of over 300% in the output power of the dual-pass MOPA configuration ($\sim 17\times$ gain factor) compared to the single-pass configuration ($\sim 5\times$ gain factor), for all the LG_p^l modes. The fundamental Gaussian mode LG_0^0 recorded the highest simulated dual-pass output power of 1.737 W and corresponded well with the experimentally measured output power of 1.70 W. As before, the system was aligned for maximum single- and dual-pass output power using the Gaussian mode and only the phase screen was varied when measuring the higher-order modes. Given the minor variations seen in the M^2, especially for higher M^2 values, it is expected that power variation will also be present. In addition, it must be noted that the power variation between the LG_0^0 and LG_0^1 modes may be attributed to several factors. The maximum power difference between these modes in 2.35% which is smaller that the error of the power meter of 5%. With this, the LG_0^1 mode has a better 3D overlap with the pump as compared to the LG_0^0 mode which is due to steeper skirts on the LG_0^1 mode and an increased M^2 relating to a larger beam as the mode traverses the length of the crystal. While the LG_0^0 beam has a larger saturation intensity, the LG_0^1 mode has a normalised power difference of 0.05% as compared to the LG_0^0 mode. This all contributes to the power variation and a more sensitive power measurement system will compensate for this difference.

The experimentally measured single and dual-pass output powers in Table 3.3 show a good correlation with the simulated results and show a similar order of the modal spread. Since the M^2 values, in Table 3.2, of the LG_p^l modes, saw minor variations, it was not deemed

		Simulated		Experiment		% Diff	
LG_p^l	M^2	SP (W)	DP(W)	SP (W)	DP (W)	SP	DP
$l=0, p=0$	1	0.502	1.737	0.51	1.70	1.6	2.1
$l=1, p=0$	2	0.502	1.729	0.47	1.74	6.4	0.6
$l=2, p=0$	3	0.497	1.675	0.48	1.68	3.4	0.3
$l=1, p=1$	4	0.493	1.641	0.49	1.58	0.6	3.7
$l=2, p=1$	5	0.492	1.631	0.48	1.52	2.4	6.8
$l=0, p=1$	3	0.488	1.623	0.50	1.67	2.5	2.9
$l=1, p=2$	6	0.487	1.606	0.49	1.47	0.6	8.5
$l=2, p=2$	7	0.488	1.606	0.49	1.38	0.4	14.1
$l=0, p=2$	5	0.484	1.590	0.50	1.60	3.3	0.6

TABLE 3.3: A summary of the simulated and experimentally measured single (SP) and dual-pass (DP) amplified output powers P_s of the various LG_p^l modes at maximum pump power $P_p = 38$ W with the relative % error between the simulation and experimental data in the last two columns. The data has been arranged in descending order of the simulated dual-pass output power P_s. The theoretical M^2 values are provided in the column adjacent to the corresponding LG_p^l modes.

necessary to simulate the effects of thermal aberrations. However, we believe that the presence of defocus, amongst other aberrations and misalignment sensitivity, will influence the focus position of the imaging system and the propagation of the beams through the crystal which will affect the higher M^2 modes more severely. Any distortion experienced during the first pass compounds during the relay imaging process for the second pass caused a significant deviation from the simulated results. This is especially the case for the LG_1^2, LG_2^1 and LG_2^2 modes which saw a measurable increase in percentage differences from 2.4%, 0.6% & 0.4% to 6.8%, 8.5% & 14.1% for the single- and dual-pass outputs, respectively, which are above the sensitivity range of the power meter (±3%). A comparison of the powers between the single-pass simulated and experimental data shows that minor variations will present a large % difference. These values are too small to ascertain any general trends and fall below the power meter sensitivity range. However, the dual-pass experimental data show that higher M^2 beams will deviate more significantly from the simulated data for a physically static system. In this instance, the system must be optimised for each mode in both the beam size and the alignment.

3.4.3 Pump-Seed Intensity Overlap

Using the three-dimensional model, the overlap integral between the dynamically evolving pump and LG_p^l fields inside the crystal at each N_z interval could be determined using equation 3.1. Differences in the M^2 value of the modes, especially for a fixed optical path system, directly influences the Rayleigh range and beam divergence angle as they propagate toward a focus. In Figure. 3.7, the total overlap over the crystal volume (i.e.$\sum_{N_z} \eta(N_z)$) for each LG_p^l mode during the second-pass is shown with the simulated dual-pass output powers of Table 3.3. For direct comparison, both sets of data have been normalized to unity with the x-axis representing the normalized overlap. It is clear that the trend observed for the output powers correlates well with the total overlap integral and shows that as the M^2 increases the total overlap integral and output power decreases similarly. Additionally, we can infer that the reduced net intensity overlap of the LG_1^0 radial mode is due only to its spatial profile since the LG_0^2 mode has the same M^2 and hence would have a similar Rayleigh range and beam divergence angle.

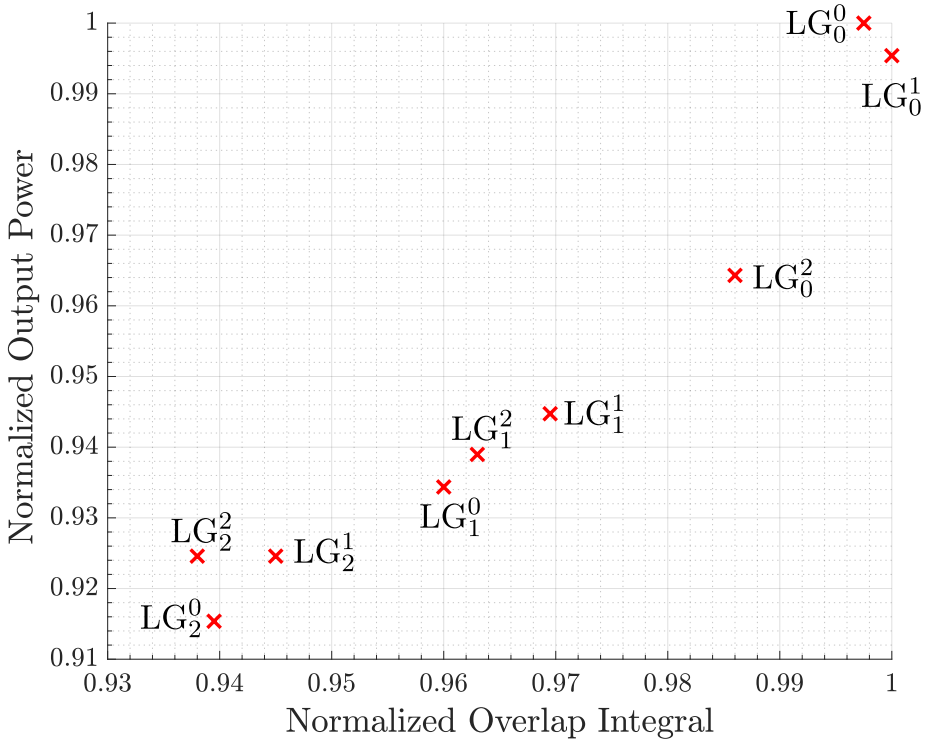


FIGURE 3.7: Simulated results showing the trend of the normalized output powers versus the normalized overlap integrals of each LG_p^l mode.

The amplification of higher-order modes under the same static experimental system (i.e., beam size at the pumped end of the crystal and input power), demonstrates that their unique spatial profiles are directly influenced by their spatial overlap with the pump region inside the crystal. Furthermore, such a system enables modes to be grouped by either the azimuthal order or radial order or both. This demonstrates that smaller groups of modes can be amplified with high fidelity in a static system, however, as the state space increases, a reduced amplification output is expected as the M^2 increases.

3.5 Conclusion

We have demonstrated the amplification of the first nine Laguerre-Gaussian modes in a novel interferometric dual-pass end-pumped pre-amplifier system that enhanced the single-pass output power by over 300% for all the modes and preserved the beam quality M^2 at the output. The MOPA design provided a highly controllable approach to achieving optimal pump and seed beam overlap during the first and second-pass amplification while showing no signs of parasitic oscillations. The simplicity and robustness of this design can easily be extended into multiple MOPA stages to achieve high-power structured light fields for high-power laser-enabled applications. Additionally, we found that effective gain extraction varies for each LG_p^l mode, showing a high correlation with the net intensity overlap with a dynamically evolving Gaussian to Flat-top pump beam inside the crystal volume. Furthermore, these results provide a further understanding of amplifying higher-order modes and the expected performance when using a spatial light modulator in a static optical system.

Chapter 4

Aberration-induced vortex splitting in amplified orbital angular momentum beams

4.1 Introduction

The annular intensity profile and twisting helical wavefront of OAM beams have been utilised in various applications, such as optical particle trapping and manipulation [232], material processing [233], free-space optical communications[234], super-resolution microscopy [235] and image processing [236]. However, LG_0^l beams of $l > 1$ promise to increase the bandwidth of free-space [237] and quantum optical communication [114] and offer greater flexibility for enhanced material ablation applications [188]. In practice, especially in manufacturing applications, average powers exceeding 20 W are required while maintaining the modal purity of the LG_0^l beams.

OAM beams are easy to create and can be generated internal (intra-) or external (extra-) to the laser cavity. Intra-cavity generation has a long history and has been extensively reviewed to date [199, 238–240], with recent advances including an interferometric mode transforming output coupler [92], astigmatic mode converters [202, 203], optical parametric oscillators (OPO) [204, 205], annular pumping [206] and exploiting spherical aberration [207]. Extra-cavity generation of OAM beams is likewise very well established [198, 241] and typically involves the transformation of a laser with a Gaussian LG_0^0 output using elements that impart an azimuthally varying phase, generally fabricated for a specific topological charge output. Further, such phase-only approaches (that impart an azimuthally varying phase to the input Gaussian beam) do not produce true LG_0^l modes; instead, they are hypergeometric modes [242] which manifest in the Laguerre-Gaussian basis as many unwanted radial modes [243]. Recent advances to overcome this include amplitude and phase control using geometric phase metasurfaces [244–246], while OAM charge tuneability can be achieved by dynamic computer-generated holograms [247] written to digital micro-mirror devices (DMDs) [248] or spatial light modulators (SLMs) [67].

Most of these approaches have been demonstrated only at low power, a limitation that can be overcome by performing power-scaling using one or more master oscillator power amplification (MOPA) modules. Power scaling of OAM beams using end-pumped MOPAs has been reported in stressed Yb fibres [249], Ho:YAG crystal rods [221], Er-doped ring core fibres

[250] and Nd:YVO_4 crystal rods [120]. In general, both the delivery of the pump light as well as its localization to a small area result in both thermal and non-thermal aberrations [227], distorting the desired mode. To date, the impact of this on OAM purity and power scaling ability has not been reported.

In this chapter, we investigate the generation and power amplification by a compact end-pumped Nd:YAG MOPA system, with the aim to produce higher-order and high purity OAM modes. We reveal that higher-order Laguerre-Gaussian (LG_0^2) beams result in vortex splitting, which we study both theoretically and experimentally with the aid of a Shack-Hartmann wavefront sensor and modal decomposition. We show that vertical astigmatism, leading to a Gouy phase anomaly, is introduced to the system via a pump beam distortion which is caused by the inherent design of compact end-pumped MOPA systems. Additionally, we show experimentally and computationally that the physical separation of the phase singularities can be reversed in the far field by exploiting the Gouy phase shift. Using these findings we are able to report an amplified vortex purity of up to 94% while achieving an amplification enhancement of up to 1200%.

4.2 Theory

4.2.1 Wavefront Aberrations

In an amplifier system, it is important not only to increase the amplitude of the input mode but to preserve its profile, both in amplitude and phase, however, we know that these systems involve energy transfer between pump photons and the crystal lattice ions. Only a portion of absorbed photons can potentially contribute towards amplification, the remaining fraction is converted to heat, defined as the quantum defect heating coefficient (η_h = 0.24-0.3 for 0.5% atm. Nd:YAG). The build-up of heat in the crystal medium changes the refractive index experienced by the input mode and causes aberrations in the wavefront $W_{ab}(x, y)$ of the amplified beam, commonly referred to as thermally-induced aberrations. A tool often used for characterizing wavefront aberrations is the Zernike Polynomials.

The Zernike polynomials and weighting coefficients can be obtained using a Shack-Hartmann wavefront sensor (SHWF) by measuring a probe beam, typically a Gaussian mode, after interaction with the aberrations, in this case, the end-pumped Nd:YAG crystal. The aberrated wavefront can be numerically reconstructed in the Zernike polynomial basis, for simplicity expressed using the singe-index (j) representation, as follows [226]:

$$W_{ab}(x, y) = W_{ref}(x, y) - \sum_{j=0}^{N} C_j Z_j(x, y) \tag{4.1}$$

Where C_j are the Zernike coefficients (units of waves) for the corresponding j_{th} Zernike polynomial $Z_j(x, y)$. From this point onward, the single-index (j) Zernike polynomial and weighting coefficient are replaced by the traditional double-index (l, n) representation (i.e. $\{Z_j, C_j\}$ $\rightarrow$ $\{Z_n^l, C_n^l\}$) according to the OSA/ANSI standard. To decouple the aberrations induced by the optical system from those caused by the end-pumped Nd:YAG crystal, a reference wavefront $W_{ref}(x, y)$ measurement with the pump beam turned off is subtracted from the wavefront

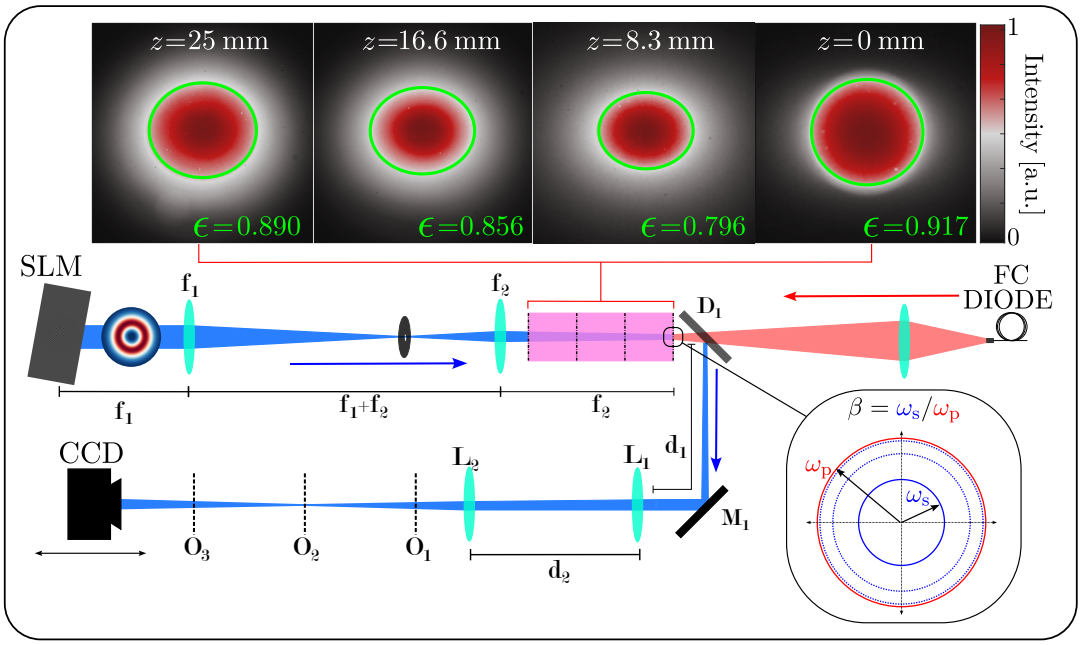


FIGURE 4.1: Schematic diagram showing the experimental layout with figure insets (top) showing the pump intensity profile (not to scale) measured at various z-positions of the Nd:YAG crystal (pink) with (green) ellipticity values (ϵ). The circled figure inset (bottom right), schematically depicts the cross-section of the fixed pump ω_{p} (red circle) and varying seed ω_{s} (blue circles) beam sizes at the pumped face of the crystal ($z = 0$ mm).

measurement when the pump beam is turned on, thus isolating the thermally-induced aberrations $W_{\mathrm{ab}}(x, y)$ of the end-pumped Nd:YAG crystal only. The wavefront $W_{\mathrm{ab}}(x, y)$ (in units of waves) can then be easily converted to a transmittance function $t_{\mathrm{ab}}(x, y)$

$$t_{\mathrm{ab}}(x, y) = e^{i\,2\pi\,W_{\mathrm{ab}}(x,y)} \tag{4.2}$$

Any LG_p^l mode can then be modulated by the phase aberration $t_{\mathrm{ab}}(x, y)$ to create an aberrated optical field $\Psi(x, y)$

$$\Psi(x, y) = \mathrm{LG}_p^l \times t_{\mathrm{ab}}(x, y) \tag{4.3}$$

The procedure of measuring real wavefront aberrations in optical systems and subsequent numerical phase reconstruction is a useful tool for performing computational simulations to better understand and characterize complex optical processes.

4.2.2 Modal Decomposition

An elegant approach to characterize the effects of wavefront aberrations on the purity of any arbitrary optical field $\Psi(x, y)$ is to perform modal decomposition, which describes modes that constitute $\Psi(x, y)$ using a complete orthogonal basis set, such as the circularly symmetric Laguerre-Gaussian modes of equation 1.9 or the rectangular symmetric Hermite-Gaussian modes of equation 1.10 [251]. When the field $\Psi(x, y)$ lacks circular symmetry, the rectangular symmetric Hermite-Gaussian $\mathrm{HG}_{n,m}$ modes are used as the modal decomposition expansion

basis set. We can expand $\Psi(x, y)$ into constituent $\mathrm{HG}_{n,m}$ modes as follows:

$$\begin{aligned}\Psi(x,y) &= \sum_{m=0}^{\infty}\sum_{n=0}^{\infty} a_{n,m}\mathrm{HG}_{n,m}(x,y) \\ &= \sum_{m=0}^{\infty}\sum_{n=0}^{\infty} |a_{n,m}|e^{i\phi_{n,m}}\mathrm{HG}_{n,m}(x,y)\end{aligned} \tag{4.4}$$

Where $a_{n,m}$ are complex-amplitude terms containing the modal weightings $|a_{n,m}|$ and complex modal phases $\phi_{n,m} = \arg(a_{n,m})$. The complex-amplitude coefficient $a_{n,m}$ can be determined by taking the inner product of the $\mathrm{HG}_{n,m}$ modes with the aberrated field $\Psi(x, y)$:

$$a_{n,m} = \iint_{-\infty}^{\infty} \mathrm{HG}^{*}_{n,m}\Psi(x,y)\mathrm{d}x\mathrm{d}y \tag{4.5}$$

With a sufficiently large set of amplitude coefficients $|a_{n,m}|$ and corresponding phases $\phi_{n,m}$, the aberrated field $\Psi(x, y)$ is reconstructed using equation 4.4. The amplitude weightings should be normalized so that $\sum_{n,m} |a_{n,m}|^2 = 1$.

4.2.3 Gouy Phase in astigmatic systems

In astigmatic systems, the lack of circular symmetry is a strong motivation for using $\mathrm{HG}_{n,m}$ modes instead of LG^{l}_{p} modes. There are mainly two ways of characterising an astigmatic mode: to analyse the coordinates and its parameters separately [252] or to use a modal decomposition of the beam including the aberrated wavefront. The Gouy phase plays an important role in both cases. In the first, the difference in Rayleigh ranges for x/y coordinates creates a phase difference between the constituent Hermite polynomials of the mode. In the latter, the Gouy phase is responsible for an intramodal phase proportional to the mode order accumulated over propagation. This intra-modal phase can be responsible for local constructive/destructive interference, which can describe simple effects such as the focusing caused by a lens [253] and even complex phenomena like self-imaging [254]. Moreover, the latter will be used to explain the vortex-splitting effect observed. Naturally, the astigmatic wavefront and its lack of circular symmetry will introduce an asymmetry in the modal decomposition. On the HG basis, this translates to modes of some indices being preferred over others, where the indices are associated with a specific coordinate. Since the level of detail in the wavefront increases, more modes will be seen in the decomposition and the different mode orders create propagation effects.

4.3 Experimental Setup

The experimental setup, depicted in Figure 4.1, consisted of three main parts; part a) was the spatial light modulator (SLM) beam shaping system used to select LG^{2}_{0} modes, part b) the end-pumped MOPA system, and part c) the aberration measurement using a Shack-Hartmann wavefront sensor.

Part a): A Gaussian beam LG^{0}_{0} at wavelength 1064 nm with a continuous-wave output power of 8 W was collimated and projected onto a water-cooled SLM (Pluto-2) phase-only screen with a D4σ radius of $\omega_0 = 3$ mm. Computer-generated holograms (CGH) of the LG^{2}_{0} modes of varying sizes were displayed on the SLM screen to perform complex-amplitude phase modulation. The reflected LG^{2}_{0} beams were spatially filtered using a $4f$ imaging system with

a variable aperture at 2F from the SLM screen to remove the undesired diffraction orders. An afocal 5× demagnifying lens pair of focal lengths $f_1 = 500$ mm & $f_2 = 100$ mm was used to relay image the LG_0^2 beams to the pumped end of an Nd:YAG crystal rod. The LG_0^2 beam waist sizes encoded on the CGH were made large to maximize the area on the SLM screen and spatial overlap with the Gaussian envelope to extract maximal power, without exceeding the damage threshold of the liquid-on-crystal layer (200 W/cm^2).

Part b): The MOPA system was constructed using an Nd:YAG crystal (0.5% atm. ϕ4 mm x 25mm) mounted in a water-cooled (18 C°) copper block and the pump source was an 808 nm, 200 μm core diameter multi-mode fibre-coupled (FC) diode laser module $P_p = 0 - 60$ W. The exit face of the diode laser fibre tip was single-lens imaged (1:2) to the surface of the crystal through a 45° dichroic mirror D_1, which is high-reflective coated at 1064 nm wavelength and anti-reflective coated at 808 nm wavelength, to a achieve a FWHM radius of $\omega_p = 200$ μm. The pump beam size ω_p was kept constant throughout the experiment. The pump beam intensity insets, shown in Figure 4.1, were measured in free-space after propagating through the dichroic mirror. At the image plane of the pumped crystal face ($z = 0$ mm), we considered LG_0^2 beam sizes with 4σ radii of $\omega_s = 100$ μm, 160 μm and 200 μm, corresponding to $\beta = \omega_s/\omega_p$ values of 0.5, 0.8 and 1, respectively, as illustrated by the concentric rings in the bottom right inset of Figure 4.1. Since the plane of the SLM screen is relay imaged to the crystal face, only the CGH phase profiles were changed to select different LG_0^2 beam sizes to make the setup consistent, repeatable and simple to switch between β values without any realignment required. The output beams were propagated over a distance $d_1 = 430$ mm from the pumped end of the crystal to lens a $L_1 = 250$ mm, with lens $L_2 = 37.5$ mm placed at the beam waist position $d_2 = Z_0$ of lens L_1. The beam was analysed symmetrically through the focus of L_2 using a CCD camera mounted on a motorized translation stage for each β value at pump powers of $P_p = 25$ W, 40 W and 60 W. The translation stage was adjusted slightly for each measurement so that the focus of L_2 was at position O_2, with $O_1 = O_2 - 25$ mm & $O_3 = O_2 + 25$ mm being the forward and backward limits of the motorized stage.

Part c): A CGH displayed was on the SLM screen to select a Gaussian beam with a D4σ beam radius of $\omega_g = 1.33$ mm and the 4F imaging lenses were changed to $f_1 = f_2 = 300$ mm for 1:1 imaging to the crystal face, so that the Gaussian beam was approximately 3× larger than ω_p, to probe a large area of the thermally induced aberration. The pixel area of the SHWS was filled using lenses $L_1 = 150$ mm and $L_2 = 400$ mm to expand the aberrated Gaussian probe by 2.6×. The SHWS was placed at the image plane of L_2 and wavefront aberrations $W_{ab}(x, y)$ were then recorded at pump at powers of $P_p = 25$ W, 40 W and 60 W.

4.4 Results and Discussion

4.4.1 Pump beam distortion

Efficient coupling of the pump light into the crystal rod is crucial for obtaining a high amplification factor while keeping the thermally-induced aberrations to a minimum. In general, for end-pumped systems specifically, the exit face of the fibre tip is focused through a 45° dichroic mirror to the face of the crystal. We assume that the pump beam remains spatially circular and uniform during this process. However, as shown by the top row inset in Figure 4.1, when measured experimentally we find that the pump beam profile is asymmetric and its degree of asymmetry varies across the crystal length. This asymmetry is measured in terms

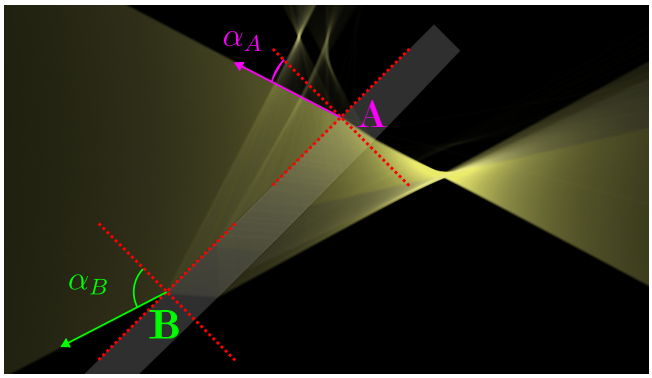


FIGURE 4.2: Ray Optics Simulation depicting the difference in the incident angles (α_A & α_B) between the outer rays (points A & B) of the pump beam (yellow) normal to the dichroic mirror (grey), resulting in a distorted pump beam at the focal plane.

of ellipticity ϵ, which indicates the ratio of the minor (short) axis to the major (long) axis second-moment beam width. When the value of ϵ is equal to 1, the beam profile is perfectly circular. At the image plane of the fibre, located at $z = 0$ mm, the measured ellipticity value was $\epsilon = 0.917$. This value decreased to $\epsilon = 0.796$ at $z = 8.3$ mm and gradually became more circular as the beam propagated further along the crystal and reached $\epsilon = 0.890$ at $z = 25$ mm. Using a ray optic simulator, the converging pump beam passing through a 45° dichroic mirror (fused quarts $n \sim 1.45$) was modelled, shown in Figure 4.2. We see that the outer edges of the light rays marked A and B, have different incident angles $\alpha_A \neq \alpha_B$ normal to the mirror surface and therefore will refract at different rates. When $\alpha_A = \alpha_B$, the outer rays will converge at the same point, but since this is no longer the case the focal point of the rays along the x-axis of the beam shift laterally. The rays along the y-axis remain unaffected since they have equal incident angles $\alpha_A = \alpha_B$ to the surface of the mirror. The density of the light rays is also not uniformly distributed after passing through the dichroic mirror and is skewed toward side A which has the smallest angle normal to the mirror.

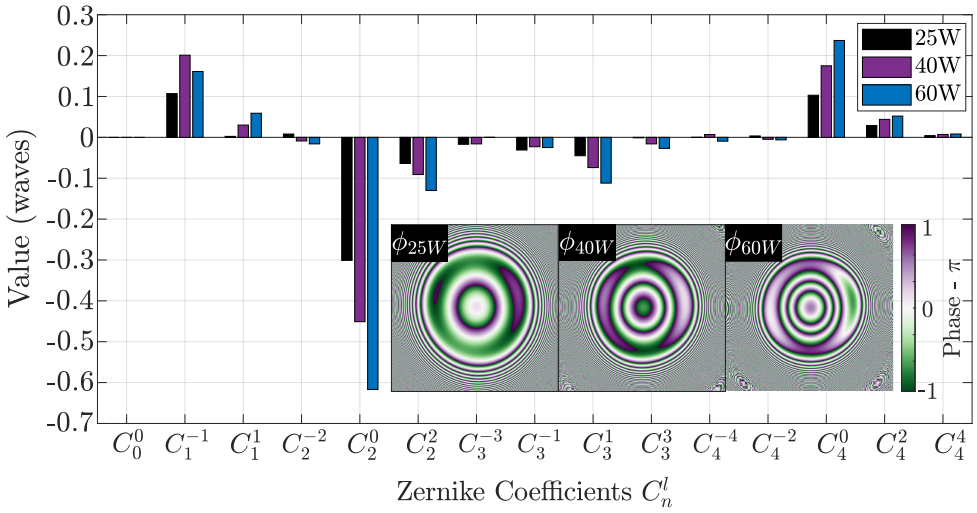


FIGURE 4.3: A bar plot showing the Zernike coefficients C_n^l of the thermally-induced wavefront aberrations for incident pump powers P_p of 25 W (black), 40 W (purple) and 60 W (blue), respectively. The figure inset shows the corresponding reconstructed phase profiles of the wavefront aberration for the pump powers ϕ_{P_p}.

4.4.2 Analysing the thermal aberrations

Due to quantum defect heating effects from energy transfer between the pump photons and crystal, the asymmetric spatial profile after passing through the 45° dichroic mirror manifests in the heat distribution inside the crystal, resulting in non-circular thermally-induced aberrations. A Shack-Hartmann wavefront sensor (SHWS) was used to measure the Zernike coefficients of the induced wavefront aberrations at pump powers of P_p = 25 W, 40 W and 60 W, shown in Figure 4.3.

As expected for a typical end-pumped amplifier, the circularly symmetric negative defocus C_2^0 and positive primary spherical C_4^0 Zernike coefficients were obtained, which scaled proportionately with increasing P_p. Pertinent to this paper is the strong appearance of non-circular primary C_2^2 and secondary C_4^2 vertical astigmatism coefficients, caused by the elliptical heat load created by the distorted pump beam along the horizontal direction and also scaled proportionately with P_p. In comparison, the primary C_2^{-2} and secondary C_4^{-2} oblique astigmatism coefficients were not significant and did not show a clear relationship with P_p. The combination of defocus C_2^0 and vertical astigmatism C_2^2 and C_4^2 aberrations create a cylindrical lens effect, resulting in the $yz-$ and $xz-$ optical axes experiencing different focusing conditions. Interestingly, we see that horizontal coma coefficient C_3^1 scaled proportionality with P_p and was more prevalent than vertical C_3^{-1} coma, which remained constant. The dependence of P_p on the horizontal coma coefficient correlates well with the inhomogeneous distribution of refracted pump rays, shown in Figure 4.2, leading to a non-uniform lens in the horizontal direction. There is, however no inclination in the vertical direction, and thus, no distortion occurs. This figure illustrates how astigmatism can arise from a single effectively transparent element without any measurable curvature. For the measured Zernike coefficients, based on the prevalence, weighting and scaling behaviour with input pump power it is clear that the intensity distribution of the pump distortion through the 45° mirror has translated directly to the thermal aberrations of the crystal in the form of strong vertical C_2^2 and C_4^2, and horizontal coma C_3^1 coefficients.

Using the measured Zernike coefficients, it is easy to numerically recreate the phase profile of the thermal aberration using the wavefront reconstruction process, as explained by equations 4.1, 4.2 and 4.3. The reconstructed phase profiles $\phi_{25\,\mathrm{W}}$, $\phi_{40\,\mathrm{W}}$ and $\phi_{60\,\mathrm{W}}$, excluding tip C_1^{-1} and tilt C_1^1 coefficients, are shown as insets in Figure 4.3.

4.4.3 How does this affect OAM beams ?

The degree of spatial overlap β between seed and pump sizes is an important parameter to consider when constructing end-pumped MOPA systems. Higher values of β overlap better with the gain region and can extract more power but become more susceptible, especially at high pump powers, to distortions due to non-uniform spatial interactions with the thermal aberrations, whereas smaller values of β extract less power but are less susceptible to aberrations. Therefore, to find the optimal overlap for higher-order OAM modes specifically, we considered a range of β = 0.5, 0.8 and 1. The phase interaction between the LG_0^2 beams and the thermally-induced wavefront aberration was performed using low input seed powers of $P_\mathrm{s} \sim 10$ mW. This was done so that no additional power-dumping optical components were required after the MOPA stage which could potentially introduce secondary aberrations. Nevertheless, since the gain of an amplifier only modulates the intensity of the mode, the phase interaction will have the same effect - regardless of the seed power.

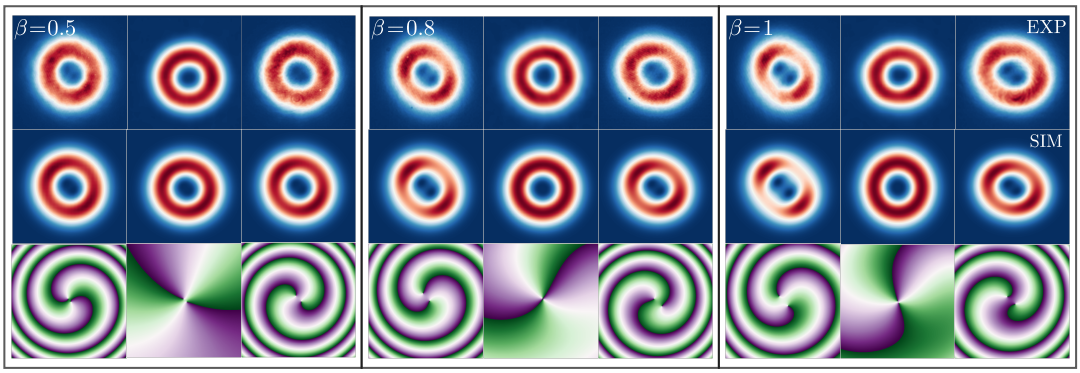


FIGURE 4.4: Experimental results (top row) of the LG_0^2 OAM modes with $\beta = 0.5$ (left grid), 0.8 (middle grid) and 1 (right grid) after interaction with the thermally-induced pump $P_p = 60$ W aberration, measured at positions O_1 (left column), O_2 (middle column) and O_3 (right column) with corresponding simulated results of the beam intensities (middle row) and phases (bottom row).

In the top row of Figure 4.4, we show experimental results of the low-power LG_0^2 beams with different β values after passing through the MOPA system at $P_p = 60$ W, and propagating through the lens system described in Figure 4.1 and recorded at positions O_1, O_2 & O_3. We see that the intensity profiles of the aberrated LG_0^2 beams before (O_1) and after (O_3) the focus positions have two distinct valleys which became more apparent as β increased. The observed effect is the well-known "vortex splitting" phenomenon and is indicative of vortex beams perturbed by astigmatic aberrations, typically caused by tilted or cylindrical lenses. However, to our knowledge, this is the first time the effect has been reported in compact end-pumped amplifiers due to thermal distortions. Interestingly, perturbed symmetry of the modes appeared to recover to a symmetrical state at the focus position O_2 regardless of β.

To analyse this effect more closely, the experiment was simulated using equation 1.9 to generate LG_0^2 modes and modulated by the reconstructed phase aberration $\phi_{60\,W}$ at the plane of the pumped crystal and propagated through the optical system d_1, L_1, d_2 and L_2 and recorded at positions O_1, O_2 and O_3. The simulated intensities, middle row of Figure 4.4, showed excellent agreement with the experimental data across all values of β and also indicate a recovery in the symmetry of the modes at O_2. The phase profiles of the split simulated data, bottom row Figure 4.4, show the physical separation of the phase singularities at locations O_3 & O_1 appear to merge at O_2.

4.4.4 Analyzing the Splitting

To track the phase singularities between positions O_1 and O_3, a local minima search algorithm was used to identify the grid locations (x, y) of the zero-intensity valleys - corresponding to the location of the phase singularities, as shown by the insets of Figure 4.5, for the simulated data. Visually inspecting Figure 4.4, the distance between the phase singularities, defined as d_{sep}, increases with an increase in β. However, when measuring d_{sep} of the top and middle rows we found that d_{sep} was larger at positions O_1 and O_3 for $\beta = 0.5$ than it was for $\beta = 1$. This is because the beam divergence is different for each β; thus, d_{sep} by itself is not very useful and can not be used to directly compare the magnitude of splitting in terms of β.

For a more general description of OAM separation, we define a unit-less variable Γ, which is the ratio of d_{sep} and the beam diameter ω_x that quantifies the "degree of OAM separation"

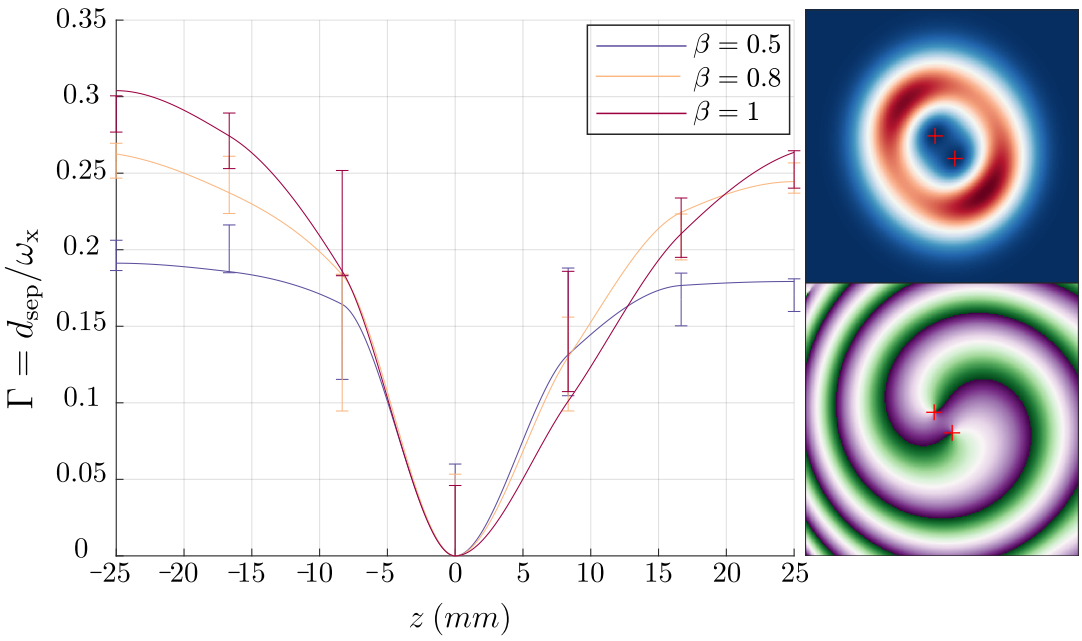


FIGURE 4.5: Graph showing the simulated (solid lines) behaviour of Γ through the focus of lens L_2 for $\beta = 0.5$ (purple), 0.8 (yellow) and 1 (red), with experimentally measured Γ values plotted as error bars. An example (right) of the algorithm used to locate (red crosses) the intensity minima (top) with correlation to the phase singularities (bottom) used to calculate d_{sep}.

as a relative value that accounts for the beam size. Γ visually quantifies the distortion so that when $d_{sep} \longrightarrow 0$ then $\Gamma = 0$ and the beam spatially resembles a symmetric LG_0^2 mode, and when $d_{sep} \neq 0$ the separation of phase singularities become more apparent and $\Gamma > 0$. With this definition of Γ, d_{sep} and ω_x were measured experimentally and in the simulation at evenly spaced points between O_1 to O_3 for the different values of β - plotted in Figure 4.5. The solid lines indicate Γ curves for the simulated data, and the error bars are experimentally measured data points which show good agreement. The trajectory of the initially separated phase singularities at O_1 converge at the focus position O_2 and separate from then on to a slightly lower value of Γ at O_3- which is also visually apparent in Figure 4.4. Additionally, the gamma values at positions O_1 and O_3 for the different values of β corroborate well with the visual degree of OAM separation that we observed in Figure 4.4.

4.4.5 Modal content

The value Γ provides a good quantitative description of the visual degree of spatial distortion but does not provide information regarding the modal purity of the aberrated LG_0^2 beam. To investigate the modal purity, a computational modal decomposition is performed on the modes aberrated by $\phi_{60\,W}$ at the position of L_1 for values of $\beta = 0.5$, 0.6, 0.7, 0.8, 0.9 and 1, following the procedure of equation 4.3 and 4.4. Since the radial symmetry of the LG_0^2 beam has been broken due to the separation of the phase singularities, the modal decomposition was performed in the rectangular symmetric $HG_{n,m}$ basis of equation 1.10. For reference, an unaberrated or 100% pure LG_0^2 beam is described in the $HG_{n,m}$ basis as a superposition of

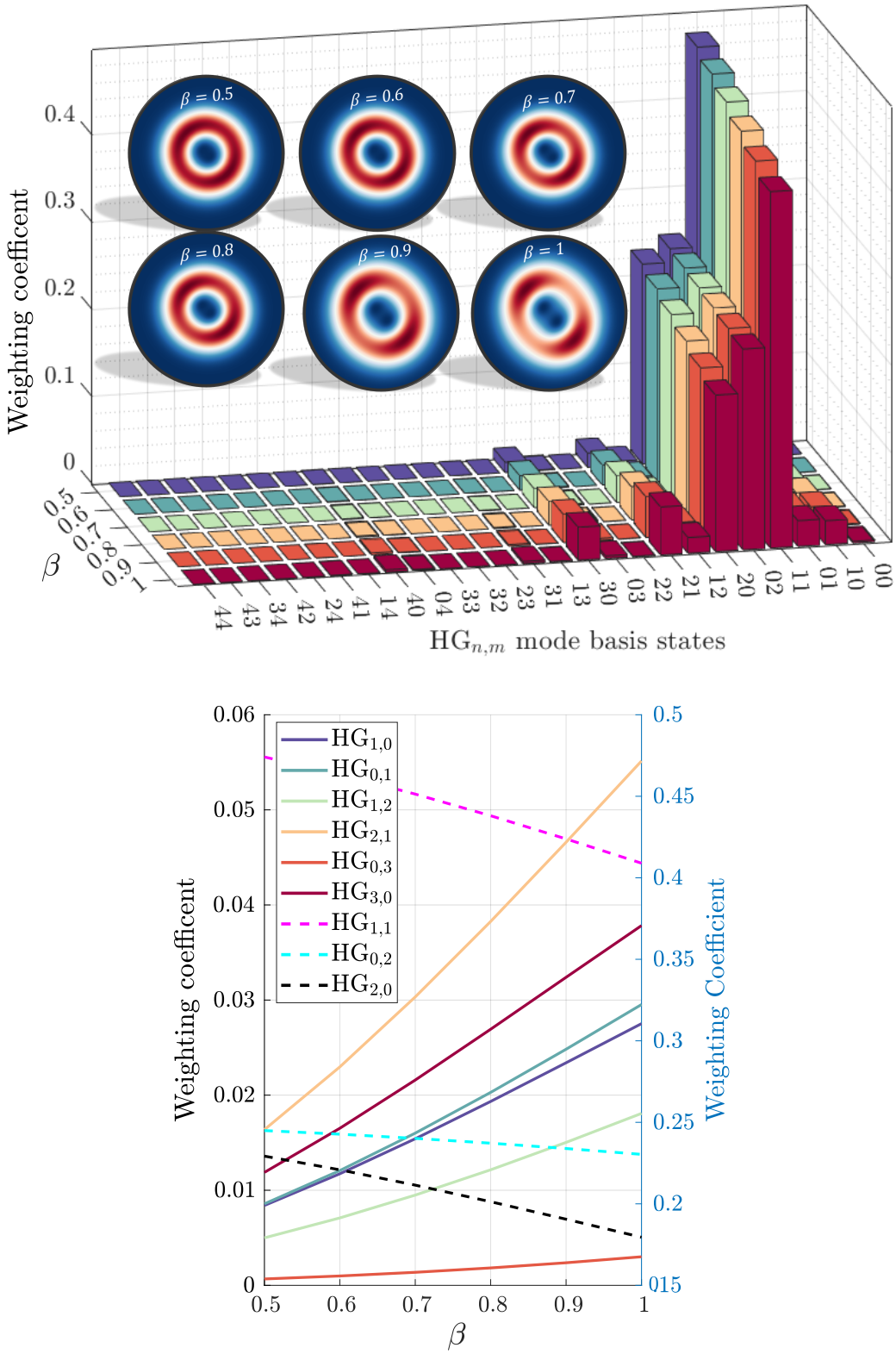


FIGURE 4.6: Computational modal decomposition results (top) in the HG$_{n,m}$ basis of LG$_0^2$ modes for β = 0.5, 0.6, 0.7, 0.8, 0.9, 1 aberrated by phase $\phi_{60\,\mathrm{W}}$, with insets showing the corresponding split OAM spatial profiles. (bottom) Traces of the main constituent HG$_{n,m}$ modes in the bar plot increase (solid lines left axis) and decrease (dashed lines right axis) as a function of β.

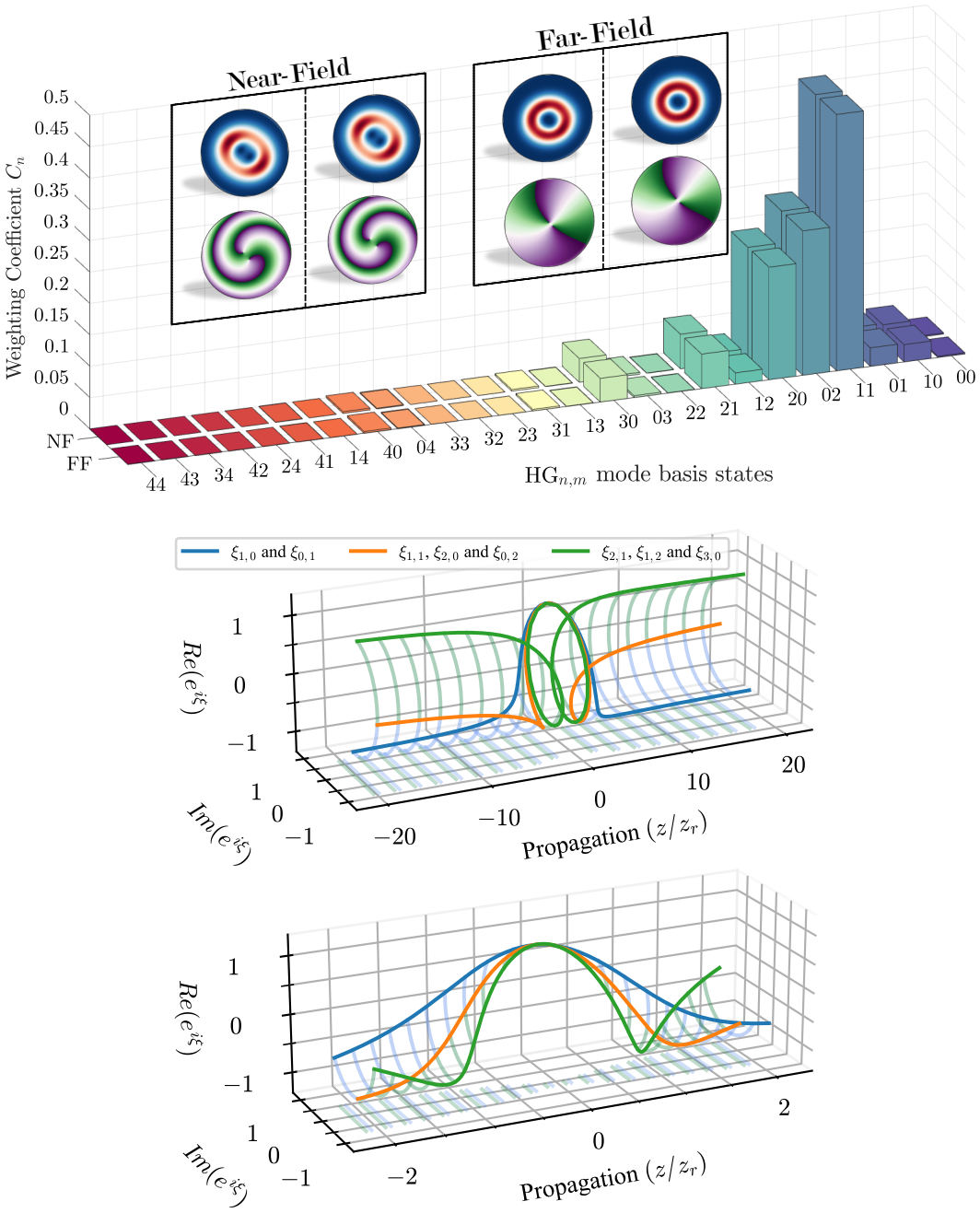


FIGURE 4.7: Differences in Near-Field and Far-Field. In the top figure insets, we see the transverse intensity and phase profiles of the simulated and reconstructed aberrated beam, alongside their modal weightings. The middle and bottom plots show the evolution of the Gouy phase of the three different mode orders that possess relevant weightings. Blue(green) lines connecting blue(green) and orange lines show the difference between the phases, and the light blue(green) lines on the bottom are the length of each corresponding line showing the module of the difference between the phases.

three $HG_{n,m}$ modes:

$$LG_0^{\pm 2} = \sqrt{0.5}HG_{1,1} + \sqrt{0.25}HG_{0,2} + \sqrt{0.25}e^{[\pm i\pi/2]}HG_{2,0}$$

The computational modal decomposition results are depicted by the bar chart of Figure 4.6 (top), showing the modal power weightings of each mode in the $HG_{n,m}$ basis for the different values of β. The insets in Figure 4.6 (top) show the intensity profiles of each β for which modal decomposition was performed and Figure 4.6 (bottom) below shows the evolution of the dominant modal weightings. We see that for $\beta = 0.5$, the purity of the LG_0^2 mode remained high at 94% and decreased gradually as β increased, such that for $\beta = 1$ the modal purity decreased to 82%. It is clear that the purity of the LG_0^2, defined by its three constituent modes $HG_{1,1}$, $HG_{2,0}$ and $HG_{0,2}$, is affected by the selection of β. In the modal traces of Figure 4.6 (bottom), we see that the $HG_{2,0}$ and $HG_{0,2}$ do not decrease at the same rate with β, which is most likely due to the horizontal symmetry of the $HG_{2,0}$ mode coupling more strongly with the aberrations induced by the horizontally distorted pump beam. The combination of defocus C_2^0 and vertical astigmatism C_2^2 and C_4^2 aberrations create a cylindrical lens effect, resulting in the $yz-$ and $xz-$ optical axes experiencing different focusing conditions and can explain the reason for enhanced coupling of the horizontally structured $HG_{n,m}$ modes. Additionally, the appearance of the horizontally structured $HG_{2,1}$ and $HG_{3,0}$ modes are significantly larger than the vertically structured $HG_{1,2}$ and $HG_{0,3}$ modes. Based on the $\{n, m\}$ indices and power weightings of the new modes appearing as β increases, it suggests that the aberrated LG_0^2 mode had an improved spatial overlap with the LG_0^3 and LG_0^1 modes in the modal decomposition calculation.

In Figure 4.5 and 4.6, we have been able to quantify the spatial distortion and modal purity of the aberrated LG_0^2 beams as a function of β for a high pump power of $P_\mathrm{p} = 60$ W. Based on the modal weightings of Figure 4.6, we know that the LG_0^2 beam is no longer a pure mode after the amplifier. However, we have yet to interpret the apparent phase singularity recombination at position O_2, $\Gamma \longrightarrow 0$, which spatially resembles a pure LG_0^2 mode. We then performed a computational modal decomposition in the $HG_{n,m}$ basis on the $\beta = 1$, $\phi_{60\,\mathrm{W}}$ aberrated LG_0^2 beam at positions O_1 and O_2 where the beams have Γ values of 0.3 and 0, respectively.

Figure 4.7 (top) shows the results of the decomposition, where the insets depict the intensity and phase of the initially simulated beams (left inset) with the corresponding reconstructed intensity and phase (right inset) for both the near-field (O_1) and far-field (O_2) positions. The modal decomposition was performed in both planes with the constituent modes having their propagation also simulated, accounting for the difference in the size of modes between the two planes. The results are consistent with the fact that modal weightings should not change in free space propagation. Therefore, for them to have the same modal weightings and composition, but different spatial profiles, their relative phases must also be different.

It is important to notice that the constituent modes for a pure LG_0^2 all belong to the same mode order $n + m = 2$. When astigmatism is introduced in this system, modes of different orders $HG_{2,1}$ and $HG_{3,0}$ (order $n+m = 3$)) become more relevant, as seen on Figure 4.7. For this reason, we recall the importance of the Gouy phase in modal content with order diversity, highlighted in recent works [252, 254, 255].

For this argument, the initial phases between modes of the same order are not relevant, only the phase accumulated in propagation between near and far fields. Effectively, the Gouy phase $\xi(z)$ makes it so that each order of modes gains a phase in propagation proportional to its order and the function arctan of the propagation distance. In the limit of $z \to \pm\infty$, it reaches the asymptotic values of π, $3\pi/2$ and 2π for orders 1, 2 and 3, respectively. This

means that, over propagation from near to far field, modes of order 1 and 3 will gain a phase of $\pm\pi/2$ relative to modes of order 2. Those accumulated intramodal phases create a dynamic behaviour where the field, composed of paraxial modes which are invariant to propagation, can change in propagation. The Gouy phases are illustrated in Figure 4.7, middle and bottom rows, only for orders 1, 2 and 3 for simplicity. When $z \to 0$ the phase differences, depicted as blue (green) arches and projections on the bottom, drop sharply to zero. On regions far from the origin, the relative phase differences reach the asymptotic value of $\pm\pi/2$. The consequence of this relative phase difference is the observation of an intensity pattern that changes on propagation and, in this case, the observation of vortex splitting happening in the near field but not in the far field.

4.4.6 Amplification Results

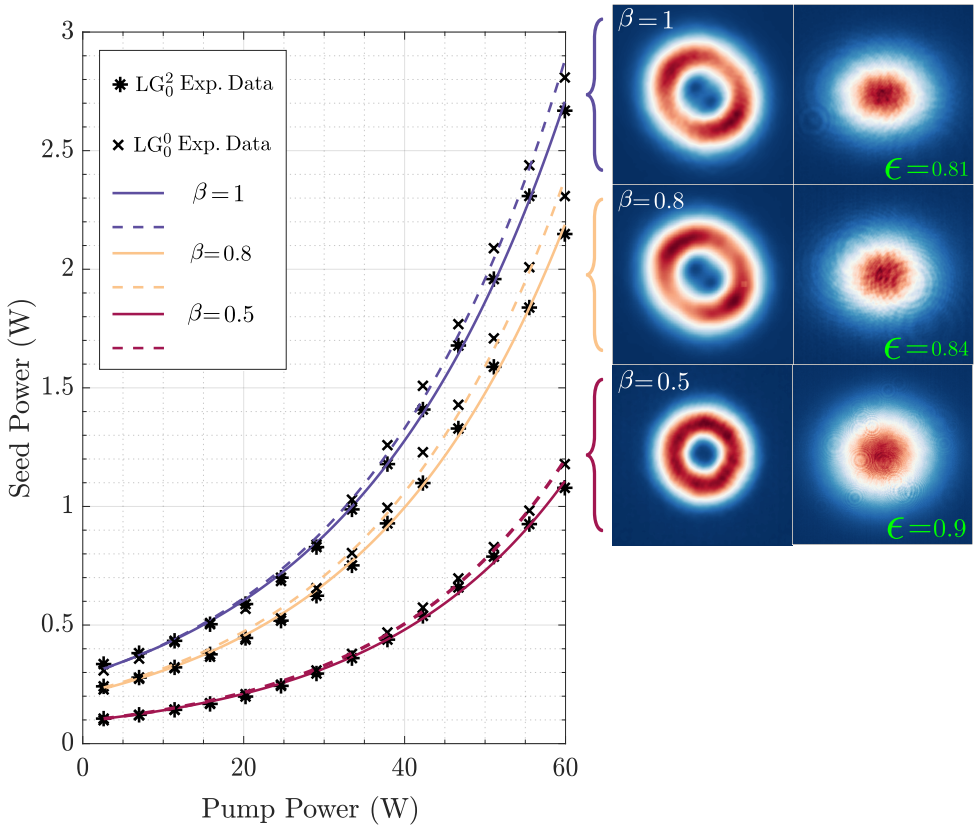


FIGURE 4.8: The output powers of the LG_0^2 higher-order OAM modes (marked with black asterisks) and a comparison with the fundamental Gaussian LG_0^0 mode (marked with black crosses) were measured experimentally for β values of 0.5 (red), 0.8 (yellow), and 1 (purple). An exponential fit was applied to the experimental data points for both the LG_0^2 (represented by solid lines) and the LG_0^0 modes (represented by dashed lines). The right figure insets display the transverse beam intensity profiles at the maximum pump power $P_p = 60$ W for the LG_0^2 (left column) and LG_0^0 (right column) modes for different β values, including the ellipticity values (marked in green) for the LG_0^0 outputs.

.

Due to the sensitivity of the d_{sep} measurement and for consistency between β values, the Gaussian beam size and power on the SLM, and all subsequent optical components were kept fixed throughout the experiment - only the CGHs were swapped. This meant that the reflected power of the SLM varied for each β value due to the reduced spatial overlap with

the Gaussian envelope during complex-amplitude shaping, resulting in maximum LG_0^2 mode powers of P_s = 90 mW, 215 mW and 300 mW, for β = 0.5, 0.8 and 1, respectively. The variations in maximum power did not deter from the thermally-induced aberration study since the measurements were performed at fixed low-powers ∼10 mW. However, rather than reduce the power of all the beams to P_s = 90 mW, we performed amplification using the maximum output for each value of β. We have already shown that by exploiting the Gouy phase shift, the symmetry of the aberrated higher-order OAM beam can be recovered at the far field, therefore, for an application such as material processing where the spatial profile at the focus is more important than the modal purity, a high value of β - corresponding to a higher amplified output power is desirable. If modal purity is required, a low β can be selected and amplified. Nevertheless, the power density of the Gaussian envelope is already at the damage threshold of the SLM device and therefore the current generated seed powers can not be increased further. Therefore, the amplification results for each value of β should be considered as an independent, rather than a comparative amplification study of LG_0^2 modes. The amplification results for β = 0.5, 0.8 and 1, are shown in Figure 4.8 as a function of the input pump power. For β = 0.5, the input seed power grew from 90 mW to 1.1 W, β = 0.8 grew from 215 mW at the input to 2.15 W, and β = 1 grew from 300 mW to 2.6 W, corresponding to gain factors of 12×, 10× and 8.6×, respectively. For comparison of the amplifier performance, the amplified output powers curves of the LG_0^2 modes are compared to that of the fundamental Gaussian mode LG_0^0 for β = 0.5, 0.8 and 1, created on the SLM using complex-amplitude shaping, with matching input powers of 90 mW, 215 mW and 300 mW, respectively. The LG_0^0 modes achieved maximum output powers of 1.17 W, 2.3 W and 2.8 W, corresponding to gain factors of 13×, 10.7× and 9.3× over the LG_0^2 modes for β = 0.5, 0.8 and 1, respectively. The slight advantage in the gain factor of the Gaussian mode is due to its high central peak intensity which has a better overlap with the intensity of the pump beam in the crystal volume, compared to the lower peak intensity LG_0^2 beam profile with a zero intensity central region. An exponential function was fit to all data points, confirming that the amplification is well within the small-signal gain region, where exponential growth is expected. In Figure 4.8, the intensity of the LG_0^2 and LG_0^0 modes are presented on the right of the amplification curve plot, measured at position O_1, for a maximum pump power of P_p = 60 W. We can observe that the OAM splitting is evident during power scaling, and this splitting has the same dependence on the choice of β. The insets displaying the fundamental mode outputs include the beam ellipticity ϵ measurement in green. We can see that β is directly proportional to the ellipticity, which decreases from ϵ = 0.9 for β = 0.5 to ϵ = 0.81 for β = 1. This observation reveals that compact end-pumped MOPAs does not adversely affect the amplified output quality of the fundamental mode, resulting in only minor ellipticity, and thus, the thermally-induced aberrations are usually ignored. However, we demonstrate here that the higher-order OAM modes, subjected to the same thermal aberration, are considerably more susceptible to these aberrations and require a lower value of β than the fundamental modes.

4.5 Conclusion

We have shown that compact end-pumped Nd:YAG crystal rod MOPA designs are inherently susceptible to non-circular aberrations due to a horizontal distortion of the pump beam when focusing through a 45° dichroic mirror. We show that the phase-interaction of higher-order

OAM beams LG_0^2, of varying seed-pump spatial overlap values β, with the produced wavefront aberration results in separation of the phase-singularities and quantified using a new variable Γ. Modal decomposition in the $HG_{n,m}$ revealed that the purity of the LG_0^2 modes decreased as β increased - resulting in an increase in the level of distortion Γ. Interestingly, we show that the Gouy phase shift anomaly for astigmatic beams can be exploited so that $\Gamma \to 0$ in the far-field and spatially recovers to a pure circular OAM mode, for any choice of β. Our results describe the conditions for β in higher-order OAM mode amplification processes to provide a high-spatial and high-modal purity in the far field.

Chapter 5

Conclusion

In conclusion, this dissertation has made contributions to the field of generating high-power structured light using power amplifiers.

In Chapter 1, the reader was introduced to the basic principles of solid-state resonators, higher-order transverse modes, and different methods for selecting such modes using beam shaping techniques. The chapter also included examples of laser-enabled applications that have benefited from the use of structured light, specifically the circularly symmetric Laguerre-Gaussian LG_p^l modes. After reviewing the literature on generating high-power structured light, it was clear that current laser systems have limited flexibility in selecting structured light, particularly higher-order transverse modes at high power. To address this issue, we proposed a laser system that incorporates a dynamic spatial light modulator (SLM) system and end-pumped master oscillator power amplifiers (MOPAs) to achieve on-demand higher-order Laguerre-Gaussian modes at high-power. The realization of such a system has the potential to significantly enhance laser-enabled applications by fully exploiting all the important characteristics of light.

Chapter 2 introduced a new analytical 3D model for an end-pumped Nd:YAG crystal rod MOPA system that was applicable to all cubic crystals. The model used laser beam propagation theory to simulate beam diffraction effects, gain saturation, and thermal effects iteratively along the crystal's length, resulting in a highly accurate three-dimensional model. Furthermore, we proposed a new approach to model multi-mode fiber-coupled diode propagation in free space by using a Gaussian-to-flat-top beam shaping transformation. This was the first time that the multi-mode fiber-coupled pump beam emission had been treated as a complex field in an end-pumped MOPA, demonstrating an accurate representation of the experimentally measured free-space propagation. Additionally, we presented a detailed calibration procedure for accurately calculating the absorption cross-section using spectral data obtained from experiments. Finally, we experimentally verified the accuracy of the newly implemented model improvements, demonstrating significant improvements compared to traditional 2D and 3D models of end-pumped MOPA systems.

In Chapter 3, we reviewed current design approaches for double-pass power scaling using end-pumped rod MOPAs with cylindrical crystal rod geometries and highlighted the design limitations. We proposed a novel dual-pass design configuration using only simple polarization-based optics to allow for effective double-pass amplification while addressing the limitations of the reviewed design approaches. Furthermore, we demonstrated the effectiveness of the novel design by amplifying the first nine LG_p^l modes generated by performing complex amplitude

shaping on an SLM. The entire system including the master oscillator, SLM beam shaping system, and dual-pass MPA had no moving parts, and only the phase screen on the SLM was varied, thus realizing a system fully capable of on-demand high-power structured light with no physical intervention. The dual-pass MOPA achieved amplification factors of up to 17x, and we were able to extract 300% more energy from an equivalent single-pass system. A single imaging lens inside the MOPA allowed for accurate control of the second pass in the amplifier, resulting in the preservation of the modal purity of the higher-order LG_p^l modes, which was confirmed with beam quality measurements. Furthermore, we simulated the single and double-pass output powers of the experiment using an advanced three-dimensional model and demonstrated excellent agreement. The accuracy of the 3D model allowed for a detailed comparative analysis of the amplification characteristic of higher-order LG_p^l modes. We showed that the seed-pump beam intensity overlap integrals of the LG_p^l modes directly correlated to the amplified output. Furthermore, this experiment demonstrated the highest power higher-order pure LG_p^l modes obtained using an SLM and MOPA configuration.

In Chapter 4, we explored the single-pass amplification of vortex beams with higher-order topological charges ($l = 2$) using the compact end-pumped MOPA design subjected to intense pump radiation of >40 kW/cm^2. At the amplifier output, we observed the phenomena of vortex splitting, whereby phase singularities physically separated thus breaking the circular symmetry of the LG_0^2 mode. We probed the thermal aberrations of the Nd:YAG crystal using a Shack-Hartmann wavefront sensor and discovered high levels of vertical astigmatism, horizontal coma, and primary spherical aberrations, attributed to a lateral pump beam distortion induced by the 45° dichroic mirror. The vortex splitting effect was due to vertical astigmatism, which we reported for the first time occurring in amplifiers. We also performed computational modal decomposition to show a direct correlation between the degree of phase separation related not only to the strength of the aberration but also to the relative size of the seed beam and the pump beam. We presented an interesting observation where the phase singularities could recombine to form a spatially pure mode in the far field by careful engineering of the Gouy phase shift.

5.1 Future Work

5.1.1 Amplification of a propagation invariant vector flat-top beam

Building on the work in this dissertation we intend to explore the amplification of other useful beams, such as flat-top beams which are widely utilized in a variety of applications. Flat-top beams have been shown to enhance laser-based applications such as metal additive manufacturing [256, 257], improved control of the ablation zone in thin films [258, 259], faster processing speeds and reduced melt artifacts in micro-machining[260], and enhanced geometrical accuracy in micro drilling [261].

Many of the approaches used to select flat-top beams have a limiting factor in that these beams only exist at a specific plane and their spatial shape changes in propagation which presents a severe limitation on sensitive applications that require high-quality flat-top beams to exist through the focus. An attractive approach to overcome this limitation is through the selection of vector flat-top (VFT) beams [262]. These beams are a superposition, in intensity, of a Laguerre-Gaussian vortex mode (i.e. LG_0^1) and a Gaussian mode (i.e. LG_0^0) having orthogonal polarization states. Due to the polarization orthogonality of the modes, the

superposition VFT state does not suffer from interference artifacts and propagates invariantly over free space. VFT beams have been selected through conical refraction [263], optical feedback [264] and using an SLM [262].

As an initial examination of the amplification of VFT beams, we created the superposition of a Gaussian and vortex beam using a Mach-Zehnder interferometer and performed single-pass amplification using an end-pumped rod MOPA.

Mathematically, one would express such a superposition state as follows:

$$\Psi = \sqrt{\alpha}\,\mathrm{LG}_0^0\ |\mathrm{V}\rangle + \sqrt{(1-\alpha)}\,\mathrm{LG}_0^1\ |\mathrm{H}\rangle\,, \tag{5.1}$$

where $|\mathrm{V}\rangle$ and $|\mathrm{H}\rangle$ represent vertical and horizontal polarisation components, respectively and α represents a modal weighting coefficient so that if $\alpha = 1$ or $\alpha = 0$ a pure Gaussian or vortex mode is recovered, respectively. However, for the special case when $\alpha = 0.5$, as shown in Figure 5.1, the superposition of the equally weighted $|\mathrm{LG}_0^1|^2$ (red) and $|\mathrm{LG}_0^0|^2$ (blue) intensity profiles result in a beam with a uniform plateau, which we call the VFT beam (magenta).

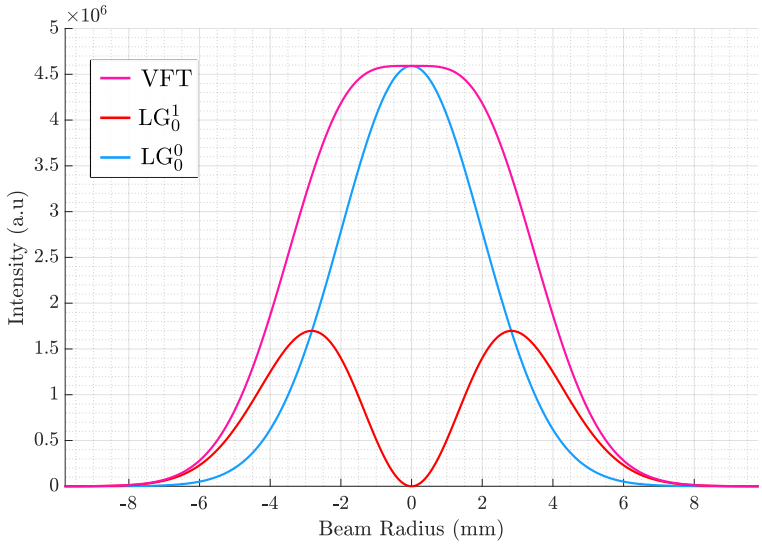


FIGURE 5.1: Intensity plot of the VFT beam (magenta) produced by the superposition of a vortex LG_0^1 mode (red) and a Gaussian LG_0^0 mode (blue), with equal amplitude weighting $\alpha = 0.5$.

The selection of the VFT beam was achieved interferometrically through a Mach-Zehnder configuration, schematically illustrated in Figure 5.2. Here, a collimated vertically polarized Gaussian beam with a D4σ beam diameter of 1 mm at a wavelength of 1.064 μm directed at the interferometer through a rotated zero-order half-wave plate (HWP). The HWP was rotated to obtain a 45° linearly polarized Gaussian beam which then passed through a polarizing beam splitter (PBS) to separate the orthogonal polarization components ($|\mathrm{H}\rangle$ and $|\mathrm{V}\rangle$) into the two arms of the interferometer. The horizontally polarized beam was then passed through a 64-level spiral phase plate (SPP) which imparts an azimuthal phase ($\exp[il\phi]$) with topological charge $l = 1$ onto the Gaussian beam to produce a vortex beam - without altering the polarization state. The vertically polarized arm of the interferometer propagated unaffected equidistant and the two arms recombine at a second polarizing beam splitter to produce the VFT beam at the output. The HWP rotation angle controlled the portion of the Gaussian beam entering the $|\mathrm{H}\rangle$ and $|\mathrm{V}\rangle$ polarization arms of the interferometer and therefore was

used to control the weighting coefficient α in equation 5.1. The experimental system used to perform amplification was the same as that described in chapter 2.

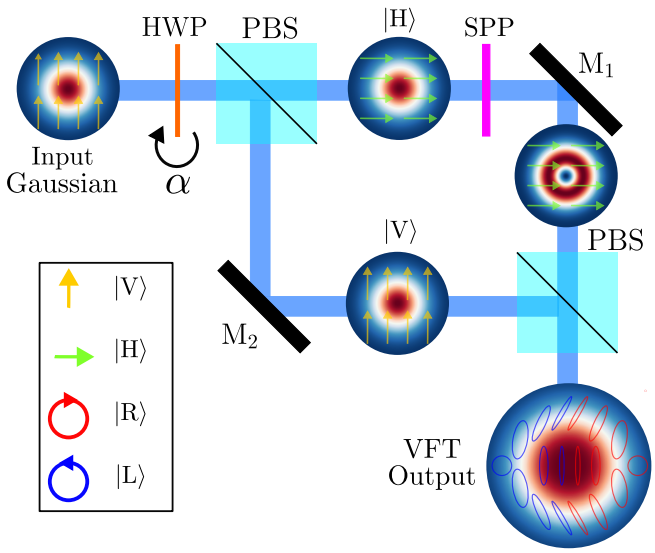


FIGURE 5.2: Mach-Zehnder interferometer comprising of two polarizing beam splitters (PBS) to used to create a VFT beam at the output.

The amplification of the VFT was performed for two input powers of 100 mW and 1 W, corresponding to Gaussian and vortex powers of, 35 mW and 350 mW, and 65 mW and 650 mW, respectively. Amplification was performed at pump beam powers ranging from 6 to 38 W. The experimentally measured amplified output powers (asterisk markers) of the experiment are shown in Figure 5.3 for the VFT beams (orange) and its constituent Gaussian (magenta) and vortex (purple) beam components. For the 100 mW case, Figure 5.3 a), the amplified output of the VFT reached 490 mW, while the Gaussian and vortex beams reached 160 mW and 330 mW, respectively. Similarly, for the 1 W input, Figure 5.3 b), the VFT was amplified to 3.15 W, and the Gaussian and vortex achieved 1.04 W and 2.44 W, respectively. At the output plane of the Nd:YAG crystal, the amplified output intensity of the VFT, Gaussian and vortex beams, under maximum pumping conditions, were relay imaged and measured using a CCD beam profile, shown as insets in Figure 5.3 a) and b). These images show that the amplification process preserved the beam profiles of the Gaussian, vortex and resulting VFT superposition. The power weighting, α, of the Gaussian and vortex beam components were slightly adjusted to obtain a VFT profile at the crystal. This was done to account for losses in the vortex component by removing the radial modes generated by the SPP.

The power curves of the amplifier over a range of pump powers showed good agreement with the theoretical predictions, using the dynamic model described in chapter 2, indicated by the shaded regions. Due to the power fluctuations on the power meter used in the experiment, the simulation was performed with a $\pm 5\%$ upper and lower bound to account for the fluctuations in the power meter head. It is important to note that the model treated the Gaussian and vortex beams separately and combined their net effect to provide the VFT's performance.

The initial investigation done above was not fully optimized but shows very promising initial results. For further investigation of the amplification of the VFT, the experimental system and model will be further optimized to consider arbitrary vector beams. Additionally, an analysis of the vectorness, before and during amplification, using the vector quality factor measurement would determine the preservation of the vector state [265].

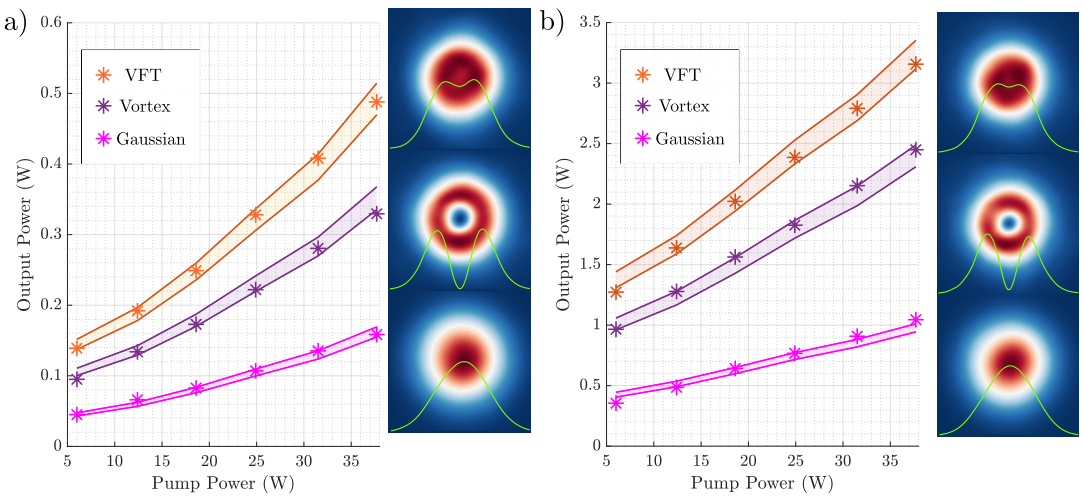


FIGURE 5.3: Amplification outputs of the end-pumped solid-state amplifier system. The solid lines and shaded region represents the simulated power levels where the upper and lower bands account for ±5% fluctuations in power measurements. The experimental data, shown as asterisks, are for the input VFT power of a) 100 mW and b) 1 W, while the figure insets are the intensity profiles, with 1D trace in green, of beams at the maximum amplified power.

5.1.2 Further Power-Scaling with Slab MOPAs

Building upon the work presented in this dissertation, further exploration of multi-pass MOPA architectures is necessary to realize on-demand structured light with power exceeding 100 W. The dual-pass end-pumped MOPA system demonstrated in this study served its purpose well as a pre-amplification stage to transition from the milliwatt to the watt range of power while preserving the complex properties of structured light

Slab and thin-disk MOPA architectures are ideal for high gain amplification and efficient energy extraction. Figure 5.4 a) shows an example of a multi-pass thin-disk MOPA system with two separate stages, which amplified a 20 W Gaussian seed beam to 2 kW at the output [266]. Each MOPA stage allowed for 18 passes through the thin-disk gain medium, corresponding to a total of 36 passes. However, the mirror system used in this design is highly complex and sensitive to misalignment.

On the other hand, the compact slab MOPA system shown in Figure 5.4 b) consists of a rectangular gain medium that is side-pumped by two laser diodes passing through cylindrical lenses to create a "gain sheet" inside the crystal [267]. The seed beam enters the slab and experiences multiple internal reflections within the gain medium. The slab MOPA design is less complex, more compact, and robust, and can be constructed using readily available diode stacks and rectangular crystals. Additionally, the large surface area of the rectangular slab gain media makes it easy to cool both sides evenly, whereas the thin disk can only be cooled on one side. For these reasons, it is worth considering incorporating the slab MOPA architecture into the output of the existing dual-pass MOPA system

The 3D modelling of a slab MOPA design is more complex than that of the circularly symmetric end-pumped cylindrical rod MOPA system. Therefore, a new model must be developed for the slab MOPA, where the pump beam is no longer circularly symmetric or co-axially propagating with the seed beam. In addition, temperature distribution and refractive index change calculations need to be solved in rectangular coordinates, taking into account the

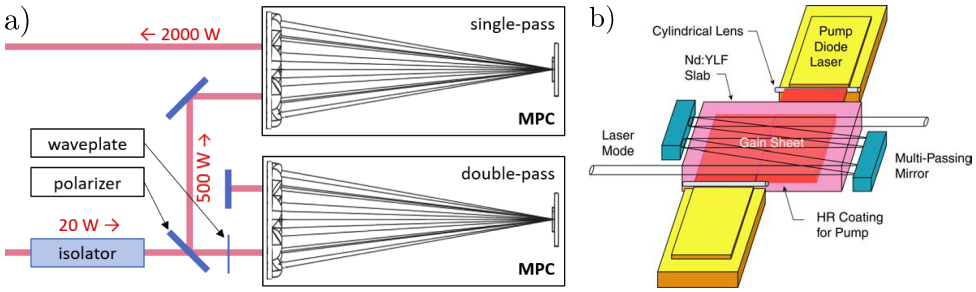


FIGURE 5.4: Figure illustrating multi-pass MOPA systems utilizing a) thin disk [266] and b) slab gain medium [267] geometries to achieve high gain amplification.

asymmetric cooling conditions where only two of the six sides are in contact with the copper heatsink. Therefore, it may be advantageous to explore numerical finite element method (FEM) modelling techniques, which are better suited for complex optical systems

5.1.3 Thermal Beam Shaping

Thermal effects in MOPA systems are inevitable. However, instead of attempting to mitigate these aberrations using heat dissipation strategies, it is possible to exploit thermally-induced phase aberrations to achieve beam shaping. For instance, one of the main phase aberrations that appear in end-pumped Nd:YAG crystals is spherical aberration, which is directly related to the spot size and intensity of the pump beam, as well as the optical properties of the crystal (i.e. dopant concentration and thermal conductivity coefficient). One could control the intensity, beam size, and location (x, y) of the pump beam on the solid state to induce a bespoke phase modulation, similar to a free-form lens. Provided that the input beam does not extract gain from the solid-state crystal, which can be achieved through careful crystal selection, the beam will only be modulated in phase, and the amplitude will remain unaffected.

Optical systems such as the π-shaper [268] use a combination of lenses that induce spherical aberration to achieve a desired beam shape. However, these optical systems are static, whereas a thermally-induced system can be controlled in real-time. For example, by increasing the pump strength, one can dynamically manipulate the strength of spherical aberration and the resulting beam profile. Furthermore, bulk solid-state laser crystals are well-suited for high-power laser beams, and therefore such a system could be applied to kW average power laser systems

5.1.4 Conclusion

In conclusion, this dissertation explored and optimized the traditional end-pumped cylindrical rod-type MOPA system for power scaling pure higher-order Laguerre-Gaussian modes while preserving their complex properties. To further investigate the amplification potential of MOPA systems for high-power structured light, multi-pass architectures such as slab MOPA designs should be considered. In doing so, the development of numerical models using FEM techniques would be highly beneficial for optimizing and characterizing the slab MOPA architecture and studying the interactions of structured light in these systems. Additionally, investigating the thermal effects in end-pumped rod MOPA systems to perform beam shaping is a niche and exciting prospect, offering a dynamic alternative to static optical systems at high power (kW). In closing, this dissertation, along with future work in this

field, is expected to make significant contributions to the advancement of laser systems that incorporate structured light. These developments will help to push the boundaries of laser technology and enable the creation of more sophisticated and versatile systems for a wide range of applications.

Bibliography

1. Griffiths, D. J. & Inglefield, C. *Introduction to Electrodynamics* **6,** 574–574. ISBN: 0-13-919960-8 (Pearson, 2005).
2. Goodman, Joseph W. *Introduction to Fourier Optics* 2nd, 61–62 (Roberts & Compay, 2005).
3. Kogelnik, H. & Li, T. Laser Beams and Resonators. *Applied Optics* **5,** 1550. ISSN: 0003-6935 (1966).
4. Einstein, A. Strahlungs-emission und absorption nach der quantentheorie. *Deutsche Physikalische Gesellschaft* **18,** 318–323. ISSN: 0372-5448 (1916).
5. Maiman, T. H. Stimulated optical radiation in Ruby. *Nature* **187,** 493–494. ISSN: 00280836 (1960).
6. Hodgson, N. & Weber, H. *Laser Resonators and Beam Propagation* Second, 793. ISBN: 0-387-40078-8 (Springer US, 2005).
7. Silfvast, W. T. *Laser Fundamentals* ISBN: 9780521541053. https://www.cambridge.org/core/product/identifier/9780511616426/type/book (Cambridge University Press, 2004).
8. Paschotta, R. *Field Guide to Laser Pulse Generation* ISBN: 9780819472489. http://link.aip.org/link/doi/10.1117/800629 (SPIE, 1000 20th Street, Bellingham, WA 98227-0010 USA, 2008).
9. Bandres, M. A. & Gutiérrez-Vega, J. C. Ince–Gaussian modes of the paraxial wave equation and stable resonators. *J. Opt. Soc. Am. A* **21,** 873–880. https://opg.optica.org/josaa/abstract.cfm?URI=josaa-21-5-873 (2004).
10. Padgett, M. & Bowman, R. Tweezers with a twist. *Nature Photonics* **5,** 343–348. ISSN: 17494885 (2011).
11. Liu, C. Vortex beam and its application in optical tweezers. *Journal of Physics: Conference Series* **1549.** ISSN: 17426596 (2020).
12. Tian, Y., Wang, L., Duan, G. & Yu, L. Multi-trap optical tweezers based on composite vortex beams. *Optics Communications* **485.** ISSN: 00304018 (2021).
13. Woerdemann, M., Alpmann, C., Esseling, M. & Denz, C. Advanced optical trapping by complex beam shaping. *Laser and Photonics Reviews* **7,** 839–854. ISSN: 18638880 (2013).
14. Yang, Y., Ren, Y. X., Chen, M., Arita, Y. & Rosales-Guzmán, C. Optical trapping with structured light: A review. *Advanced Photonics* **3.** ISSN: 25775421 (2021).
15. Otte, E. & Denz, C. Optical trapping gets structure: Structured light for advanced optical manipulation. *Applied Physics Reviews* **7.** ISSN: 19319401 (2020).
16. Ndagano, B., Nape, I., Cox, M. A., Rosales-Guzman, C. & Forbes, A. Creation and Detection of Vector Vortex Modes for Classical and Quantum Communication. *Journal of Lightwave Technology* **36,** 292–301. ISSN: 07338724 (2018).

17. He, C., Shen, Y. & Forbes, A. Towards higher-dimensional structured light. *Light: Science and Applications* **11.** ISSN: 20477538 (2022).
18. Géneaux, R. *et al.* Radial index of Laguerre-Gaussian modes in high-order-harmonic generation. *Physical Review A* **95,** 051801. ISSN: 2469-9926. http://link.aps.org/doi/10.1103/PhysRevA.95.051801 (2017).
19. Hradil, Z *et al.* Radial quantum number of Laguerre-Gauss modes. **063813,** 1–6 (2014).
20. Trichili, A. *et al.* Optical communication beyond orbital angular momentum. *Scientific Reports* **6.** ISSN: 20452322 (2016).
21. Cox, M. A. *et al.* Structured Light in Turbulence. *IEEE Journal of Selected Topics in Quantum Electronics* **27,** 1–21. ISSN: 1077-260X. https://ieeexplore.ieee.org/document/9198098/ (2021).
22. Qiao, Z. *et al.* Multi-vortex laser enabling spatial and temporal encoding. *PhotoniX* **1.** ISSN: 26621991 (2020).
23. Wang, J. *et al.* Terabit free-space data transmission employing orbital angular momentum multiplexing. *Nature Photonics* **6,** 488–496. ISSN: 17494885 (2012).
24. Chen, Y. *et al.* Underwater transmission of high-dimensional twisted photons over 55 meters. *PhotoniX* **1.** ISSN: 26621991. arXiv: 1902.01392 (2020).
25. Gao, H. *et al.* Super-resolution imaging with a Bessel lens realized by a geometric metasurface. *Optics Express* **25,** 13933. ISSN: 10944087. https://opg.optica.org/abstract.cfm?URI=oe-25-12-13933 (2017).
26. Yan, L., Kristensen, P. & Ramachandran, S. Vortex fibers for STED microscopy. *APL Photonics* **4,** 022903. ISSN: 23780967. http://aip.scitation.org/doi/10.1063/1.5045233 (2019).
27. Tamburini, F., Anzolin, G., Umbriaco, G., Bianchini, A. & Barbieri, C. Overcoming the Rayleigh criterion limit with optical vortices. *Physical Review Letters* **97.** ISSN: 00319007. arXiv: 0606196 [astro-ph] (2006).
28. Hou, T. *et al.* Spatially-distributed orbital angular momentum beam array generation based on greedy algorithms and coherent combining technology. *Optics Express* **26,** 14945. ISSN: 10944087 (2018).
29. Hamazaki, J., Morita, R. & Chujo, K. Optical-vortex laser ablation. **18,** 2144–2151 (2010).
30. Omatsu, T. *et al.* Metal microneedle fabrication using twisted light with spin. *Optics Express* **18,** 17967. ISSN: 1094-4087 (2010).
31. Forbes, A. *Laser Beam Propagation* (ed Forbes, A.) 364. https://books.google.co.za/books?id=YErSBQAAQBAJ&pg=PR10&dq=Spatial+Laser+Beam+Characterisation&hl=en&sa=X&ved=0ahUKEwivqJLx1ZXNAhXEIsAKHVQoD9wQ6AEIJDAA#v=onepage&q=SpatialLaserBeamCharacterisation&f=falsehttps://www.taylorfrancis.com/books/9781466554 (CRC Press, 2014).
32. Rubinsztein-Dunlop, H. *et al.* Roadmap on structured light. *Journal of Optics (United Kingdom)* **19,** 013001. ISSN: 20408986. https://iopscience.iop.org/article/10.1088/2040-8978/19/1/013001 (2017).
33. Amphawan, A., Chaudhary, S. & Neo, T. K. Hermite-gaussian mode division multiplexing for free-space optical interconnects. *Advanced Science Letters* **21,** 3050–3053. ISSN: 19367317 (2015).
34. Ndagano, B., Mphuthi, N., Milione, G. & Forbes, A. Comparing mode-crosstalk and mode-dependent loss of laterally displaced orbital angular momentum and Hermite–Gaussian

modes for free-space optical communication. *Optics Letters* **42,** 4175. ISSN: 0146-9592. https://opg.optica.org/abstract.cfm?URI=ol-42-20-4175 (2017).

35. Singh, M. & Malhotra, J. 2 × 10 Gbit/s-10 GHz Radio over Free Space Optics Transmission System Incorporating Mode Division Multiplexing of Hermite Gaussian Modes. *Journal of Optical Communications,* 1–9. ISSN: 01734911 (2019).
36. Cox, M. A. *et al.* The Resilience of Hermite-and Laguerre-Gaussian Modes in Turbulence. *Journal of Lightwave Technology* **37,** 3911–3917. ISSN: 15582213. arXiv: 1901.07203 (2019).
37. Milione, G., Ndagano, B., Mphuthi, N. & Forbes, A. *Using Hermite-Gaussian modes for free-space optical communication (Conference Presentation)* in *Complex Light and Optical Forces XII* (eds Andrews, D. L., Galvez, E. J. & Glückstad, J.) (SPIE, 2018), 11. ISBN: 9781510615830. https://spiedigitallibrary.org/conference-proceedings-of-spie/10549/2292578/Using-Hermite-Gaussian-modes-for-free-space-optical-communication-Conference/10.1117/12.2292578.full.
38. Kiasaleh, K. Spatial beam tracking for Hermite–Gaussian-based free-space optical communications. *Optical Engineering* **56,** 076106. ISSN: 0091-3286 (2017).
39. Meyrath, T. P., Schreck, F., Hanssen, J. L., Chuu, C. S. & Raizen, M. G. A high frequency optical trap for atoms using Hermite-Gaussian beams. *Optics Express* **13,** 2843. ISSN: 10944087. arXiv: 0503349 [cond-mat] (2005).
40. Porfirev, A. P. & Skidanov, R. V. Optical trapping and manipulation of light-absorbing particles by means of a Hermite–Gaussian laser beam. *Journal of Optical Technology* **82,** 587. ISSN: 1070-9762 (2015).
41. Su, J. *et al.* Simultaneous trapping of two types of particles with focused elegant third-order hermite–gaussian beams. *Micromachines* **12,** 1–9. ISSN: 2072666X (2021).
42. Zhang, S. & Yi, L. Two-dimensional Hermite-Gaussian solitons in strongly nonlocal nonlinear medium with rectangular boundaries. *Optics Communications* **282,** 1654–1658. ISSN: 00304018. http://dx.doi.org/10.1016/j.optcom.2008.12.013 (2009).
43. Wang, P. X., Ho, Y. K., Tang, C. X. & Wang, W. Field structure and electron acceleration in a laser beam of a high-order Hermite-Gaussian mode. *Journal of Applied Physics* **101,** 0–7. ISSN: 00218979 (2007).
44. Zhang, H., Liu, S. & Guo, H. Direct acceleration of electrons by intense crossed Hermite-Gaussian laser beams. *Physics Letters, Section A: General, Atomic and Solid State Physics* **367,** 402–407. ISSN: 03759601 (2007).
45. Zhao, Z., Yang, D. & Lü, B. Electron acceleration by a tightly focused Hermite-Gaussian beam: higher-order corrections. *Journal of the Optical Society of America B* **25,** 434. ISSN: 0740-3224 (2008).
46. Beijersbergen, M., Allen, L., van der Veen, H. & Woerdman, J. Astigmatic laser mode converters and transfer of orbital angular momentum. *Optics Communications* **96,** 123–132 (1993).
47. Hsieh, Y.-H., Lai, Y.-H., Hsieh, M. X., Huang, K.-F. & Chen, Y.-F. *Characterizing the Topological Charges in the Astigmatic Transformation from Hermite-Gaussian Modes to Hermite-Laguerre-Gaussian Modes* in *Laser Congress 2019 (ASSL, LAC, LSC)* (OSA, Washington, D.C., 2019), JM5A.8. ISBN: 978-1-943580-68-2. https://opg.optica.org/abstract.cfm?URI=ASSL-2019-JM5A.8.

48. Collett, E. *Field Guide to Polarization (SPIE Vol. FG05)* 134. ISBN: 0819458686. http://spie.org/Publications/Book/626141\%0Ahttp://www.amazon.com/Field-Guide-Polarization-SPIE-Vol/dp/0819458686 (2005).
49. Milione, G., Sztul, H. I., Nolan, D. A. & Alfano, R. R. Higher-order poincaré sphere, stokes parameters, and the angular momentum of light. *Physical Review Letters* **107,** 1–4. ISSN: 00319007 (2011).
50. Sroor, H., Litvin, I., Naidoo, D. & Forbes, A. Amplification of higher order Poincaré sphere beams through Nd:YLF and Nd:YAG crystals. *Applied Physics B: Lasers and Optics* **125,** 0. ISSN: 09462171. http://dx.doi.org/10.1007/s00340-019-7158-3 (2019).
51. Zhan, Q. Cylindrical vector beams: From mathematical concepts to applications. *Optics InfoBase Conference Papers* **1,** 1–57. ISSN: 21622701 (2009).
52. Romero, L. A. & Dickey, F. M. Lossless laser beam shaping. *Journal of the Optical Society of America A* **13,** 751. ISSN: 1084-7529. https://opg.optica.org/abstract.cfm?URI=josaa-13-4-751 (1996).
53. Shealy, D. L. & Hoffnagle, J. A. Laser beam shaping profiles and propagation. *Applied Optics* **45,** 5118–5131. ISSN: 15394522 (2006).
54. Voelkel, R. & Weible, K. J. Laser beam homogenizing: limitations and constraints. *Optical Fabrication, Testing, and Metrology III* **7102,** 71020J. ISSN: 0277786X (2008).
55. Katz, S., Kaplan, N. & Grossinger, I. Using Diffractive Optical Elements. *Laser Technik Journal* **15,** 29–32 (2018).
56. Laskin, A., Laskin, V. & Ostrun, A. Refractive beam shapers for optical systems of lasers. *Components and Packaging for Laser Systems* **9346,** 93460R. ISSN: 1996756X (2015).
57. Fok, L. M., Liu, Y. H. & Li, W. J. Prototyping of beam shaping diffraction gratings by AFM nanoscale patterning. *IEEE Transactions on Automation Science and Engineering* **7,** 49–57. ISSN: 15455955 (2010).
58. Veldkamp, W. B. Laser beam profile shaping with interlaced binary diffraction gratings. *Applied Optics* **21,** 3209. ISSN: 0003-6935. https://opg.optica.org/abstract.cfm?URI=ao-21-17-3209 (1982).
59. Jiang, T. *et al.* Monolithic bifocal zone-plate lenses for confocal collimation of laser diodes. *Optics Letters* **38,** 3739. ISSN: 0146-9592. https://opg.optica.org/abstract.cfm?URI=ol-38-19-3739 (2013).
60. Massari, M., Ruffato, G., Gintoli, M., Ricci, F. & Romanato, F. Fabrication and characterization of high-quality spiral phase plates for optical applications. *Applied Optics* **54,** 4077. ISSN: 0003-6935 (2015).
61. Ruffato, G., Massari, M. & Romanato, F. Generation of high-order Laguerre–Gaussian modes by means of spiral phase plates. *Optics Letters* **39,** 5094. ISSN: 0146-9592 (2014).
62. Rafayelyan, M. & Brasselet, E. Laguerre–Gaussian modal q-plates. *Optics Letters* **42,** 1966. ISSN: 0146-9592 (2017).
63. Rubano, A., Cardano, F., Piccirillo, B. & Marrucci, L. Q-plate technology: a progress review

Invited

. *J. Opt. Soc. Am. B* **36,** D70–D87. https://opg.optica.org/josab/abstract.cfm?URI=josab-36-5-D70 (2019).

64. Machavariani, G., Lumer, Y., Moshe, I. & Jackel, S. Transforming the (0,1)* LG mode with radial polarization to a nearly Gaussian beam by use of a spiral phase element and spatial filter. *XVI International Symposium on Gas Flow, Chemical Lasers, and High-Power Lasers* **6346,** 63461W. ISSN: 0277786X (2006).
65. Li, A., Singh, S. & Sievenpiper, D. Metasurfaces and their applications. *Nanophotonics* **7,** 989–1011. ISSN: 2192-8614 (2018).
66. Bruchhaus, a., Mazarov, P., Bischoff, L., Gierak, J & Wieck, A. Comparison of technologies for nano device prototyping with a special focus on ion beams: A review. *Applied Physics Reviews* **4,** 11302 (2017).
67. Forbes, A., Dudley, A. & McLaren, M. Creation and detection of optical modes with spatial light modulators. *Advances in Optics and Photonics* **8,** 200–227 (2016).
68. Ren, Y. X., Lu, R. D. & Gong, L. Tailoring light with a digital micromirror device. *Annalen der Physik* **527,** 447–470. ISSN: 15213889 (2015).
69. Piehler, S. *et al.* Deformable mirrors for intra-cavity use in high-power thin-disk lasers. *Optics Express* **25,** 4254. ISSN: 1094-4087 (2017).
70. Konrad, T. & Goyal, S. *Laser Beam Propagation - Generation and Propagation of Customized Light* 41–76 (CRC Press, 2014).
71. Moreno, I. *et al.* Diffraction efficiency of stepped gratings using high phase-modulation spatial light modulators. *Optics and Lasers in Engineering* **126,** 105910. ISSN: 0143-8166. https://www.sciencedirect.com/science/article/pii/S0143816619311571 (2020).
72. Grunwald, R. *et al.* High-Flexibility Control of Structured Light with Combined Adaptive Optical Systems. *Photonics* **9.** ISSN: 2304-6732. https://www.mdpi.com/2304-6732/9/1/42 (2022).
73. Shane, J. C., McKnight, D. J., Hill, A., Taberski, K. & Serati, S. *Designing a new spatial light modulator for holographic photostimulation* in *Optical Trapping and Optical Micromanipulation XVI* (eds Dholakia, K. & Spalding, G. C.) **11083** (SPIE, 2019), 1108306. https://doi.org/10.1117/12.2528558.
74. HOLOEYE Photonics AG. *Thermal Management Systems for HOLOEYE* 2023. https://holoeye.com/slm-thermal-management-systems/.
75. Stilgoe, A. B., Kashchuk, A. V., Preece, D. & Rubinsztein-Dunlop, H. An interpretation and guide to single-pass beam shaping methods using SLMs and DMDs. *Journal of Optics (United Kingdom)* **18,** 1–12. ISSN: 20408986. http://dx.doi.org/10.1088/2040-8978/18/6/065609 (2016).
76. Lazarev, G., Gädeke, F. & Luberek, J. *Ultrahigh-resolution phase-only LCOS spatial light modulator* in *Emerging Liquid Crystal Technologies XII* (ed Chien, L.-C.) **10125** (2017), 101250M. ISBN: 9781510606913. http://proceedings.spiedigitallibrary.org/proceeding.aspx?doi=10.1117/12.2250531.
77. Douglass, M. DMD reliability: a MEMS success story. *Reliability, Testing, and Characterization of MEMS/MOEMS II* **4980,** 1. ISSN: 0277786X (2003).
78. Rubano, A., Cardano, F., Piccirillo, B. & Marrucci, L. Q-plate technology: a progress review [Invited]. *Journal of the Optical Society of America B* **36,** D70. ISSN: 0740-3224. https://opg.optica.org/abstract.cfm?URI=josab-36-5-D70 (2019).
79. Kraus, M. *et al.* Microdrilling in steel using ultrashort pulsed laser beams with radial and azimuthal polarization. *Optics express* **18,** 22305–22313 (2010).

80. Kim, D. J., Kim, J. W. & Clarkson, W. A. Q-switched Nd:YAG optical vortex lasers. *Optics Express* **21,** 29449. ISSN: 10944087 (2013).
81. Kim, T. H., Park, J. S., Kim, J. W., Kim, D. J. & Park, E. J. Direct Generation of a Laguerre-Gaussian-Mode Optical Vortex Beam in a Single-Frequency Nd:YVO4 Unidirectional Ring Laser. *Journal of the Korean Physical Society* **75,** 557–560. ISSN: 19768524. http://link.springer.com/10.3938/jkps.75.557 (2019).
82. Li, J., Yao, Y., Yu, J., Xia, K. & Zhou, C. Efficient Vortex Laser With Annular Pumping Formed by Circle Dammann Grating. *IEEE Photonics Technology Letters* **28,** 473–476. ISSN: 1041-1135. http://ieeexplore.ieee.org/document/7327160/ (2016).
83. Yang, Y., Li, Y., Wang, C. & Yang, C. Research on 946 nm LG 01 mode laser considering thermal effect. *Laser Physics* **32,** 095801. ISSN: 1054-660X. https://iopscience.iop.org/article/10.1088/1555-6611/ac7ec6 (2022).
84. Aadhi, A., Sharma, V. & Samanta, G. K. High-power, continuous-wave, tunable mid-IR, higher-order vortex beam optical parametric oscillator. *Optics Letters* **43,** 2312. ISSN: 0146-9592 (2018).
85. Schepers, F., Bexter, T., Hellwig, T. & Fallnich, C. Selective Hermite–Gaussian mode excitation in a laser cavity by external pump beam shaping. *Applied Physics B: Lasers and Optics* **125,** 75. ISSN: 09462171. http://link.springer.com/10.1007/s00340-019-7186-z (2019).
86. Beijersbergen, M. W., Allen, L., van der Veen, H. E. & Woerdman, J. P. Astigmatic laser mode converters and transfer of orbital angular momentum. *Optical Angular Momentum* **96,** 135–144 (2016).
87. Chen, Y. F., Huang, T. M., Kao, C. F., Wang, C. L. & Wang, S. C. Generation of Hermite-Gaussian modes in fiber-coupled laser-diode end-pumped lasers. *IEEE Journal of Quantum Electronics* **33,** 1025–1030. ISSN: 00189197 (1997).
88. Lukowski, M. L., Meyer, J. T., Hessenius, C., Wright, E. M. & Fallahi, M. High-Power Higher Order Hermite-Gaussian and Laguerre-Gaussian Beams from Vertical External Cavity Surface Emitting Lasers. *IEEE Journal of Selected Topics in Quantum Electronics* **25,** 1–6. ISSN: 21910359. https://ieeexplore.ieee.org/document/8675371/ (2019).
89. Gottesman, N. S. *et al.* Intra-Cavity Astigmatic Mode Converting VECSEL. *IEEE Photonics Journal* **14,** 1–6. ISSN: 19430655 (2022).
90. Tuan, P. H., Hsieh, Y. H., Lai, Y. H., Huang, K. F. & Chen, Y. F. Characterization and generation of high-power multi-axis vortex beams by using off-axis pumped degenerate cavities with external astigmatic mode converter. *Optics Express* **26,** 20481. ISSN: 10944087 (2018).
91. Qiao, Z. *et al.* Generating High-Charge Optical Vortices Directly from Laser Up to 288th Order. *Laser and Photonics Reviews* **12,** 1–5. ISSN: 18638899 (2018).
92. Geberbauer, J. W. T., Kerridge-Johns, W. R. & Damzen, M. J. >30 W vortex LG 01 or HG 10 laser using a mode transforming output coupler. *Optics Express* **29,** 29082. ISSN: 10944087 (2021).
93. Chard, S. P., Shardlow, P. C. & Damzen, M. J. High-power non-astigmatic TEM00 and vortex mode generation in a compact bounce laser design. *Applied Physics B: Lasers and Optics* **97,** 275–280. ISSN: 09462171 (2009).

94. Wang, M. *et al.* Laguerre-Gaussian beam generation via enhanced intracavity spherical aberration. *Optics Express* **29,** 27783. ISSN: 10944087. https://opg.optica.org/abstract.cfm?URI=oe-29-17-27783 (2021).
95. Sheng, Q. *et al.* Intracavity spherical aberration for selective generation of single-transverse-mode Laguerre-Gaussian output with order up to 95. *PhotoniX* **3,** 4. ISSN: 26621991. https://photonix.springeropen.com/articles/10.1186/s43074-022-00050-8 (2022).
96. Yonezawa, K., Kozawa, Y. & Sato, S. Generation of a radially polarized laser beam by use of the birefringence of a c-cut Nd:YVO4 crystal. *Optics Letters* **31,** 2151. ISSN: 0146-9592 (2006).
97. Thirugnanasambandam, M. P., Senatsky, Y. & Ueda, K.-i. Generation of radially and azimuthally polarized beams in Yb:YAG laser with intra-cavity lens and birefringent crystal. *Optics Express* **19,** 1905. ISSN: 10944087 (2011).
98. He, H. S., Chen, Z. & Dong, J. Direct generation of vector vortex beams with switchable radial and azimuthal polarizations in a monolithic Nd:YAG microchip laser. *Applied Physics Express* **10.** ISSN: 18820786 (2017).
99. Chen, D., Wang, X., He, H. & Dong, J. Vector vortices with tunable polarization states directly generated in a microchip laser. *Applied Physics Express* **12,** 052012. ISSN: 18820786. https://iopscience.iop.org/article/10.7567/1882-0786/ab1558 (2019).
100. Chen, D. *et al.* High-order cylindrical vector beams with tunable topological charge up to 14 directly generated from a microchip laser with high beam quality and high efficiency. *APL Photonics* **4,** 106106. ISSN: 23780967. http://aip.scitation.org/doi/10.1063/1.5119789 (2019).
101. Jefferson-Brain, T. L., Barber, M. J., Coupe, A. D., Clarkson, W. A. & Shardlow, P. C. Stabilisation of transverse mode purity in a radially polarised Ho:YAG laser using machine learning. *Applied Physics B: Lasers and Optics* **128,** 110. ISSN: 09462171. https://link.springer.com/10.1007/s00340-022-07816-9 (2022).
102. Ngcobo, S., Litvin, I., Burger, L. & Forbes, A. A digital laser for on-demand laser modes. *Nature Communications* **4,** 1–6. ISSN: 20411723. http://dx.doi.org/10.1038/ncomms3289 (2013).
103. Chen, X., Liu, S., Lin, Z., Chen, Z. & Pu, J. Dual-cavity digital laser for intra-cavity mode shaping and polarization control. *Optics Express* **26,** 18182. ISSN: 10944087. https://opg.optica.org/abstract.cfm?URI=oe-26-14-18182 (2018).
104. Sroor, H. *et al.* High-purity orbital angular momentum states from a visible metasurface laser. *Nature Photonics* **14,** 498–503. ISSN: 17494893. http://www.nature.com/articles/s41566-020-0623-z (2020).
105. Wei, D. *et al.* Generating Controllable Laguerre-Gaussian Laser Modes Through Intracavity Spin-Orbital Angular Momentum Conversion of Light. *Physical Review Applied* **11,** 014038. ISSN: 23317019. https://link.aps.org/doi/10.1103/PhysRevApplied.11.014038 (2019).
106. Zhang, L. *et al.* Multifunctional Metasurfaces: Transmission-Reflection-Integrated Multifunctional Coding Metasurface for Full-Space Controls of Electromagnetic Waves (Adv. Funct. Mater. 33/2018). *Advanced Functional Materials* **28,** 1870232. ISSN: 1616-301X (2018).

107. Miao, Y., Zhang, L. & Dong, J. Broadband Petal-Like Raman Laser. *Annalen der Physik* **534,** 2100476. ISSN: 15213889. https://onlinelibrary.wiley.com/doi/10.1002/andp.202100476 (2022).
108. Chen, D., Miao, Y., Wang, H. & Dong, J. Vortex arrays directly generated from an efficient diode-pumped microchip laser. *JPhys Photonics* **2,** 035002. ISSN: 25157647. https://iopscience.iop.org/article/10.1088/2515-7647/ab8a5b (2020).
109. Seghilani, M. S. *et al.* Vortex Laser based on III-V semiconductor metasurface: Direct generation of coherent Laguerre-Gauss modes carrying controlled orbital angular momentum. *Scientific Reports* **6,** 38156. ISSN: 20452322. https://www.nature.com/articles/srep38156 (2016).
110. Zhang, J. *et al.* An InP-based vortex beam emitter with monolithically integrated laser. *Nature Communications* **9,** 2652. ISSN: 20411723. https://www.nature.com/articles/s41467-018-05170-z (2018).
111. Hayenga, W. E. *et al.* Direct Generation of Tunable Orbital Angular Momentum Beams in Microring Lasers with Broadband Exceptional Points. *ACS Photonics* **6,** 1895–1901. ISSN: 23304022. https://pubs.acs.org/doi/10.1021/acsphotonics.9b00779 (2019).
112. Zhang, Z. *et al.* Tunable topological charge vortex microlaser. *Science* **368,** 760–763. ISSN: 0036-8075. https://www.science.org/doi/10.1126/science.aba8996 (2020).
113. Caño-García, M., Quintana, X., Otón, J. M. & Geday, M. A. Dynamic multilevel spiral phase plate generator. *Scientific Reports* **8,** 15804. ISSN: 20452322. https://www.nature.com/articles/s41598-018-34041-2 (2018).
114. Fickler, R., Campbell, G., Buchler, B., Lam, P. K. & Zeilinger, A. Quantum entanglement of angular momentum states with quantum numbers up to 10,010. *Proceedings of the National Academy of Sciences of the United States of America* **113,** 13642–13647. ISSN: 10916490 (2016).
115. Pinnell, J., Rodríguez-Fajardo, V. & Forbes, A. Probing the limits of orbital angular momentum generation and detection with spatial light modulators. *Journal of Optics (United Kingdom)* **23,** 015602. ISSN: 20408986. https://iopscience.iop.org/article/10.1088/2040-8986/abcd02 (2021).
116. Li, R. *et al.* Generating large topological charge Laguerre–Gaussian beam based on 4K phase-only spatial light modulator. *Chinese Optics Letters* **20,** 120501. ISSN: 1671-7694. https://www.researching.cn/articles/OJb370f79f30677e61/html (2022).
117. Li, P. *et al.* Generation of perfect vectorial vortex beams. *Optics Letters* **41,** 2205. ISSN: 0146-9592 (2016).
118. Chen, Y., Fang, Z.-X., Ren, Y.-X., Gong, L. & Lu, R.-D. Generation and characterization of a perfect vortex beam with a large topological charge through a digital micromirror device. *Applied Optics* **54,** 8030. ISSN: 0003-6935 (2015).
119. Xiong, G., Tang, A., Lan, B. & Shen, F. Vortex field manipulation based on deformation mirror with continuous surface. *Guangdian Gongcheng/Opto-Electronic Engineering* **49.** ISSN: 1003501X (2022).
120. S. H. Noh, S. H. N., D. J. Kim, D. J. K. & J. W. Kim, J. W. K. High power generation of adaptive laser beams in a Nd:YVO4 MOPA system. *Chinese Optics Letters* **15,** 120801. ISSN: 1671-7694 (2017).

121. Yu, Y., Di, J., Qu, W. & Asundi, A. Measurement of thermal effects of diode-pumped solid-state laser by using digital holography. *Applied Optics* **57,** 5385. ISSN: 1559-128X (2018).
122. Zhang, X., Zhang, X. & Xiang, A. Analysis of thermal effect and beam wavefront properties for LD-pumped Q-switch Nd:YAG laser. *Optics and Laser Technology* **49,** 268–273. ISSN: 00303992. http://dx.doi.org/10.1016/j.optlastec.2013.01.020 (2013).
123. Liu, B. *et al.* 100 MW Peak Power Picosecond Laser Based on Hybrid End-Pumped Nd:YVO4 and Side-Pumped Nd:YAG Amplifiers. *IEEE Journal of Selected Topics in Quantum Electronics* **24.** ISSN: 21910359 (2018).
124. McNaught, S. J. *et al.* 100 kW coherently combined slab MOPAs. *Optics InfoBase Conference Papers,* 1–2. ISSN: 21622701 (2009).
125. Sumida, D. S., Bruesselbach, H. W., Byren, R. W., Mangir, M. S. & Reeder, R. High-power Yb:YAG rod oscillators and amplifiers. *Solid State Lasers VII* **3265,** 100. ISSN: 0277786X (1998).
126. Markovic, V. *et al.* 160 W 800 fs Yb:YAG single crystal fiber amplifier without CPA. *Optics Express* **23,** 25883. ISSN: 1094-4087 (2015).
127. Maleki, A., Kavosh Tehrani, M., Saghafifar, H., Moghtader Dindarlu, M. H. & Ebadian, H. A compact diode-pumped pulsed Nd:YAG slab laser based on a master oscillator power amplifier configuration. *Laser Physics* **26.** ISSN: 15556611 (2016).
128. Giesen, A. & Speiser, J. Fifteen years of work on thin-disk lasers: Results and scaling laws. *IEEE Journal on Selected Topics in Quantum Electronics* **13,** 598–609. ISSN: 1077260X (2007).
129. Li, Y. *et al.* Concentric vortex beam amplification: experiment and simulation. *Optics Express* **24,** 1658–1667 (2016).
130. Sroor, H., Lisa, N., Naidoo, D., Litvin, I. & Forbes, A. Purity of Vector Vortex Beams through a Birefringent Amplifier. *Physical Review Applied* **9,** 44010. ISSN: 23317019. https://doi.org/10.1103/PhysRevApplied.9.044010 (2018).
131. Sroor, H., Litvin, I., Naidoo, D. & Forbes, A. Amplification of higher order Poincare sphere beams through Nd: YLF and Nd: YAG crystals. *Applied Physics B* **125,** 1–9 (2019).
132. Moshe, I., Jackel, S., Meir, A., Lumer, Y. & Leibush, E. 2kW, M^2 $<$ 10 radially polarized beams from aberration-compensated rod-based Nd:YAG lasers. *Optics Letters* **32,** 47. ISSN: 0146-9592 (2007).
133. Moshe, I. *et al.* Use of polycrystalline Nd:YAG rods to achieve pure radially or azimuthally polarized beams from high-average-power lasers. *Optics Letters* **35,** 2511. ISSN: 0146-9592 (2010).
134. Barber, M. J., Shardlow, P. C., Smith, C. R. & Clarkson, W. A. Radially polarized 33 W emission from a double-pass Ho:YAG thin-slab amplifier. *Journal of the Optical Society of America B* **39,** 2395. ISSN: 0740-3224 (2022).
135. Loescher, A., Negel, J.-P., Graf, T. & Abdou Ahmed, M. Radially polarized emission with 635 W of average power and 21 mJ of pulse energy generated by an ultrafast thin-disk multipass amplifier. *Optics Letters* **40,** 5758. ISSN: 0146-9592 (2015).
136. Negel, J. P. *et al.* Thin-disk multipass amplifier for fs pulses delivering 400 W of average and 2.0 GW of peak power for linear polarization as well as 235 W and 1.2 GW for

radial polarization. *Applied Physics B: Lasers and Optics* **123,** 156. ISSN: 09462171. http://link.springer.com/10.1007/s00340-017-6739-2 (2017).

137. Loescher, A., Röcker, C., Graf, T. & Abdou Ahmed, M. Azimuthally polarized picosecond vector beam with 1.7 kW of average output power. *Optics Letters* **46,** 3492. ISSN: 0146-9592. https://opg.optica.org/abstract.cfm?URI=ol-46-14-3492 (2021).
138. Luo, R. *et al.* Experimental study of diode pumped rubidium amplifier for single higher-order Laguerre-Gaussian modes. *Optics Express* **24,** 13351. ISSN: 10944087 (2016).
139. Niziev, V. G. & Nesterov, A. V. Influence of beam polarization on laser cutting efficiency. *Journal of Physics D: Applied Physics* **32,** 1455–1461. ISSN: 00223727 (1999).
140. Kliner, D. A. *et al. Advanced metal processing enabled by fiber lasers with tunable beam properties* in *Fiber Lasers XIX: Technology and Systems* (eds Jáuregui-Misas, C. & Supradeepa, V. R.) **11981** (SPIE, 2022), 18. ISBN: 9781510648333.
141. Koechner, W. in *Solid-State Laser Engineering* 156–209 (Springer New York, New York, NY). http://link.springer.com/10.1007/0-387-29338-8_5.
142. Koshel, R. J. & Walmsley, I. A. esign of Optically Side-P. *Quantum,* 94–102 (1997).
143. Liu, W. *et al.* Uniformity of pump intensity distribution in diode-array side-pumped laser rod. *High-Power Lasers and Applications VII* **9266,** 92661J. ISSN: 1996756X (2014).
144. Honea, E. C. *et al.* 115-W Tm: YAG diode-pumped solid-state laser. *IEEE Journal of Quantum Electronics* **33,** 1592–1600. ISSN: 00189197 (1997).
145. Glaser, D., Polese, C., Venter, A., Marais, D. & Plaisier, J. Evaluation of laser shock peening process parameters incorporating Almen strip deflections. *Surface and Coatings Technology* **434,** 128158. ISSN: 02578972. https://linkinghub.elsevier.com/retrieve/pii/S0257897222000792 (2022).
146. Nie, S., Zhao, T., Fan, Z. & Xiao, H. Thermal effect of large-diameter laser rod in multi-direction side-pump high power pulsed Nd:YAG laser amplifier. *High Power Lasers, High Energy Lasers, and Silicon-based Photonic Integration* **10152,** 101520H. ISSN: 1996756X (2016).
147. Sovizi, M & Massudi, R. Study of thermal effects, considering birefringence, on phase distortion of beam in a side pumped Nd:YAG rod using BEM. *Optics Communications* **275,** 206–212. ISSN: 00304018 (2007).
148. Lausten, R. & Balling, P. Thermal lensing in pulsed laser amplifiers: an analytical model. *Journal of the Optical Society of America B* **20,** 1479. ISSN: 0740-3224 (2003).
149. Nie, M. *et al.* Design of High-Gain Single-Stage and Single-Pass Nd:YVO4 Amplifier Pumped by Fiber-Coupled Laser Diodes: Simulation and Experiment. *IEEE Journal of Quantum Electronics* **52.** ISSN: 00189197 (2016).
150. Richardson, D. J., Nilsson, J. & Clarkson, W. A. High power fiber lasers: current status and future perspectives [Invited]. *Journal of the Optical Society of America B* **27,** B63. ISSN: 0740-3224 (2010).
151. Rutherford, T. S., Tulloch, W. M., Gustafson, E. K. & Byer, R. L. Edge-pumped quasi-three-level slab lasers: Design and power scaling. *IEEE Journal of Quantum Electronics* **36,** 205–219. ISSN: 00189197 (2000).
152. Perry, B. N., Rabinowitz, P. & Newstein, M. Wave propagation in media with focused gain. *Physical Review A* **27,** 1989–2002. ISSN: 0556-2791. https://link.aps.org/doi/10.1103/PhysRevA.27.1989 (1983).

153. Risk, W. P. Modeling of longitudinally pumped solid-state lasers exhibiting reabsorption losses. *Journal of the Optical Society of America B* **5,** 1412. ISSN: 0740-3224. https://opg.optica.org/abstract.cfm?URI=josab-5-7-1412 (1988).
154. Innocenzi, M. E., Yura, H. T., Fincher, C. L. & Fields, R. A. Thermal modeling of continuous-wave end-pumped solid-state lasers. *Applied Physics Letters* **56,** 1831–1833. ISSN: 00036951 (1990).
155. Sato, Y. & Taira, T. Saturation Factors of Pump Absorption in Solid-State Lasers. *IEEE Journal of Quantum Electronics* **40,** 270–280. ISSN: 00189197 (2004).
156. Cini, L & Mackenzie, J. I. Analytical thermal model for end-pumped solid-state lasers. *Applied Physics B: Lasers and Optics* **123.** ISSN: 09462171 (2017).
157. Bričkus, D. & Dement'Ev, A. S. Modeling of thermal lensing in a [1 1 1]-cut Nd:YAG rod with temperature-dependent parameters and different pumping profiles. *Laser Physics* **27.** ISSN: 15556611 (2017).
158. Xiang, Z. *et al.* Beam quality improvement by gain guiding effect in end-pumped Nd:YVO_4 laser amplifiers. *Optics Express* **19,** 21060. ISSN: 1094-4087 (2011).
159. Abdul-Razzak, M. J. Simulation of thermal lensing in an end-pumped Nd:YAG laser rod with Gaussian and super-Gaussian pump beam profile. *Iraqi Journal of Physics (IJP)* **11,** 81–84. ISSN: 2664-5548. http://ijp.uobaghdad.edu.iq/index.php/physics/article/view/385 (2019).
160. Shen, Y., Gong, M., Ji, E., Fu, X. & Sun, L. Spatial dynamic thermal iteration model for 888 nm end-pumped Nd:YVO4 solid-state laser oscillators and amplifiers. *Optics Communications* **383,** 430–440. ISSN: 00304018. http://dx.doi.org/10.1016/j.optcom.2016.09.040 (2017).
161. Sayem El-Daher, M. Finite element analysis of thermal effects in diode end-pumped solid-state lasers. *Advances in Optical Technologies* **2017.** ISSN: 16876407 (2017).
162. Peng, X. Thermal lensing effects for diode-end-pumped Nd:YVO4 and Nd:YAG lasers. *Optical Engineering* **43,** 2454. ISSN: 0091-3286. http://opticalengineering.spiedigitallibrary.org/article.aspx?doi=10.1117/1.1787529 (2004).
163. Roth, U *et al.* Saturation , Gain , and Noise Properties of a Nd : YAG CW Amplifier. *IEEE Journal of Quantum Electronics* **34,** 1987–1991 (1998).
164. Sazegari, V., Milani, M. R. J. & Jafari, A. K. Structural and optical behavior due to thermal effects in end-pumped Yb:YAG disk lasers. *Applied Optics* **49,** 6910–6916. ISSN: 15394522 (2010).
165. Shayeganrad, G. Efficient design considerations for end-pumped solid-state-lasers. *Optics and Laser Technology* **44,** 987–994. ISSN: 00303992. http://dx.doi.org/10.1016/j.optlastec.2011.10.019 (2012).
166. Fan, S. *et al.* More precise determination of thermal lens focal length for end-pumped solid-state lasers. *Optics Communications* **266,** 620–626. ISSN: 00304018 (2006).
167. Liu, X., Zhao, Y., Yang, A. & Xie, W. Super-Gaussian pumping profiles for solid state lasers. *Solid State Lasers XVI: Technology and Devices* **6451,** 645120. ISSN: 0277786X (2007).
168. Sutton, S. B. & Albrecht, G. F. Optical distortion in end-pumped solid-state rod lasers. *Applied Optics* **32,** 5256. ISSN: 0003-6935 (1993).
169. Pearce, S, Ireland, C. L. M. & Dyer, P. E. Simplified analysis of double-pass amplification with pulse overlap and application to Nd:YVO4 laser. *Optics Communications* **255,** 297–303. ISSN: 00304018 (2005).

170. Albrodt, P., Delen, X., Besbes, M., Lesparre, F. & Georges, P. Simulation and experimental investigation of beam distortions in end-pumped laser rod amplifiers. *Journal of the Optical Society of America B* **35,** 3004. ISSN: 0740-3224 (2018).
171. Schmid, M, Weber, R, Graf, T., Roos, M & Weber, H. P. Numerical Simulation and Analytical Description of Thermally Induced Birefringence in Laser Rods. *IEEE Journal of Quantum Electronics* **36,** 620–626. ISSN: 00189197 (2000).
172. Naidoo, D., Litvin, I. A. & Forbes, A. Brightness enhancement in a solid-state laser by mode transformation. *Optica* **5,** 836–843. https://opg.optica.org/optica/abstract.cfm?URI=optica-5-7-836 (2018).
173. Aït-Ameur, K., Passilly, N., De Saint Denis, R & Fromager, M. *Laser beam shaping* 59–67. ISBN: 9780735405752 (2008).
174. Czeranowsky, C. Effiziente Neodym-Grundzustandslaser und deren Frequenzverdopplung. *Fachbereich Physik* **Diploma,** 67 (1999).
175. Yan-Li, M., Pei-Zhen, D., Ying-Hua, Z., Ju-Ping, G. & Fu-Xi, G. High Efficient Laser Operation of the High-Doped Nd:YAG Crystal Grown by Temperature Gradient Technology. *Chinese Physics Letters* **19,** 1293–1295. ISSN: 0256-307X. https://iopscience.iop.org/article/10.1088/0256-307X/19/9/323 (2002).
176. Dement'ev, A. S. Relationships between different expressions of thermo-optic and photoelastic coefficients of YAG crystal. *Laser Physics* **25,** 95004. ISSN: 15556611. http://dx.doi.org/10.1088/1054-660X/25/9/095004 (2015).
177. Moghtader Dindarlu, M. H., Kavosh Tehrani, M, Saghafifar, H & Maleki, A. Analytical model for thermal lensing and spherical aberration in diode side-pumped Nd:YAG laser rod having Gaussian pump profile. *Chinese Physics B* **24.** ISSN: 16741056 (2015).
178. Bričkus, D. & Dement'ev, A. S. On the use of photoelastic effect and plane strain or plane stress approximations for the description of thermal lensing. *Lithuanian Journal of Physics* **56.** ISSN: 16488504. http://lmaleidykla.lt/ojs/index.php/physics/article/view/3272 (2016).
179. Cao, X, Jahazi, M, Immarigeon, J. P. & Wallace, W. A review of laser welding techniques for magnesium alloys. *Journal of Materials Processing Technology* **171,** 188–204. ISSN: 09240136 (2006).
180. Tabata, N., Yagi, S. & Hishii, M. Present and future of lasers for fine cutting of metal plate. *Journal of Materials Processing Technology* **62,** 309–314. ISSN: 09240136 (1996).
181. Antar, M., Chantzis, D., Marimuthu, S. & Hayward, P. High Speed EDM and Laser Drilling of Aerospace Alloys. *Procedia CIRP* **42,** 526–531. ISSN: 22128271. http://dx.doi.org/10.1016/j.procir.2016.02.245 (2016).
182. Lee, H. *et al.* Lasers in additive manufacturing: A review. *International Journal of Precision Engineering and Manufacturing - Green Technology* **4,** 307–322. ISSN: 21980810 (2017).
183. Martínez, S., Lamikiz, A., Tabernero, I. & Ukar, E. Laser Hardening Process with 2D Scanning Optics. *Physics Procedia* **39,** 309–317. ISSN: 18753892 (2012).
184. Coutts, D. W. *et al.* Generation of flat-top focussed beams for percussion drilling of ceramic and metal. *ICALEO 2002 - 21st International Congress on Applications of Laser and Electro-Optics, Congress Proceedings* (2002).
185. Nasrollahi, V. *et al.* Laser drilling with a top-hat beam of micro-scale high aspect ratio holes in silicon nitride. *Journal of Materials Processing Technology* **281.** ISSN: 09240136 (2020).

186. Wehrmann, A. *et al.* Analysis of laser scribes at CIGS thin-film solar cells by localized electrical and optical measurements. *Optics and Laser Technology* **44,** 1753–1757. ISSN: 00303992. http://dx.doi.org/10.1016/j.optlastec.2012.01.009 (2012).
187. Yuan, W. *et al.* Understanding of adopting flat-top laser in laser powder bed fusion processed Inconel 718 alloy: simulation of single-track scanning and experiment. *Journal of Materials Research and Technology* **16,** 1388–1401. ISSN: 22387854. https://doi.org/10.1016/j.jmrt.2021.12.077 (2022).
188. Duocastella, M. & Arnold, C. B. Bessel and annular beams for materials processing. *Laser and Photonics Reviews* **6,** 607–621. ISSN: 18638880 (2012).
189. Tumkur, T. U., Guss, G., Roehling, J. D., Khairallah, S. A. & Matthews, M. J. Metal Additive Manufacturing using complex beam shaping. *Procedia CIRP* **111,** 71–74. ISSN: 22128271. https://doi.org/10.1016/j.procir.2018.08.092https://linkinghub.elsevier.com/retrieve/pii/S2212827122010113 (2022).
190. Belloni, V. V., Bollani, M., Eaton, S. M., Di Trapani, P. & Jedrkiewicz, O. Microhole generation by high-energy pulsed bessel beams in different transparent materials. *Micromachines* **12.** ISSN: 2072666X (2021).
191. Govekar, E., Jeromen, A., Kuznetsov, A., Kotar, M. & Kondo, M. Annular laser beam based direct metal deposition. *Procedia CIRP* **74,** 222–227. ISSN: 22128271. https://doi.org/10.1016/j.procir.2018.08.099 (2018).
192. Kundtz, N. & Smith, D. R. Extreme-angle broadband metamaterial lens. *Nature Materials* **9,** 129–132. ISSN: 14764660. http://dx.doi.org/10.1038/nmat2610 (2010).
193. Granata, M., Buy, C., Ward, R. & Barsuglia, M. Higher-order laguerre-gauss mode generation and interferometry for gravitational wave detectors. *Physical Review Letters* **105.** ISSN: 10797114. arXiv: 1008.0795 (2010).
194. Chelkowski, S., Hild, S. & Freise, A. Prospects of higher-order Laguerre-Gauss modes in future gravitational wave detectors. *Physical Review D - Particles, Fields, Gravitation and Cosmology* **79.** ISSN: 15507998. arXiv: 0901.4931 (2009).
195. Carbone, L., Bogan, C., Fulda, P., Freise, A. & Willke, B. Generation of high-purity higher-order laguerre-gauss beams at high laser power. *Physical Review Letters* **110,** 1–5. ISSN: 00319007 (2013).
196. Hasnaoui, A., Bencheikh, A., Fromager, M., Cagniot, E. & Aït-Ameur, K. Creation of a sharper focus by using a rectified TEMp0 beam. *Optics Communications* **284,** 1331–1334. ISSN: 00304018. https://linkinghub.elsevier.com/retrieve/pii/S0030401810012241 (2011).
197. Hasnaoui, A., Bencheikh, A. & Aït-Ameur, K. Tailored TEMp0 beams for large size 3-D laser prototyping. *Optics and Lasers in Engineering* **49,** 248–251. ISSN: 01438166. https://linkinghub.elsevier.com/retrieve/pii/S0143816610002058 (2011).
198. Forbes, A., de Oliveira, M. & Dennis, M. R. Structured light. *Nature Photonics* **15,** 253–262 (2021).
199. Forbes, A. Structured light from lasers. *Laser & Photonics Reviews* **13,** 1900140 (2019).
200. Buono, W. T. & Forbes, A. Nonlinear optics with structured light. *Opto-Electronic Advances* **5,** 210174–1 (2022).
201. Senatsky, Y. *et al.* Laguerre-Gaussian modes selection in diode-pumped solid-state lasers. *Optical Review* **19,** 201–221. ISSN: 13499432 (2012).
202. Pan, J. *et al.* Index-Tunable Structured-Light Beams from a Laser with an Intracavity Astigmatic Mode Converter. *Physical Review Applied* **14.** ISSN: 23317019 (2020).

203. Wang, S. *et al.* Generation of wavelength- and OAM-tunable vortex beam at low threshold. *Optics Express* **26,** 18164. ISSN: 1094-4087. https://opg.optica.org/abstract.cfm?URI=oe-26-14-18164 (2018).
204. Sharma, V. *et al.* Tunable vector-vortex beam optical parametric oscillator. *Scientific Reports* **9,** 1–7. ISSN: 20452322 (2019).
205. Sharma, V., Chaitanya Kumar, S., Samanta, G. K. & Ebrahim-Zadeh, M. Tunable, high-power, high-order optical vortex beam generation in the mid-infrared. *Optics Express* **30,** 1195. ISSN: 10944087 (2022).
206. Kim, T. H., Park, J. S., Kim, J. W., Kim, D. J. & Park, E. J. Direct Generation of a Laguerre-Gaussian-Mode Optical Vortex Beam in a Single-Frequency Nd:YVO4 Unidirectional Ring Laser. *Journal of the Korean Physical Society* **75,** 557–560. ISSN: 19768524 (2019).
207. Sheng, Q. *et al.* Intracavity spherical aberration for selective generation of single-transverse-mode Laguerre-Gaussian output with order up to 95. *PhotoniX* **3,** 4. ISSN: 26621991. https://photonix.springeropen.com/articles/10.1186/s43074-022-00050-8 (2022).
208. Thirugnanasambandam, M., Senatsky, Y. & Ueda, K. Generation of very-high order Laguerre-Gaussian modes in Yb:YAG ceramic laser. *Laser Physics Letters* **7,** 637–643. ISSN: 16122011. https://iopscience.iop.org/article/10.1002/lapl.201010044 (2010).
209. Srinivasa Rao, A., Miike, T., Miamoto, K. & Omatsu, T. Direct generation of 523 nm orbital Poincaré mode from a diode-pumped Pr 3+ :LiYF 4 laser with an off-axis optical needle pumping geometry. *Optics Express* **29,** 30409. ISSN: 1094-4087. https://opg.optica.org/abstract.cfm?URI=oe-29-19-30409 (2021).
210. Naidoo, D. *et al.* Controlled generation of higher-order Poincaré sphere beams from a laser. *Nature Photonics* **10,** 327–332. ISSN: 17494893. http://dx.doi.org/10.1038/nphoton.2016.37 (2016).
211. Ahmed, M. A. *et al.* Radially polarized 3kW beam from a CO_2 laser with an intracavity resonant grating mirror. *Optics Letters* **32,** 1824. ISSN: 0146-9592 (2007).
212. Endo, M. Azimuthally polarized 1 kW CO_2 laser with a triple-axicon retroreflector optical resonator. *Optics Letters* **33,** 1771. ISSN: 0146-9592 (2008).
213. Dietrich, T. *et al.* Thin-disk oscillator delivering radially polarized beams with up to 980 W of CW output power. *Optics Letters* **43,** 1371. ISSN: 0146-9592 (2018).
214. Abdou Ahmed, M. *et al.* High-power thin-disk lasers emitting beams with axially-symmetric polarizations. *Nanophotonics* **11,** 835–846. ISSN: 21928614 (2022).
215. Lin, D., Baktash, N., Alam, S.-u. & Richardson, D. J. 106 W, picosecond Yb-doped fiber MOPA system with a radially polarized output beam. *Optics Letters* **43,** 4957. ISSN: 0146-9592 (2018).
216. Loescher, A., Röcker, C., Graf, T. & Abdou Ahmed, M. Azimuthally polarized picosecond vector beam with 1.7 kW of average output power. *Optics Letters* **46,** 3492. ISSN: 0146-9592 (2021).
217. Gong, L. *et al.* Generation of cylindrically polarized vector vortex beams with digital micromirror device. *Journal of Applied Physics* **116.** ISSN: 10897550 (2014).
218. Gong, L. *et al.* Generation of nondiffracting Bessel beam using digital micromirror device. *Applied Optics* **52,** 4566–4575. ISSN: 15394522 (2013).

219. Lazarev, G., Chen, P.-J., Strauss, J., Fontaine, N. & Forbes, A. Beyond the display: phase-only liquid crystal on Silicon devices and their applications in photonics. *Optics express* **27,** 16206–16249 (2019).
220. Turtaev, S. *et al.* Comparison of nematic liquid-crystal and DMD based spatial light modulation in complex photonics. *Optics Express* **25,** 29874. ISSN: 1094-4087 (2017).
221. Li, Y., Zhang, Z., Miller, J. K. & Johnson, E. Ho:YAG rod amplifier for vortex beams. *2015 IEEE Photonics Conference, IPC 2015* **3,** 321–322 (2015).
222. Thies, F. *et al.* Nd:YVO 4 high-power master oscillator power amplifier laser system for second-generation gravitational wave detectors. *Optics Letters* **44,** 719. ISSN: 0146-9592. https://opg.optica.org/abstract.cfm?URI=ol-44-3-719 (2019).
223. Yan, X., Liu, Q., Fu, X., Wang, D. & Gong, M. Gain guiding effect in end-pumped Nd:YVO_4 MOPA lasers. *Journal of the Optical Society of America B* **27,** 1286. ISSN: 0740-3224. https://opg.optica.org/abstract.cfm?URI=josab-27-6-1286 (2010).
224. Moshe, I. *et al.* Maintaining radial-polarization and beam-quality in muli-kW rod-based lasers through the use of polycrystalline Nd:YAG rods. *2011 Conference on Lasers and Electro-Optics Europe and 12th European Quantum Electronics Conference, CLEO EUROPE/EQEC 2011* **809,** 81800 (2011).
225. Liu, B. *et al.* Beam quality management by periodic reproduction of wavefront aberrations in end-pumped Nd:YVO_4 laser amplifiers. *Optics Express* **24,** 8988. ISSN: 10944087 (2016).
226. Pan, S. Q. *et al.* Beam quality improvement by thermally induced aberrations in a diode-end-pumped laser amplifier. *Laser Physics* **23.** ISSN: 1054660X (2013).
227. Wang, C. *et al.* 16 MW peak power, 90 ps all-solid-state laser from an aberration self-compensated double-passing end-pumped Nd:YVO_4 rod amplifier. *Applied Optics* **55,** 2399. ISSN: 0003-6935. https://opg.optica.org/abstract.cfm?URI=ao-55-9-2399 (2016).
228. Li, F. *et al.* Direct Amplification of High Energy Pulsed Laser in Fiber-Single Crystal Fiber with High Average Power. *Crystals* **9,** 216. ISSN: 2073-4352. https://www.mdpi.com/2073-4352/9/4/216 (2019).
229. Martial, I., Balembois, F., Didierjean, J. & Georges, P. Nd:YAG single-crystal fiber as high peak power amplifier of pulses below one nanosecond. *Optics Express* **19,** 11667. ISSN: 1094-4087. https://opg.optica.org/abstract.cfm?URI=ASSP-2011-ATuB6https://opg.optica.org/oe/abstract.cfm?uri=oe-19-12-11667 (2011).
230. Huang, Y. J., Zhuang, W. Z., Su, K. W. & Chen, Y. F. Power Scaling in a Diode-End-Pumped Multisegmented Nd:YVO4 Laser With Double-Pass Power Amplification. *IEEE Journal of Selected Topics in Quantum Electronics* **21,** 226–231. ISSN: 15584542. http://ieeexplore.ieee.org/document/6849936/ (2015).
231. Marshall, L. R., Kaz, A. & Burnham, R. L. Highly efficient TEM_00 operation of transversely diode-pumped Nd:YAG lasers. *Optics Letters* **17,** 186. ISSN: 0146-9592. https://opg.optica.org/abstract.cfm?URI=ol-17-3-186 (1992).
232. Zhang, H. *et al.* Grafted optical vortex with controllable orbital angular momentum distribution. *Optics Express* **27,** 22930. ISSN: 10944087 (2019).
233. Toyoda, K. *et al.* Transfer of light helicity to nanostructures. *Physical Review Letters* **110,** 1–5. ISSN: 00319007 (2013).

234. Yan, X., Guo, L., Cheng, M. & Li, J. Controlling abruptly autofocusing vortex beams to mitigate crosstalk and vortex splitting in free-space optical communication. *Optics Express* **26,** 12605. ISSN: 10944087 (2018).
235. Watanabe, T. *et al.* Two-point-separation in super-resolution fluorescence microscope based on up-conversion fluorescence depletion technique. *Optics Express* **11,** 3271. ISSN: 10944087 (2003).
236. Aleksanyan, A., Kravets, N. & Brasselet, E. Multiple-Star System Adaptive Vortex Coronagraphy Using a Liquid Crystal Light Valve. *Physical Review Letters* **118,** 1–5. ISSN: 10797114 (2017).
237. Willner, A. E. *et al.* Optical communications using orbital angular momentum beams. *Advances in Optics and Photonics* **7,** 66. ISSN: 19438206 (2015).
238. Omatsu, T., Miyamoto, K. & Lee, A. J. Wavelength-versatile optical vortex lasers. *Journal of Optics* **19,** 123002 (2017).
239. Forbes, A. Advances in Orbital Angular Momentum Lasers. *Journal of Lightwave Technology* (2022).
240. Forbes, A. Controlling light's helicity at the source: orbital angular momentum states from lasers. *Philosophical Transactions of the Royal Society A* **375,** 20150436 (2017).
241. Rosales-Guzmán, C., Ndagano, B. & Forbes, A. A review of complex vector light fields and their applications. *Journal of Optics (United Kingdom)* **20.** ISSN: 20408986 (2018).
242. Karimi, E., Zito, G., Piccirillo, B., Marrucci, L. & Santamato, E. Hypergeometric-gaussian modes. *Optics letters* **32,** 3053–3055 (2007).
243. Sephton, B., Dudley, A. & Forbes, A. Revealing the radial modes in vortex beams. *Applied Optics* **55,** 7830. ISSN: 0003-6935 (2016).
244. De Oliveira, M. *et al.* Radially and azimuthally pure vortex beams from phase-amplitude metasurfaces. *arXiv preprint arXiv:2205.15890* (2022).
245. Jin, M. *et al.* Spin-Orbit Modal Optical Vortex Beam Shaping from Dielectric Metasurfaces. *Advanced Optical Materials,* 2202149 (2022).
246. Coursault, D. & Brasselet, E. Nanostructured silica spin–orbit optics for modal vortex beam shaping. *Nanophotonics* **11,** 805–812 (2022).
247. Pinnell, J., Rodríguez-Fajardo, V. & Forbes, A. Probing the limits of orbital angular momentum generation and detection with spatial light modulators. *Journal of Optics* **23,** 015602 (2020).
248. Scholes, S., Kara, R., Pinnell, J., Rodríguez-Fajardo, V. & Forbes, A. Structured light with digital micromirror devices: a guide to best practice. *Optical Engineering* **59,** 041202 (2019).
249. Koyama, M., Hirose, T., Okida, M., Miyamoto, K. & Omatsu, T. Nanosecond vortex laser pulses with millijoule pulse energies from a Yb-doped double-clad fiber power amplifier. *Optics Express* **19,** 14420. ISSN: 1094-4087 (2011).
250. Kang, Q. *et al.* Amplification of 12 OAM Modes in an air-core erbium doped fiber. *Optics Express* **23,** 28341. ISSN: 10944087 (2015).
251. Schulze, C. *et al.* Wavefront reconstruction by modal decomposition. *Optics Express* **20,** 19714. ISSN: 1094-4087 (2012).
252. Buono, W. T., Peters, C., Tau, J., Nape, I. & Forbes, A. Eigenmodes of aberrated systems: the tilted lens. *Journal of Optics* **24,** 125602 (2022).
253. Sroor, H., Moodley, C., Rodríguez-Fajardo, V., Zhan, Q. & Forbes, A. Modal description of paraxial structured light propagation: tutorial. *JOSA A* **38,** 1443–1449 (2021).

254. Da Silva, B. P., Pinillos, V., Tasca, D., Oxman, L. & Khoury, A. Pattern Revivals from Fractional Gouy Phases in Structured Light. *Physical Review Letters* **124,** 033902 (2020).
255. Zhong, R.-Y. *et al.* Gouy-phase-mediated propagation variations and revivals of transverse structure in vectorially structured light. *Physical Review A* **103,** 053520 (2021).
256. Kandis, M & Bergman, T. A simulation-based correlation of the density and thermal conductivity of objects produced by laser sintering of polymer powders. *J. Manuf. Sci. Eng.* **122,** 439–444 (2000).
257. Gurin, V. D., Tyurbeeva, T., Peretyagin, P. Y., Kotoban, D. V. & Okunkova, A. A. Study of layers' structure defects of 3D objects obtained by selective laser melting. *Mechanics & Industry* **17,** 718 (2016).
258. Račiukaitis, G. *et al.* Laser Processing by Using Diffractive Optical Laser Beam Shaping Technique. *Journal of laser micro/nanoengineering* **6** (2011).
259. Kim, H.-Y., Yoon, J.-W., Choi, W.-S., Kim, K.-R. & Cho, S.-H. Ablation depth control with 40 nm resolution on ITO thin films using a square, flat top beam shaped femtosecond NIR laser. *Optics and Lasers in Engineering* **84,** 44–50 (2016).
260. Möhl, A. *et al.* Tailored focal beam shaping and its application in laser material processing. *Journal of Laser Applications* **31,** 042019 (2019).
261. Nasrollahi, V. *et al.* Laser drilling with a top-hat beam of micro-scale high aspect ratio holes in silicon nitride. *Journal of Materials Processing Technology* **281,** 116636 (2020).
262. Bhebhe, N., Rosales-Guzman, C. & Forbes, A. Classical and quantum analysis of propagation invariant vector flat-top beams. *Applied Optics* **57,** 5451. ISSN: 1559-128X (2018).
263. Turpin, A., Loiko, Y. V., Kalkandkiev, T. K., Tomizawa, H. & Mompart, J. Super-Gaussian conical refraction beam. *Opt. Lett.* **39,** 4349–4352 (2014).
264. Naidoo, D., Harfouche, A., Fromager, M., Ait-Ameur, K. & Forbes, A. Emission of a propagation invariant flat-top beam from a microchip laser. *Journal of Luminescence* **170,** 750–754 (2016).
265. Selyem, A., Rosales-Guzmán, C., Croke, S., Forbes, A. & Franke-Arnold, S. Basis-independent tomography and nonseparability witnesses of pure complex vectorial light fields by Stokes projections. *Physical Review A* **100,** 063842. ISSN: 2469-9926. https://link.aps.org/doi/10.1103/PhysRevA.100.063842 (2019).
266. Dietz, T. *et al.* Ultrafast thin-disk multi-pass amplifier system providing 1.9 kW of average output power and pulse energies in the 10 mJ range at 1 ps of pulse duration for glass-cleaving applications. *Optics Express* **28,** 11415. ISSN: 1094-4087. https://opg.optica.org/abstract.cfm?URI=oe-28-8-11415 (2020).
267. Isyanova, Y. *et al. Compact tunable all-solid-state LWIR source for standoff chemical detection* in *Chemical and Biological Standoff Detection* **5268** (2004), 155.
268. Laskin, A. *Achromatic refractive beam shaping optics for broad spectrum laser applications* in *Laser Beam Shaping X* **7430** (2009), 743003.